7-17-2009

Analysis of Channel Networks and the Potential for Sediment Transport in the Vicinity of the North Polar Seas of Titan

Richard Cartwright

ANALYSIS OF CHANNEL NETWORKS AND THE POTENTIAL FOR SEDIMENT TRANSPORT IN THE VICINITY OF THE NORTH POLAR SEAS OF TITAN

by

RICHARD CARTWRIGHT

Under the Direction of Jordan Clayton

ABSTRACT

This study analyzes the available radar evidence in order to describe the morphology of channel networks around the north polar seas of Titan. Critical flow depths necessary to entrain water-ice grains, and denudation rates for a north polar channel network are discussed. The results indicate that channel networks on Titan have similar morphologies to channel networks cut by water on Earth. We also find that water-ice sediment should be readily entrained in the headwaters and downstream sections of the analyzed Titanian basin, given sufficient flow depths of liquid hydrocarbons. Also, the importance of slope and the elevated topography of the highlands surrounding the polar lakes are considered, as well as potential formation theories for the elevated highlands and low-lying maria that dominate the north polar region.

INDEX WORDS: Titan, Liquid hydrocarbons, Dendritic networks, Sediment transport, Synthetic aperture radar, Cassini-Huygens mission, Geomorphology, Fluctuating methane table, Water-ice grains, Polar maria, Uplifted highlands, Atmospheric haze, Convective storms

ANALYSIS OF CHANNEL NETWORKS AND THE POTENTIAL FOR SEDIMENT TRANSPORT IN THE VICINITY OF THE NORTH POLAR SEAS OF TITAN

by

RICHARD CARTWRIGHT

A Thesis Submitted in Partial Fulfillment of the Requirements for the Degree of

Master of Arts

in the College of Arts and Sciences

Georgia State University

2009

ANALYSIS OF CHANNEL NETWORKS AND THE POTENTIAL FOR SEDIMENT TRANSPORT IN THE VICINITY OF THE NORTH POLAR SEAS OF TITAN

by

RICHARD CARTWRIGHT

Committee Chair: Jordan Clayton

Committee: Todd Henry
Larry Kiage

Electronic Version Approved:

Office of Graduate Studies
College of Arts and Sciences
Georgia State University
August 2009

DEDICATION

I would like to thank music for keeping me awake and functioning through the long nights and early mornings spent preparing my thesis. As I recall the different stages of writing this document, music of many genres fills my head and slowly coalesces into a rhythmic soup. While my parents encouraged me to complete this grand project, the gods of music were the ones who kept me company as I stared at my computer screen and read over papers for hours on end. Some of the most important bands that pulsed over my speakers and headphones during the past two years includes: Intronaut, Valet, Enslaved, Mastodon, Black Lips, Animal Collective, Snowman, Women, Crystal Castles, The Knife, The Field, Health, Ruby Suns, and Radiohead. Also of great importance: My undergraduate advisor Linda Taylor who helped sculpt my writing style, my two cats Gobbler and Nibbler, and the magical elixir known as coffee.

ACKNOWLEDGEMENTS

Many people have helped shape this document, but several individuals deserve to be mentioned by name for their input and support. My advisor Jordan Clayton has provided invaluable insight on numerous occasions. His input and support were crucial elements to the successful publication of this Master's thesis. The other members of my committee, Todd Henry and Larry Kiage, have provided feedback and resources that have strengthened this document as well. Furthermore, Randolph Kirk has bolstered the analysis contained within this document by providing the highest resolution images available of Titan's north polar seas. I would also like to thank Shanna Hobson for her tireless patience and support through long nights of research.

TABLE OF CONTENTS

LIST OF TABLES

LIST OF FIGURES

CHAPTER 1.

INTRODUCTION TO TITAN

1.1: Titan's Planetary Characteristics

As the Solar System began to take shape ~4.5 billion years ago, Earth and Titan emerged out of the protoplanetary disc swirling around the young Sun (table 1.1). Titan formed on the edge of Saturn's circumplanetary disc roughly $1.4x10^9$ km away from the Sun, and has a silicate core wrapped in thick layers of water ice (Lebreton et al., 2005). Earth on the other hand, formed close to the Sun where refractory, high density, metals were found in greater relative abundance; consequently, it possesses a dense metallic core surrounded by layers of rocky material. While the materials that comprise Earth and Titan differ greatly, they both possess significant atmospheres with large molecular nitrogen abundances (~78%, ~95%, respectively). Furthermore, the atmospheres of Earth and Titan (table 1.2) both experience a temperature inversion at the top of the troposphere (equatorial altitudes of ~18 km and ~70 km, respectively), which limits the convective lifting of air parcels to the region beneath the tropopause of each world (Lunine and Atreya, 2008).

While clouds above the tropopause are rare on Earth (noctilucent clouds being one example), upper atmospheric haze layers maintain permanent global coverage and are crucial elements of the Titanian hydrocarbon cycle (Atreya, 2007). Solar photons and charged particles from Saturn bombard the upper atmospheric haze, breaking apart the abundant methane molecules. The resulting molecular debris quickly recombines with the surrounding species to create a host of complex hydrocarbons and nitriles (e.g. Yung et al., 1984). The resulting products either recombine further into more complex compounds, or they slowly float down to the surface of Titan (Atreya et al., 2006).

Table 1.1: Comparison of Important Planetary Characteristics of Earth and Titan

Characteristics:	Earth	Titan
Mean Radius (km)	6371	2575
Mass (kg)	59.736×10^{23}	1.345×10^{23}
Density (g/cm^3)	5.52	1.88
Length of year (days)	365	10759
Equatorial Gravity m/s^2	9.78	1.35
Mean Heliocentric Distance (AU)	1.0	9.5
Surface Temperature (K)	288	94
Surface Pressure (bars)	1.013	1.467
Geometric Albedo	0.37	0.21

Source: de Pater and Lissauer (2001).

Table 1.2: Atmospheric Constituents of Titan

Substance	Titan
N_2	95% (near surface)
CH_4	4.9% (near surface)
H_2	0.1 +/- 0.2%
Ar	43ppm
C_2H_6	~20ppm
CO	~45ppm
C_2H_2	3.3ppm
C_3H_8	700ppb
HCN	800ppb (winter) and ~100ppb (summer)
C_2H_4	160ppb
CO_2	15ppb
C_3H_4	10ppb
H_2O	8ppb
HC_3N_3	5ppb (winter) and <1ppb (summer)
CH_3C_2H	5ppb
C_2N_2	5ppb
C_4H_2	1.5ppb
C_6H_6	1.4ppb (winter) and <0.5 (elsewhere)

Many of the listed hydrocarbons are added to the atmosphere via the photochemical destruction of methane. Source**:** Lorenz and Mitton (2008).

The photochemical destruction of methane on Titan has two important consequences over long timescales: (1) without a surface/subsurface reservoir to replenish the methane destroyed by photons and charged particles, atmospheric stocks of methane on Titan will be depleted after ~10 Myr (Lorenz, 2006). (2) The organic material formed from the destruction of methane, assuming constant photochemical loss of CH_4 over the course of Titan's geologic history, should

form a layer perhaps 10-100 m thick over the surface of Titan (Hayes et al., 2008). Thus, a large surface/subsurface source of methane recharges the atmosphere on geologic timescales, or the hydrocarbon cycle on Titan operates on an intermittent basis. Furthermore, the volume of organic particulates that can accumulate on the surface of Titan is dependent on atmospheric recharge of methane from a surface/subsurface source. In other words, if the Titanian hydrocarbon cycle is temporary, then only a thin layer of particulates should coat the surface, and if it is a more permanent facet of Titan's atmospheric processes, then the layer of precipitated organics should be thicker. Further analysis of the hydrocarbon cycle on Titan is required to determine if atmospheric stocks of methane are replenished by surface/subsurface sources.

Titan's hydrocarbon cycle has other tantalizing ramifications. Given the mean surface temperature of ~94 K, the large near-surface abundance of methane (~5%), and seasonal heating of Titan (~26.7° axial tilt), it is likely that methane clouds condense in the troposphere and precipitate liquid hydrocarbons onto the surface of Titan (Atreya et al., 2006). Terrestrial observations of changing brightness levels close to the subsolar point (e.g. Brown et al., 2002) suggested that clouds coalesce in response to enhanced solar heating of the Titanian surface. More importantly, these observed brightness changes dissipated shortly after they emerged, indicating that Titanian clouds precipitate liquids out into the atmosphere. Thus, methane-laden air parcels rise and expand due to seasonal solar heating, reach the corresponding threshold height for condensation (~8-16 km – e.g. Lunine and Atreya, 2008), and precipitate liquid hydrocarbons (principally methane) back towards the surface of Titan.

Differential heating of Earth's atmosphere propels global atmospheric circulation cycles called Hadley cells, which transport air masses from the equator to the poles. Similarly,

differential heating of Titan's surface (from seasonal heating) leads to a single pole-to-pole circulation cell transporting rising warm air from Titan's summer hemisphere to its winter half. The hemispheres experience ~7 Earth year long seasons, with ~15 Earth years in between opposing solstices, leading to ~30 Earth years to complete one entire cycle of 4 seasons. Some researchers suggest that the rising air parcels are laden with hydrocarbons (principally methane and ethane), which precipitate onto the winter hemisphere as the air mass descends (Lorenz and Mitton, 2008). However, other researchers (Griffith et al., 2006) indicate that the winter hemisphere is drier than the summer hemisphere and likely experiences little to no rainfall. While further observations of Titan's atmospheric circulation are necessary, it is clear that the atmosphere of Titan is a dynamic place where permanent layers of haze coexist alongside transient clouds that precipitate liquids towards the surface of Titan.

Mounting radar evidence gathered by the Cassini Orbiter strongly suggests that precipitated hydrocarbon liquids cut channels into the surface of Titan (figure 1.1 – 1.3). The Cassini Orbiter arrived in the Saturnian system in late 2004 (Lorenz and Mitton, 2008). Since its arrival, it has gathered data using a variety of instruments. Chief among its tools is Cassini's radar imaging capabilities, specifically, the SAR mode of the Titan Radar Mapper (e.g. Elachi et al., 2005). Radar images, gathered in long swaths (Figure 1.4) display networks of dark lines at all latitudes, which look strikingly like Terrestrial channels and drainage basins. Thus, analysis of Cassini's radar data suggests that precipitating liquid methane, like water rain on Earth, cuts channels into the surface of Titan.

Supporting the evidence for fluvial processes and features across Titan's surface, are the large radar dark spots (smooth featureless surfaces at the given bandwidth) imaged around the north pole on various flybys. Stofan and her research counterparts (2007) identified these radar

dark spots as polar lakes and seas filled with liquid hydrocarbons. Furthermore, dark networks of lines (i.e. channels) that connect to these radar smooth surfaces, along with the apparent coastlines of the dark spots, strongly support the identification of the features as low-lying basins filled by a liquid substance (probably methane and ethane given the prevailing surface conditions – e.g. Stofan et al., 2007).

Titan is an intriguing analog to Earth; the two worlds share many similar characteristics (moderately dense atmospheres, precipitating clouds, channel networks, etc), but are different enough from one another to raise important questions regarding the geomorphic processes shaping Titan's frigid surface. As such, this study investigates several examples of channel networks around Titan's north pole in order to analyze the morphology of the basins and the potential for sediment transport around the polar seas.

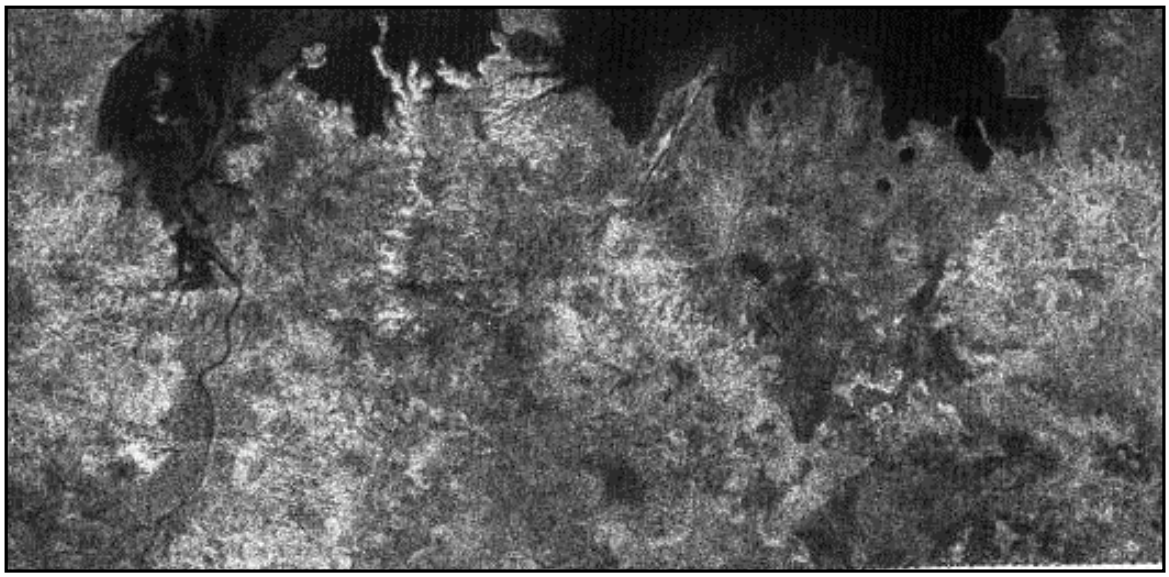

Figure 1.1: Unnamed Polar Lake. Brighter portions of the image represent areas of increased radar. Image is about 300km long by 140km wide. Source: NASA/JPL, PIA01942.

Figure 1.2: Channel Network Draining into Ligeia Mare. Example of Titanian channel network. Outlet of the basin drains into a large polar sea called Ligeia Mare Source: Cassini Radar Team.

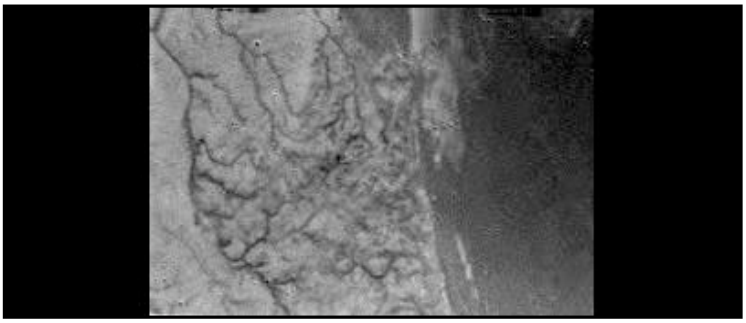

Figure 1.3: Dendritic Network Close to the Huygens Landing Site. One of the first raw images returned by Huygens during its descent. An apparent dendritic network drains the elevated terrain from the middle of the image towards the upper left-hand corner. Image altitude ~16.2km, spatial resolution of ~40m/pixel. Source: ESA, Cassini-Huygens.

1.2: Investigation of Apparent Fluvial Features

Given the evidence for lake-like features filled with liquid hydrocarbons (Stofan et al., 2007), and the globally ubiquitous presence of channel networks (e.g. Lorenz et al., 2008), it is clear that a hydrocarbon cycle occurs on Titan and leads to the formation of erosional features like drainage basins, which transport water-ice grains and organic particles as sediment into low-lying areas. This process is similar to Terrestrial drainage basins cut by water, which carry sediment from areas of higher topography to low-lying outlets or subsurface pathways. The

identification of the radar dark spots and lines as fluvial features; however, does little to explain the geomorphic processes that shaped the features.

Figure 1.4: Radar Swaths. (a) left side of image displays the radar swaths recorded over Titan's northern hemisphere; **(b)** right side of image displays swaths over the southern hemisphere. The equator is the outer circle in both images and the poles are located at the image centers. Source: NASA, Steve Albers from NOAA/GSD.

One potential way to address the geomorphic history of Titanian features is through morphological comparisons between Terrestrial and Titanian channel networks. For example, many channel networks on Titan display remarkably similar morphologies to drainage basins on Earth (e.g. Burr et al., 2006), including many examples of dendritic and contorted basins. Furthermore, if channels are actively cutting into the crust of Titan, then some amount of material is excavated and transported in the flow. In order to investigate the underlying forces that might have shaped the Titanian channels, this study compares two analogous Terrestrial drainage basins with selected channel networks on Titan.

Additionally, Titan presents researchers with an unparalleled opportunity to investigate how fluvial processes might function on another world with starkly different surface conditions compared to Earth. While such a comparison is hindered by Titan's large distance from Earth, making observations difficult, the array of instruments onboard the Cassini orbiter continue to return large volumes of data. Analysis of this gathered radar data, and the topography map produced from overlapping flybys (PIA 10353, see figure 3.1), led to the calculation of the critical depths required to entrainment sediment of a given grain size. Further analysis of the topography data led in PIA 10353 led to the calculation of a denudation rate for the observed basin.

As such, this document investigates the apparent channel networks and polar seas imaged using the SAR mode of Cassini's Titan Radar Mapper. Channel organization, ordering hierarchy, bifurcation ratios, and the potential for sediment transport (specifically the entrainment of water-ice into bed load) are the primary subjects investigated in this study. A comparison between the selected Titan channel networks and Terrestrial drainage basins are made in order to investigate the potential formation mechanisms of the Titanian basins.

1.3 Chapter Organization

This document is organized into five chapters: introduction to Titan and the research questions addressed in this study, background information relevant to the investigation of Titan, the potential for sediment transport, analysis of channel network morphology, and discussion of the results produced by this study and their implications. Chapter 1 has introduced Titan and the evidence supporting liquid methane precipitation cutting channel networks into the moon's crust. The second chapter provides background and technical information for the Cassini-Huygens

Mission, and explores the importance of Cassini's SAR and the intricacies of radar imagery interpretation. Chapter 2 also examines Titan's atmospheric chemistry and possible precipitation regimes on the moon before investigating the potential mechanics of fluvial processes occurring on Titan's surface.

Chapters 3 and 4 analyze north polar SAR imagery, and the available topography data, to investigate the apparent fluvial features recorded around Titan's north pole. Chapter 3 details the calculation of slope for a drainage basin that empties into a branch of the polar sea called Kraken Mare. Subsequent analysis of the basin uses the calculated slope, along with other known quantities, to solve a variety of sediment transport formulas that address the potential for bedload entrainment of water-ice grains from the headwaters to the outlet of the basin. The results are compared to those of Burr et al. (2006) who investigate the sediment transport potential of channelized flow on Titan. Also, a denudation rate is calculated, which describes the minimum amount of time the basin will take to erode down to the base level in response to precipitation events. This denudation rate helps constrain the rate of resurfacing in and around the north polar seas by providing an estimate of the minimum amount of time required to remove the basin.

Chapter 4 explores the morphology of three Titanian basins (including the basin examined in chapter 3) around the north polar seas of Titan. Channel networks are constructed to represent the flow pathways taken by fluids at each of the three basins. After the channel networks are constructed (figure 4.10 - 4.14), stream ordering, using the Strahler technique (1952), is performed at each site. Furthermore, the bifurcation ratios of each grouping of channel segments are calculated, which leads to a basin-wide mean bifurcation ratio that describes the relationship between different channel segments within the same network. The results of the

channel network construction, stream ordering, and bifurcation ratio calculation suggest that liquid methane creates drainage basins with similar morphologies to water-cut Terrestrial basins.

The final chapter of this document focuses on the developing picture of Titan as a dynamic world with complex geomorphic processes continually resurfacing the frigid moon. The discussion considers the work of other authors who describe the surface of Titan, and compares their findings and insight to those developed in this study. The goals of future work utilizing the channels around the north pole are considered. Furthermore, the implications of Titanian fluvial processes are considered as well as the possible role of cryotectonics and topography on the morphology of the selected Titan channel networks.

CHAPTER 2.

BACKGROUND ON THE CASSINI ORBITER AND TITAN'S SURFACE PROCESSES

2.1: The Cassini-Huygens Mission

The Cassini Orbiter arrived in the Saturnian system in spring 2004 - almost 7 years after its launch. To gain velocity, Cassini swung around the inner Solar System twice and Jupiter once (figure 2.1) before zipping off towards Saturn at 70 km/s (Lorenz and Mitton, 2008). On December 25th, 2004, the Huygens probe detached from Cassini and moved into a Titanian orbit, and on January 14th, 2005 the Huygens probe descended into the dense atmosphere (Lebreton et al., 2005). The probe transmitted data for over 2 hours as it drifted through the atmosphere. After the probe successfully landed on the surface of Titan, it continued to operate for an additional 3 hours (Tomasko et al., 2005). The probe observed an apparent dendritic drainage basin that was imaged at various altitudes as the Huygens probe drifted towards the surface (figure 1.3).

Cassini left Earth with a large array of instruments designed to observe the surface and atmosphere of Titan along with other Saturnian moons and Saturn itself. Some of the objectives of the Cassini-Huygens mission at Titan include: (1) studying the constituent gases of the atmosphere; (2) finding the energy sources of the chemical reactions in the atmosphere; (3) studying aerosol properties and clouds; (4) measuring the temperature and wind velocity; (5) analyzing the surface and subsurface properties; (6) and investigating the upper atmosphere and ionosphere (Lebreton and Matson 2002; Matson et al. 2002). To accomplish these goals, 45 flybys were originally scheduled for Titan by the Cassini orbiter (Lebreton et al. 2005). Due to the great success of Cassini's observations, the project leaders agreed to extend the orbiter's observations of the system through the summer of 2010.

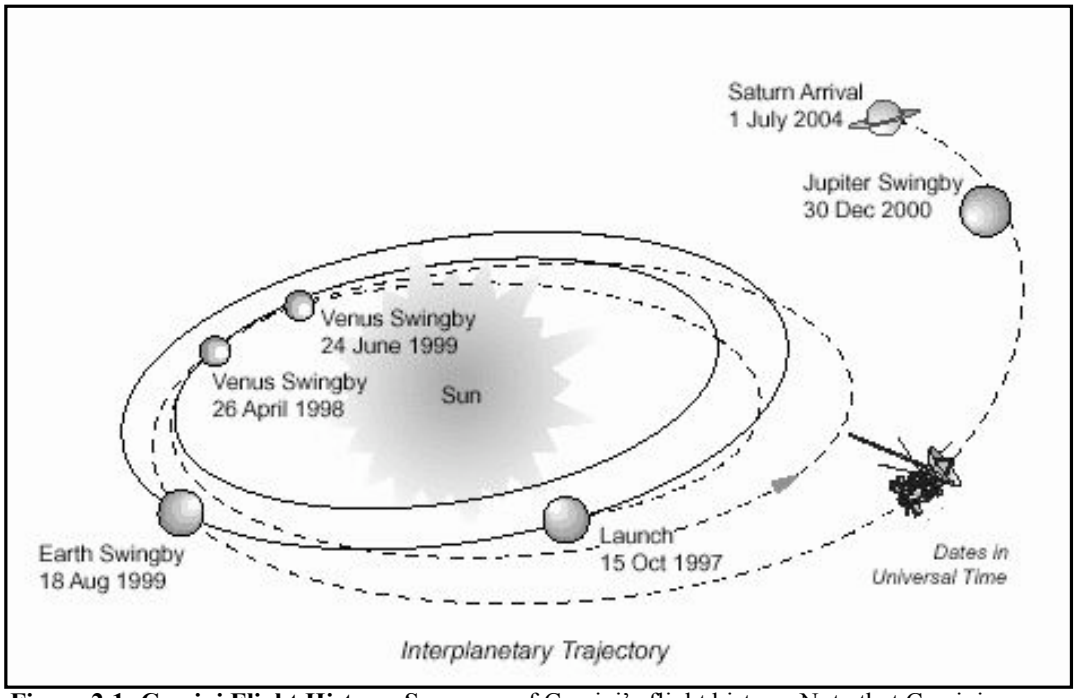

Figure 2.1: Cassini Flight History. Summary of Cassini's flight history. Note that Cassini swung around the inner Solar System twice before shooting off towards Saturn. **Source:** Federation of American Scientists **(**fas.org)

Figure 2.2: Cassini Pre-Launch. Cassini pre-launch. The 5.5 ton spacecraft is one of the largest payloads put into space by NASA. Source: NASA/JPL.

2.1.1: Cassini's SAR mode

To penetrate the haze filled atmosphere, Cassini's Titan Radar Mapper utilizes narrow atmospheric windows between thick methane bands (Paganelli et al., 2007). Cassini's Titan Radar Mapper has four modes: (1) radiometry; (2) scatterometry; (3) altimetry; (4) Synthetic Aperture Radar (SAR). The SAR mode of the Titan Radar Mapper operates in the K_u band (2.17 cm) with a spatial resolution of 0.35-1.7 km per pixel (Lebreton et al. 2005). The SAR system onboard Cassini requires close flybys of the target (within ~4000 km) in order to image properly; furthermore, for the higher resolution SAR images (~350 m/pixel), the Cassini orbiter must be within only 1500 km of its target (Elachi et al. 2005). Cassini's SAR mode makes observations at incidence angles between 15°-35°, and the resolution of each swath degrades towards the widening tips (Lorenz et al. 2008). The imagery used in chapter 4 of this document was gathered by the Titan Radar Mapper's SAR mode.

2.1.2: Sigma-naught and Dielectric constants

Radar systems produce images by measuring the microwave radiation that is returned (backscatter) from a target to the observing platform. Sigma-naught (σ°) is a computed coefficient that measures the strength of the backscatter returned radar pulse. In other words, the backscatter coefficient (σ°) is the quantification of the ability of an object or surface to scatter the incident radar signal. Multiple factors impact the strength of the backscatter returned from a target including surface roughness, moisture content, and the radar system parameters (Lillesand et al., 2008). Also, sigma-naught is related to the dielectric constant of an observed surface. The dielectric constant is a measure of the electrical conductivity of an imaged surface, and higher dielectric constants result in brighter radar returns. Water has a high dielectric constant (~80), but water ice (a major component of Titan's crust) is actually quite low. In fact, most of the materials

expected to reside on Titan's surface have low dielectric constants (table 2.1). Therefore, by determining the dielectric constant, it is possible to constrain what comprises an imaged surface (Lillesand et al., 2008).

Different materials have different dielectric constants, and the low σ° values recorded within numerous Titanian channels (>1 in some channels, Lorenz et al., 2008) are indicative of a low dielectric material – probably liquid methane. Furthermore, the radar-dark polar lakes (e.g. Stofan et al., 2007) have radar returns below the -25 dB noise floor of the instrument (i.e. below the lowest possible return that Cassini's radar can interpret). Paganelli and colleagues (2007) co-registered radiometric data with SAR images, and found that the temperature contrast between radar dark patches and the surrounding terrain is characteristic of a flat surface with a low dielectric constant in an icy terrain (table 2.1). Thus, given the expected, mostly radar-dark, composition of Titan's crust, brighter regions of the surface should be controlled by surface roughness and elevation to a large extent, and the darker regions of Titan might be covered by hydrocarbons with low dielectric constants.

Table 2.1: Dielectric Constants of Common Materials Expected to Reside on Titan's Surface

Material	Dielectric Constant
CH_4, C_2H_6, N_2 (liquid)	1.7 - 1.9
Solid Hydrocarbons	2.0 - 2.4
CO_2 Ice	2.2
H_2O Ice	3.1
NH_3 Ice	4.5
Silicates	~8
Liquid Water	~80

Lists a variety of compounds expected to reside on Titan's surface and their corresponding dielectric constants. Note that none of the materials have high values indicating a dearth of liquid water at the surface of Titan. Source: Jaumann et al. (2009).

2.1.3: Cassini's VIMS discovers evidence of liquid ethane

The Visual and Infrared Mapping Spectrometer (VIMS) utilizes near-infrared atmospheric windows at 2.0, 2.7, and 5.0 microns. VIMS data was used by Brown and colleagues (2008) to assess the composition of Ontario Lacus, which is a ~150 km across lake-like feature near Titan's south pole. By comparing the spectra of Ontario Lacus with a nearby area (with near-identical viewing angle) they found that at 5 microns, almost all incident photons are absorbed by the lake's interior, which suggests a smooth liquid surface (perhaps liquid ethane) because it is unlikely that a solid surface within the radar-dark spot could produce the same extremely low reflectance (Stofan et al., 2007). However, atmospheric methane is abundant near the surface of Titan, which complicates the identification of liquid hydrocarbons within Ontario Lacus because methane, in both its liquid and gas phase, shares similar rotational-vibrational spectra (Brown et al., 2008). Thus, the composition of Ontario Lacus is consistent with liquid alkanes (hydrocarbons with a single bond), but confirmation of such composition is difficult.

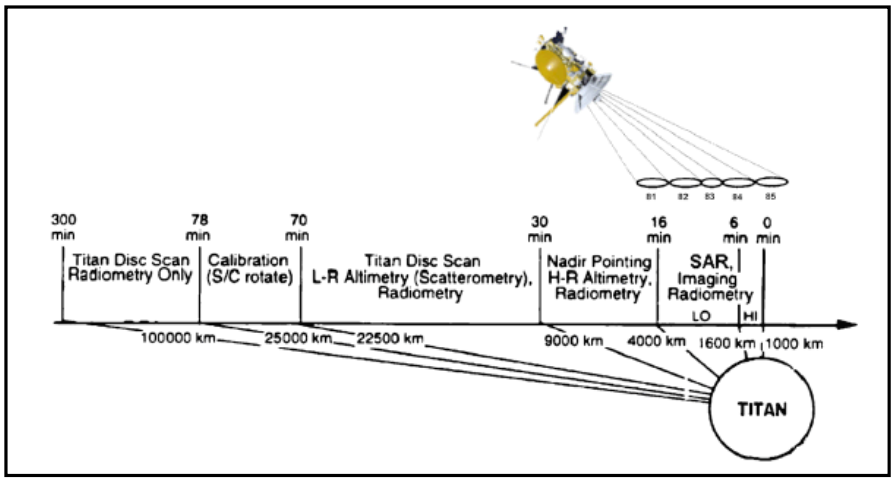

Figure 2.3: Summary of Cassini's Radar Capabilities. Displays distances to target required for the four modes of the Titan Radar Mapper. Source: Paganelli et al. (2007).

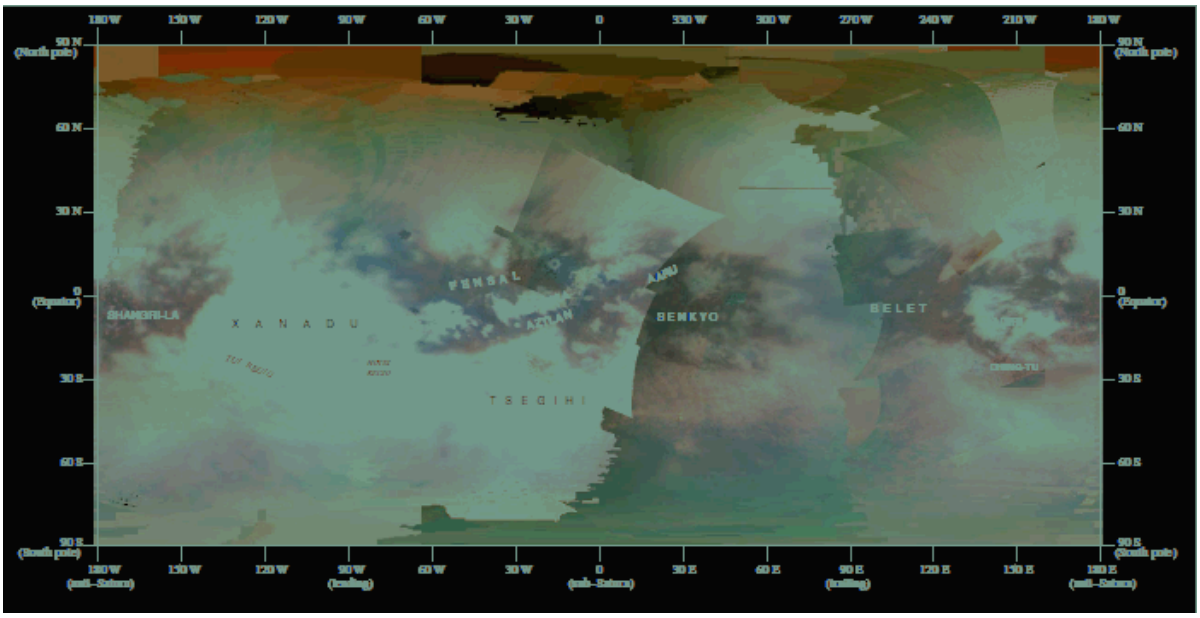

Figure 2.4: Global Map of VIMS Coverage. Source: NASA/JPL/UArizona, early 2008.

2.1.4: Flybys reveal Titan's surface in swaths

The flybys of Titan, which allow Cassini's SAR mode to record the surface in large swaths, have numerous titles depending on which department of NASA is considering the data, but the primary nomenclature labels each flyby as 'T1,' 'T15,' 'T30,' etc (exceptions like 'TA' exist, but most use T + number). The first close flyby by Cassini, referred to as TA, in 2004 sent back images revealing a varied and complex surface (Elachi et al. 2005). The third major look at Titan (after TA and Huygens descent) was the T3 flyby over the region called Xanadu - a large elevated plateau located around Titan's equator. On the T7 pass Cassini displayed deeply incised channels, and one area in particular (around 40°S) portrayed a dense network of channels (Lunine et al. 2008). Furthermore, on the same T7 run Cassini recorded what looks like dendritic features in the vicinity of Titan's south pole. On the T13 swath numerous channels were seen that drain southwards to develop into what looks like 6th and 7th order channels (Lorenz et al. 2008). On T16 and T18 the polar hydrocarbon lakes described by Stofan et al., (2007) were

spotted at 70°N and above. The potential lakes have a low backscatter (down to -25 dB), which is a radar trait typically displayed by the calm surface of a body of liquid (Hayes et al., 2008).

Figure 2.5: T28 Radar Swath. A cluster of polar seas were imaged on this flyby, indicated by dark spots towards the right end of the swath. The image varies from 200-500km wide and is over 6700km long. Source: NASA/JPL PIA 09217.

2.2: Terrestrial Observations of Titan

Before the 1990s, earthbound telescopes could resolve little detail from the tiny disc Titan presented. In 1990, the Hubble Space Telescope (HST) changed that with its ground-breaking imagery from orbit. With these images, it was possible to see brightness changes that Titan had undergone since the Voyager flybys of the early 1980s (Lorenz and Mitton, 2008). After inserting corrective optical elements for the primary mirror in 1994, the Titan images produced by HST improved considerably, and it was clear that hemisphere brightness variations suggested seasonal changes in the moon's atmosphere (Brown et al., 2002). Also, HST could view Titan in the near-infrared, which allowed it to penetrate the atmosphere, and in conjunction with the removal of atmospheric contribution in the data processing stage, allowed the creation of a coarse global map of Titan (Lorenz and Mitton, 2008).

Another prominent source of imagery that advanced into the 1990s was adaptive optics (AO). AO compensates for atmospheric distortion with a deformable mirror, which continually adjusts to create a clearer picture (Brown et al., 2002). AO systems use wavefront sensors, laser guide stars, control loops, and mirror actuators sharpen the picture producing a crisp Titan disk showing details of its surface and atmosphere. Once AO systems matured, the imagery in the

near infrared surpassed the capabilities of Hubble; however, Hubble still produced the best images in the visible and ultraviolet wavelengths (Meier et al., 2000). During the 1990s, Terrestrial observations of Titan's atmosphere at different wavelengths, probing different atmospheric depths, produced strong evidence supporting the existence of Titanian seasons, but a closer observational platform would be necessary to resolve the surface of Titan in the fine detail required by planetary scientists.

2.3: Liquid Methane on Titan's Surface

2.3.1: Obscured by haze

At longer wavelengths, Titan's haze scatters rather than absorbs; thus, small amounts of light manage to reach the surface. The haze's optical depth drops from several photon-haze collisions at 0.94 microns to ~0.2 collisions at 2 microns (Barnes et al., 2006); consequently, the haze layers makes Titan's surface darker and its atmosphere absorbent at UV wavelengths, but brighter and clearer at red and near-infrared wavelengths where fewer photons are absorbed by the haze. Furthermore, haze is evenly distributed at all heights, but methane is concentrated in the lower atmosphere (Lunine and Atreya, 2008). As a result, UV/blue light is absorbed in the upper atmosphere and red light to near-infrared can reach the surface and reflect back up. Infrared light is mostly absorbed by methane before reaching the surface. These viewing requirements focused the Cassini-Huygens developers to accurately describe the best near-IR wavelengths for viewing the surface with Cassini: 1.07, 1.28, 1.6, 2, 3, and 5 microns, which are narrow windows in between large methane absorption bands (Lorenz and Mitton, 2008).

2.3.2: From global hydrocarbon oceans to polar lakes

Before Cassini's arrival to the Saturnian system, many researchers proposed globally distributed hydrocarbon seas. The idea of liquid methane oceans originated because methane is known to be close to its triple point (~90K) on the moon (e.g. Lunine et al., 1983); as such, methane could easily change states and cycle through the atmosphere, lithosphere, or 'hydrosphere' of Titan. While no global ocean has been imaged, evidence of fluvial activity exists across Titan, especially at higher northern latitudes where large polar lakes and seas dominate the landscape (Stofan et al., 2007). Moreover, the largest polar sea (Kraken Mare) is estimated to contain more hydrocarbons than the entire known oil and gas reserves on Earth (Lorenz et al., 2008). While there is no evidence of liquid methane oceans on Titan, polar lakes around Titan's poles comprise some of the best evidence for the presence of liquid hydrocarbons stored at the surface, and replenished by precipitation and/or subsurface interaction with a liquid methane table.

Given the prevailing surface conditions, liquid methane can exist anywhere on Titan, but only at high latitudes is the relative humidity over 100% (Stofan et al., 2007), as such, liquid methane can accumulate more easily at higher latitudes due to the lack of a strong evaporative process. So far 655 lake features have been identified in the SAR dataset from 7 different flybys between July 2006 and May 2007, and all of the observed lakes are above 55^{o}N (Hayes et al., 2008). While some of the imaged lakes have dark, branching lines attached to them, which are assumed to be channels of fluvial origin (Stofan et al., 2007), the lines probably do not form the expansive network of channels that would be required to maintain the current lake levels if the visible surface channels were the only input to them. As such, the lake levels might be

maintained by contact with a subsurface liquid methane table in addition to a limited volume of precipitated hydrocarbons captured by surficial flow.

2.3.3: Polar lake classification describes by Hayes et al. (2008)

Polar lake appearances span a wide range of shapes but two basic morphologies are apparent: (1) large seas with rough coastlines and adjoining channel networks, some of which included what looks like 'drowned river valleys' draining into the seas; (2) small circular lakes that appear to be steep-sided (Hayes et al., 2008). The significance of the 'drowned' channel networks (see figure 4.10a for an example) surrounding the large polar seas is that these flooded drainage basins might be actively changing to fluctuating lake levels. In other words, the 'drowned' channel networks could be adjusting to a rising lake level that floods nearby channel networks resulting in the 'drowned' appearance as demonstrated in figure 4.10a. The potential for fluctuating polar sea levels is discussed in greater detail in chapter 5. The small rounded lakes could possibly have formed from impact basins, volcanic calderas, or even sinkholes; however, the clustered nature and small size of the circular patches makes the possibility of an impact craters origin unlikely (Stofan et al., 2007). Also, the rate of dissolution of water ice in liquid methane is expected to be a very slow process at the mean surface temperatures of Titan, and it is unlikely to aid much in the formation of these lakes.

Aside from visible, physical characteristics, the lakes can be classified on the basis of their radar reflectivity. Some of the lakes appear to be full; others look partially filled with radar bright areas around their edges (perhaps shallower regions of the lake) surrounding a darker center section (Stofan et al., 2007). The lakes can be broken down into three backscatter-determined groups: (1) dark lakes, which are seen above 65°N and occupy 15% of these high latitudes and are interpreted as being full of liquid hydrocarbons; (2) bright lakes, which possess

a backscatter equal to or higher than the surrounding area and are interpreted as 200-300 m deep empty basins; (3) granular lakes, which have a relative increase in backscatter compared to dark lakes, but without a distinct start/end in terms of where the granular lake become a dark lake or a bright lake (Hayes et al., 2008). Granular lakes are considered to be partially filled based on their backscatter signal and geographic location (Hayes et al., 2008).

Hayes and colleagues (2008) describe the lake classification system as follows: dark lakes comprise 394 of the 655 documented north polar lake-features, and account for 84% of total lake area across Titan with a mean surface area of 87 km^2. Of the total area covered by dark lakes, 73% is covered by large lakes (10^4 km^2 and up), and they are clustered for the most part between 0°E-140°E. Granular lakes reach latitude of up to 77°N, and account for about 6% of the total mapped lake area. Furthermore, granular lakes comprise 109 of the 655 total lake-like features mapped so far. Granular lake areas cover a mean of 147 km^2. Bright lakes account for 152 of the 655 total lake features mapped so far, which is equal to ~10% of the total lake area covering Titan. The areal distribution of the bright lakes has a mean of 273 km^2. Bright lakes are radar bright in both nadir and off-axis backscatter measurements; in other words, the bright lakebeds have a similar roughness to the surrounding area, but some sort of thin layer covering the bright lake basins distinguishes them from the surrounding area. While the polar seas are large radar-dark features, many of the 'full' hydrocarbon lake are in fact small circular lakes; as a consequence, the mean surface area of the radar-dark lake category is lower than the partially filled and empty lakes comprising the other two classifications.

2.3.4: Estimation of lake depth utilized by Paillou et al. (2008)

In order to decipher the radar response of Titan's lakes seen in flyby T16 and others, the dielectric constant of liquid hydrocarbons is a necessary parameter. The dielectric constant

controls attenuation (related to penetration depth) of radar waves and the reflectivity of the observed surface (Paillou et al., 2008). To estimate the dielectric constant of liquid methane seen in polar lakes during flyby T16 (the radar swath that uncovered lakes, Stofan et al., 2007), experiments were conducted on Earth using purified liquefied natural gas (LNG), which is 90% liquid methane and stored at temperatures (110 K) comparable to the surface of Titan (Paillou et al., 2008). After conducting multiple tests, the workers measured both the reflection and transmission coefficients. These calculations led to a dielectric constant for the LNG of [$\varepsilon = 1.75 - 0.0002$ j]. This dielectric constant value produces a skin depth of 2.2 m at the 13.78 GHz frequency of Cassini's radar equipment (Paillou et al., 2008). In other words, Cassini can penetrate at least a couple of meters into the radar-dark patches.

To test the dark patch penetration limits of Cassini's radar, Paillou and colleagues (2008) devised a two layered approach to interpreting the reflectance of the lakes. One layer possessed the dielectric constant of LNG [$\varepsilon_1 = 1.75 - 0.0002$ j] to represent surface reflectance, and a related deeper layer represented the dielectric constant of the lake bottom [$\varepsilon_2 = 2.20 - 0.01$ j]. The researchers then calibrated the two layer model with roughness parameters produced from two extreme examples of lake backscatter recorded on the T16 flyby [-25 dB (dark lake) and -11 dB (bright lake)]. The researchers then fixed these roughness values to apply to all cases in order to calculate hypothetical backscatter values for a variety of lake depths. It is important to note that the incidence angle (workers used a mean of 33^o) of the radar is a key factor in the hypothetical backscatter determination because lower incidence angles lead to more backscatter off dark lakes. For example, a mean incidence angle of 33^o, with a detection limit of about -27 dB means that Cassini's radar could penetrate up to 7 m of liquid methane for the imaged lake (Paillon et al., 2008).

Once this method was applied to all 77 lakes depicted in the T16 swath, two classes of lakes came into focus: (1) lakes with backscatter lower than -22 dB, which have a depth greater than 3 m; (2) lakes with backscatter higher than -19 dB, which have a depth less than 2m (Paillou et al., 2008). This correlation between backscatter values and depth can be adapted to lake area as well. The darker lakes (-22 dB and lower) correspond to larger lakes with an area over 100 km^2 while the brighter lakes (-19 dB and higher) match up with smaller lakes with an area under 50 km^2 (Paillou et al., 2008).

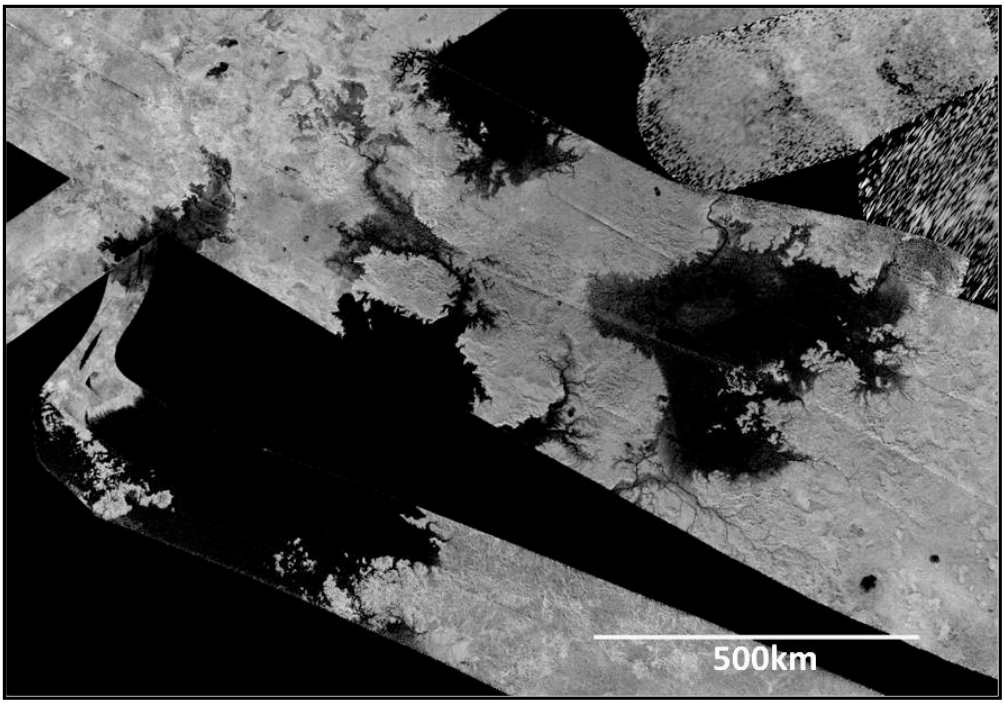

Figure 2.6: North Polar Seas. North polar radar swath mosaic showing the area dominated by large polar seas. Note the rough coastlines and dark channels draining into the seas. Source: Cassini Radar Team.

2.4: Atmospheric Methane Replenishment

The inventory of liquid hydrocarbons on Titan is sufficient to replenish the methane rich atmosphere via evaporative fluxes on timescales shorter than methane is removed from the atmosphere by photochemical depletion (Mitri et al., 2007). However, there is about an order of magnitude more methane in the atmosphere than there is on Titan's surface, and according to

current photochemical models, this means Titan would run out of surface methane within 10 million years (Lorenz et al., 1997). Because methane is not only present but abundant in Titan's atmosphere, some combination of other factors must be maintaining Titan's methane cycle. Titan's interior may add methane to the surface-atmosphere system (Tobie et al., 2005) via cryovolcanic activity or outgassing of subsurface organics. Volcanic-like features imaged with radar and the visible and near infrared spectrometer across different parts of Titan suggest that cryovolcanism plays some sort of role (Stofan et al., 2007). It is also possible that the photochemical models currently used produce incorrect timescale calculations for the exhaustion of atmospheric methane on Titan (Lorenz et al., 2008). Alternatively, there it is the possibility that Titan has undergone long periods in the past where it had no hydrocarbon cycle and had a much thinner atmosphere (Sotin et al. 2005). While each of these explanations has merit, it seems most likely that an undetected subsurface reservoir aids in the long-term sustainability of atmospheric and surface methane stocks (Niemann et al., 2005) given the evidence for a fluctuating alkanifer that is believed to maintain the north polar lake levels (Mitchell et al., 2009). By extension, this alkanifer might replenish atmospheric stocks of methane by adding trapped deposits of methane into the surface-atmosphere cycle. A more detailed discussion of a possible fluctuating hydrocarbon table is included in chapter 5.

2.5: Estimation of Precipitation Regimes

Liquid methane precipitation might only reach the surface of Titan when the base of precipitating clouds are relatively low, or rainfall might reach the surface only during longer precipitation events (Perron et al. 2006). Rain drops that fall early on during a storm could evaporate before hitting the surface, which increases the relative humidity of the atmosphere

between the cloud base and the ground sufficiently to reduce further evaporation of subsequent drops (Lorenz, 1993). Most images of Titan displaying large clouds are concentrated over the hemisphere receiving the most insolation (i.e. the summer hemisphere - Griffith et al., 2006). Coalescing and dissipating clouds (figure 2.7) on Titan were first identified from earthbound observations around Titan's south pole (Griffith et al., 2000). The rate at which the south polar clouds seem to form and dissipate (e.g. Rannou et al., 2006) suggests that these are large convective storms precipitating condensed methane onto the surface.

Precipitation models, (e.g. Hueso and Sanchez-Lavega, 2006; Barth and Rafkin, 2007), predict the existence of storms capable of producing tens of kg/m^2 around the subsolar point (Mitchell, 2008). Hueso and Sanchez-Lavega (2006) showed that the initiation of convective activity could occur with relatively slight manipulations (i.e. 1 K temperature change, 1 m s^{-1} vertical velocity increase, etc) where conditions of 'high-relative-humidity' prevail (RH >80%). Furthermore, the researchers' model indicated that the typical lifecycle of a liquid methane convective storm was about 10 hours from the initial growth phase, to a mature phase (when most of the rainfall occurs), to the dissipation of the clouds. These convective methane storms released an amount of liquid comparable to rain storms on Earth (~100 kg m^{-2}). The researchers' model could not account for the tallest cloud plumes observed on Titan at the time of their study (~40 km at 40°S) even when they adjusted the relative humidity from 50% to 95%. Hueso and Sanchez-Lavega (2006) suggest that perhaps the atmosphere is significantly less stable at 40°S than at the Huygens landing site, which is major source of data concerning the atmospheric composition of Titan.

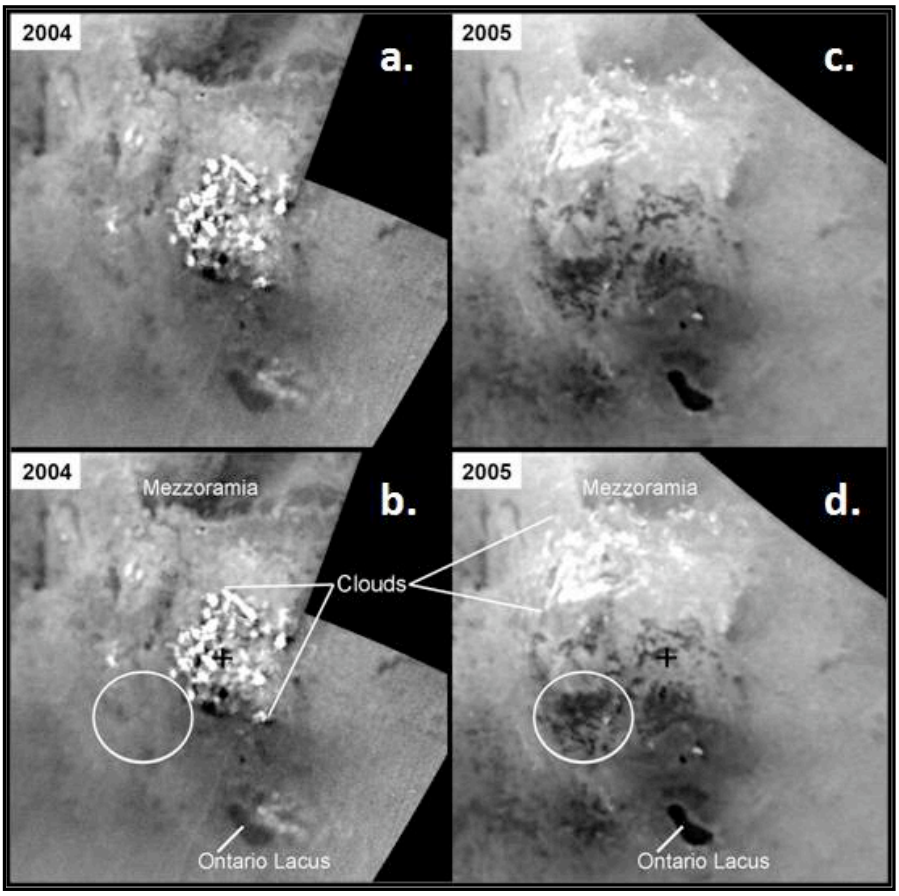

Figure 2.7: Evidence of Liquid Ethane. (a and **b)** acquired July 3, 2004. **(c** and **d)** acquired June 6, 2005. In **c** and **d**, new dark areas are visible, suggesting that precipitation has filled the area. The very bright features are clouds in the troposphere. Source: NASA/JPL, PIA 11147.

As the winter hemisphere air circulates down from the stratosphere, it becomes heated through compression, and prevents the formation of methane clouds (Griffith et al., 2006). However, close to Titan's arctic circle (51°-68°N and perhaps further north but a lack of illumination prevents observation) a bright band (i.e. a cloud) appears in the data recorded by Cassini's VIMS (Brown et al., 2008). In contrast to the large convective clouds imaged over Titan's south pole, this northern cloud is not dissipating and is spread over a large area (Griffith et al., 2006). The latitudinal location of the cloud is where photochemical products (principally ethane) are expected to be concentrated as they descend to lower altitudes where they condense to form clouds (Rannou et al., 2006). The cloud was confined to an altitude range of 30-50 km

with no trace of the cloud above 60 km. Additionally, the northern cloud forms at altitudes where the mixing ratio for ethane surpasses the threshold for saturation, and the unvarying nature of the cloud is supported by the slow fall velocities for particles of similar size to the ones observed in the cloud (~3 km per month) (Griffith et al., 2006). Thus, is it likely that ethane condenses at arctic latitudes where global circulation models predict a downwelling of hydrocarbons (principally ethane) from the stratosphere to the surface. As molecules of ethane descend to ~30-50 km, they condense and form the somewhat static cloud observed by Cassini's VIMS.

Therefore, the data suggests that rapidly forming and dissipating methane clouds form over the summer hemisphere, and stable ethane clouds form over the winter hemisphere. The processes leading to the formation of the stable ethane cloud over the winter hemisphere are poorly understood; however, it is possible that the photochemical removal of methane, driven by heightened numbers of solar photons over the summer hemisphere, leads to increased amounts of atmospheric ethane – the principal byproduct of methane destruction (e.g. Yung 1984). This ethane and other hydrocarbons might be transported to the opposite hemisphere via a single pole-to-pole circulation cell transporting rising warm air from Titan's summer hemisphere to its winter half. The underlying dynamics of this circulation cell, and whether it transports significant amounts of hydrocarbons from one pole to the other, requires further observations to establish its basic functions.

2.6: Surface Composition, Possible Dissolution

The bright regions of Titan's surface are likely comprised of exposed water-ice bedrock mixed with small amounts of hydrocarbon impurities creating 'dirty-ice' (Tomasko et al., 2005). Furthermore, surface albedos at 1.28, 1.58, and 2.0 microns correspond to the spectra of both water-ice and solid organic sediments (Griffith et al., 2003), which suggests that the bedrock of

Titan (thick layers of water-ice) are exposed at the surface while precipitated organic material covers other the darker portions of the moon (e.g. Lorenz and Lunine, 1997). The precipitated atmospheric particles slowly drift down to the surface as complex hydrocarbons, and over the course of Titan's geologic history, these particles could form a layer of organic materials 10-100 m thick over a water-ice bedrock layer (Hayes et al., 2008). The brighter regions must have been 'washed clean' within the past $10^4 – 10^5$ Earth years, which is the approximate amount of time required for a layer of precipitated organics several 100 microns thick to form on the surface (Smith et al., 1996). Alternatively, new formations of water-ice bedrock could be brought to the surface by cryotectonic activity. Further discussion of the evidence supporting tectonics on Titan is included in chapter 5. As such, available evidence suggests that Titan's surface has a frozen bedrock layer covered with an unknown depth of precipitated organics.

Lorenz and Lunine (1996) calculated the solubility of water and ammonia ices in CH_4 and C_2H_6. Their results showed that the dissolution of pure water-ice in liquid methane or ethane at 94 K is extremely limited, and only a fairly minor amount of dissolution is possible on Titan over the course of the Solar System's past (Lorenz and Lunine, 1996). While the dissolution of pure ammonia-ice in liquid CH_4 at 94 K might be similar to $CaCO_3$ in liquid water on Earth, the uncertainty in the calculations suggests that the dissolution of ammonia-ice could be up to three times less (Perron et al., 2006). Furthermore, ammonia on Titan is found primarily in the form of ammonia-water hydrates, which have poorly understood solution properties (Perron et al., 2006). Therefore, dissolution of water-ice in liquid methane is a very slow process, and is unlikely to function as a major geomorphic force on the surface of Titan.

2.7: Sediment Supply and Transport

Sediment falls at a slower rate (factor of 3-4) through the fluid column on Titan versus Earth due to the disparity in the effectiveness of gravity on the surface of the two worlds (Burr et al. 2006). The diminished gravity of Titan is partially offset by the lower absolute viscosity of liquid methane ($2x10^{-4}$ Pas) when compared to liquid water ($1x10^{-3}$ Pas). Additionally, Burr and colleagues (2006) point out that water-ice has a specific gravity of 2.06 in liquid methane while quartz in water has a specific gravity of 2.65. Thus, sediment on Titan is slightly more buoyant. The enhanced buoyancy of water-ice sediment and lower gravity on Titan means that sediment grains should become entrained in lower fluid depths than on Earth (e.g. Perron et al., 2006); additionally, flow velocities at the moment of entrainment will be lower than on Earth. These factors lead to sediment transport in smaller discharges on Titan for a given grain size in channels with similar geometry and basin size (Perron et al., 2006).

Collins (2005) compares the fluvial incision processes on Earth to what might be happening on Titan. He suggests that fluvial channels might be made by bedrock incision if the surface of Titan is mostly water-ice, or if the surface is composed of a loose regolith, then the removal of sediment would lead to channel formation (assuming the precipitation rate of liquid methane exceeded infiltration rates into the loose regolith). Furthermore, the rapid removal of impact craters, in comparison to the timescales involved in resurfacing on other Saturnian satellites, suggests that processes related to fluvial erosion are not only occurring on Titan, but do so on fairly regular time intervals (Collins 2005). Furthermore, Perron et al. (2006) showed that sediment transport models for Titan predict precipitation rates of 0.5-15 mm an hour would be enough to move sediment with grains 1-10 cm in a channel, which would be comparable to the size of the cobbles seen in the pictures taken after Huygens had landed (Tomasko et al.,

2005). Where unbroken blocks of water-ice bedrock appear at the surface of Titan (as opposed to a loose regolith of precipitated organics), infiltration rates are probably low (Perron et al., 2006). Furthermore, without the presence of vegetation to decrease the velocity of hydrocarbon flows and promote infiltration, runoff could potentially reach flash flood conditions – similar to arid environments that experience infrequent precipitation events on Earth.

Thus, for a given shear stress, Titan is able to transport larger sediment particles than fluvial systems on Earth (Collins 2005) due to the slower fall velocity stemming from Titan's gravity. While less gravity on Titan leads to larger sediment size entrainment for a given flow, the diminished gravity also dampens sediment transport because Titan's lower gravity requires steeper slopes and/or greater flow depths in order to acquire the same shear stress as a stream on Earth (Collins 2005). Once all of the effects of Titan's gravity and differences in sediment composition are taken into account, the diameter of water-ice sediment on Titan able to reach thresholds for transport for a given flow depth and slope are about two times the possible diameter of quartz sediment on Earth (Collins 2005).

2.7.1: Bedrock incision

Saltating grains of sediment may chip off small pieces of bedrock in stream channels on Titan. Sklar and Dietrich (2004) developed a model to emulate erosion by bedload. While larger grain sizes can be entrained on Titan for a given flow compared to Earth, the lower gravity and smaller sediment densities reduces the impact force of sediments on Titan. In other words, grains with equal diameters falling through a given depth of fluid will exert less force on their bed on Titan than on Earth. However, initial experiments performed by Collins (2005) that measure the abrasion resistance of water-ice bedrock (chilled to 200 K) impacted by a variety of grains (ranging in mass from 2-8g) show that water-ice is about half as resistant to abrasion as rock.

This lower resistance to abrasion by water-ice negates the reduced impact force of sediments on Titan, which brings erosion rates on Titan for a water-ice carved channel close to erosion rates on Earth for a stream carved into sandstone (Burr et al., 2006). However, the mean surface temperature of Titan is close to 94 K, which should enhance the resistance of water-ice to abrasion. Further analysis of the properties of water-ice at very low temperatures is needed to better understand its ability to resist abrasion.

At low discharges, erosion is minimal since the sediments are immobile on the bed. At higher discharges, erosion rates decrease as a larger percentage of available sediment is entrained as suspended load (Collins 2005). Thus, peak erosion rates happen for smaller discharges on Titan versus Earth because lower shear stress is needed to move water-ice sediment, and transport stage is always higher on Titan for a given sediment size and a given discharge (Collins 2005). The presumed lower resistance of water-ice to abrasion and the larger amount of sediment in suspension for a given flow on Titan versus Earth combine to suggest that the rate of erosion caused by suspended sediment should be higher on Titan. However, Whipple et al. (2000) argue that erosion carried out by the suspended load will scale with flow velocity, and Titan's lower gravity reduces flow velocity. On Titan, the higher transport stage would make it easier to move large blocks while the poor tensile strength of water-ice would promote fracturing in the bedrock (Collins 2005). These factors could combine to lead to higher rates of plucking on Titan (assuming an adequate supply of blocks is available to be transported as solid pieces), and to more effective transport of large blocks for a given flow versus Earth.

Therefore, fluvial erosion rates are probably similar on both Earth and Titan; however, it seems clear that further research is required in order to better define the parameters of sediment transport on Titan. Furthermore, large precipitation events, leading to overland flow and the

initiation of channelized flow, are probably infrequent, but intense and short lived when they do occur (Lorenz et al. 2005). Therefore, fluvial erosion on Titan might be a significant driving force for change on the surface of Titan, but these changes probably materialize in rapid bursts of activity that are separated by longer dry periods similar to arid environments on Earth.

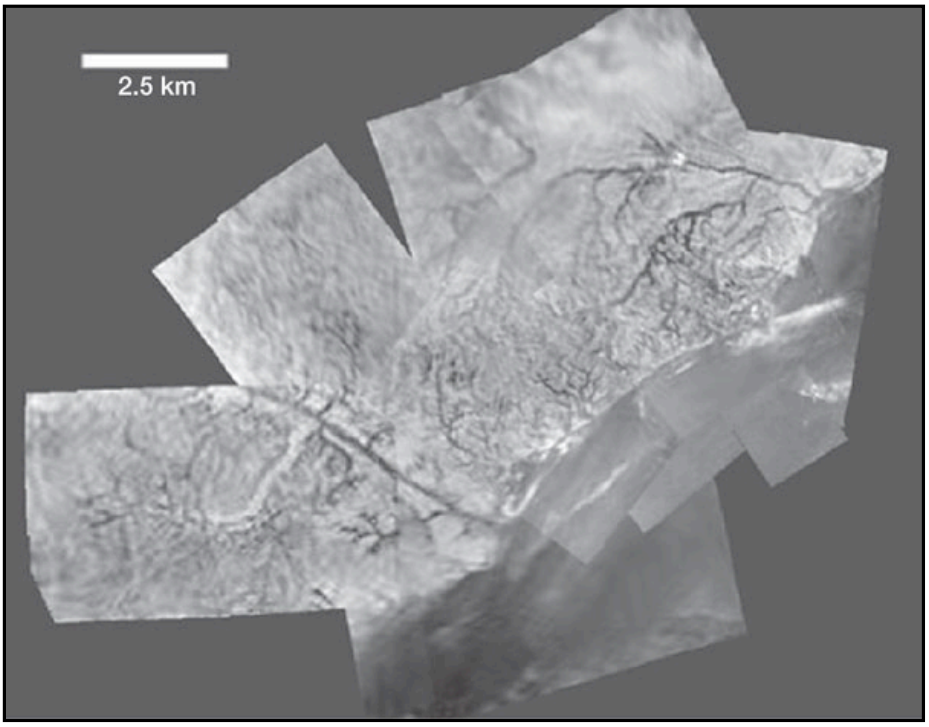

Figure 2.8: Drainage Basins Close to Huygens Landing Site. Mosaic of two channel networks just north of the Huygens landing site. Source: Tomasko et al. (2005).

CHAPTER 3.

INVESITGATION OF CRITICAL FLOW DEPTHS AND DENUDATION RATES IN A NORTH POLAR DRAINAGE BASIN

3.1: Introduction

Titan presents researchers with a tantalizing opportunity to observe fluvial processes outside the confines of the terrestrial planets. Before the Cassini Orbiter arrived in the Saturnian system, many researchers (e.g. Lunine et al., 1983) speculated that a global methane and ethane ocean, over a kilometer deep, could cover the surface of Titan. While there is no evidence of a global ocean on Titan, the possibility of liquid methane precipitation reaching the surface has been strongly reinforced by the channel networks (e.g. Barnes et al., 2007) and polar lakes (Stofan et al., 2007) apparent in the radar data. Thus, it is likely that runoff from liquid methane storms carves channel networks into the water-ice crust of Titan; subsequently, grains of water-ice are entrained as bedload.

The existence of channels on Titan is apparent in the SAR images gathered by Cassini; however, the relationship between these liquid methane-cut channels and the surrounding terrain is poorly understood. Overlapping flybys covering portions of Titan allow for the generation of digital terrain models (DTMs) like PIA 10353 (portion of DTM in figure 3.1) that displays the topography of an area relative to the radius of Titan (~2575 km). With the elevation data provided by PIA 10353, it is possible to calculate the slope in different parts of the polar landscape. Once the slope of a particular region is known, various measures describing the sediment transport capacity of that area can be calculated. Within the area covered by PIA 10353 (overlapping portions of T25 and T28 radar swaths) are several channel networks that drain into

a nearby branch of Kraken Mare. One of these channel networks is a large basin (~1865 km^2) with a dendritic morphology (referred to as Basin A, discussed in chapter 4).

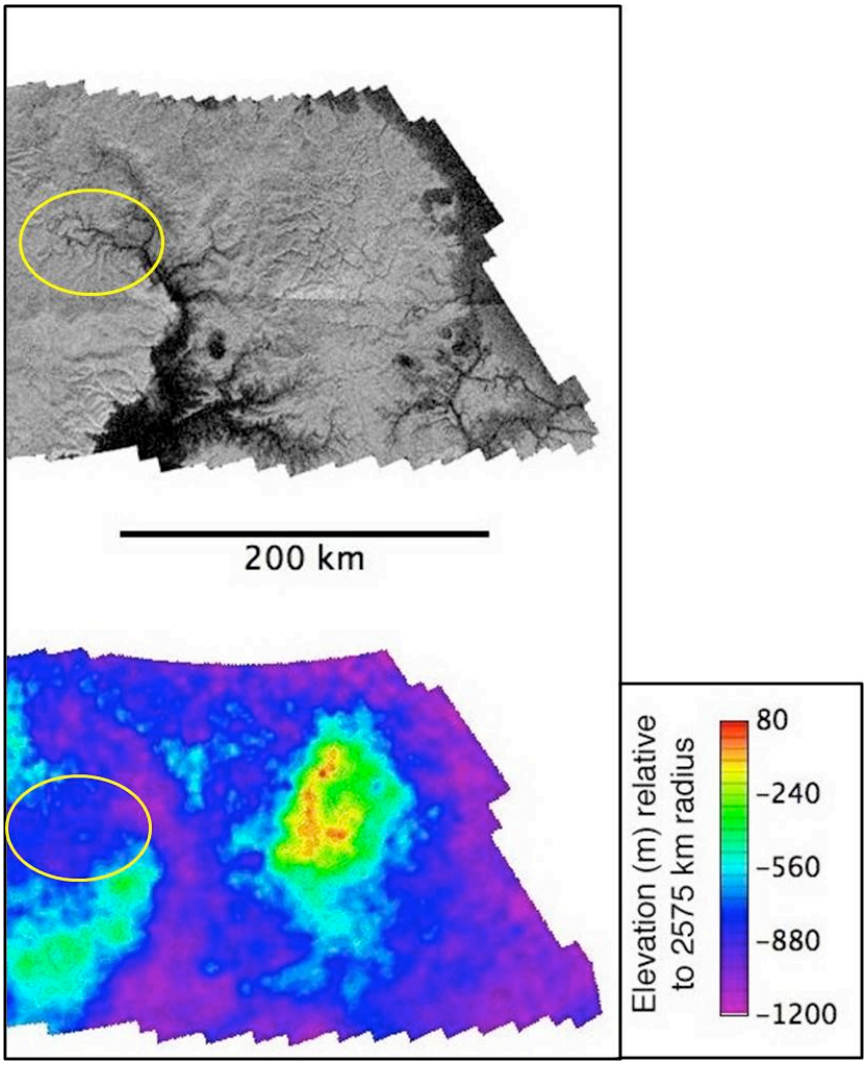

Figure 3.1: Topographic Map of Kraken Mare 'Estuary.' Right most portion of the original PIA 10353. The scale bar on the right displays the elevation relative to the radius of Titan. Area within yellow circle indicates location of Basin A. Source: NASA/JPL/USGS (2008).

This chapter investigates the slope in three regions of the dendritic basin (called 'Basin A'), and focuses on the critical flow depths and critical Shields stress values required to entrain water-ice grains in the three regions (headwaters, midstream, and downstream) of the Basin A. The resulting critical flow depths are compared to those described in Burr et al. (2006), which

details an assortment of sediment transport thresholds for the expected surface conditions on Titan. Furthermore, a denudation rate for each zone of Basin A is also calculated. The denudation rate describes the minimum amount of time required for a given basin to erode down to base level. Therefore, the denudation rate provides an estimate for the amount of time fluvial processes require to resurface their surroundings.

3.2: Background

3.2.1: Overlapping radar observations

Titan's residence in the outer Solar System, coupled with its dense atmosphere, limits Terrestrial observations of the moon. The Cassini orbiter, cruising through the Saturnian system, provides a much closer observational platform from which to study Titan. Cassini is equipped with an array of instruments capable of penetrating the dense atmosphere of the moon by manipulating narrow atmospheric windows between large methane bands at near-infrared and longer wavelengths (e.g. Porco et al., 2005). The SAR mode of Cassini's Titan Radar Mapper produces swaths with the finest surface resolution possible of any Cassini instrument. Such exquisite views of the frigid satellite require that the orbiter comes to within ~4000 km from the surface (Pagenlli et al., 2008). Fortunately, Cassini can dip as close as ~1000 km from the surface – just above the upper reaches of the atmosphere.

The Cassini orbiter's SAR mode collects data in large radar swaths as it passes Titan. Each pass is called a 'flyby,' and given a flight name: T0, T1, T18, T41, etc. Where overlapping coverage of the Titanian surface occurs, it is possible to generate a digital terrain model (DTM) that describes the topography of the region. One such topography map was produced and released to the public by NASA (PIA 10353). In this image (figure 3.1), overlapping flybys

allowed for stereopair analysis of a ~200 km wide and ~1700 km long span of Titan's polar surface. Several channel networks are contained within the stereo paired region, and as such, the slope of these basins can be assessed using the available elevation values. The intricacies of PIA 10353 are discussed in the final section of this chapter.

3.2.2: Sediment transport on Titan

The probable sediment sources on Titan range from finer grained organic particles to coarser chunks of water-ice bedrock. Ground-based spectra of Titan (e.g. Griffith et al., 2003) suggests that the moon's crust consists predominantly of water-ice bedrock (Lunine and Atreya, 2008). Organic matter, formed by photolysis in the upper atmosphere, slowly drifts down to the surface (Thompson, 1984; Tran et al., 2003; Lorenz and Lunine, 2005). These precipitated particles are complex hydrocarbons, and over the course of Titan's geologic history, atmospheric particulates could form a layer of organic materials 10-100 m thick over a water-ice bedrock layer (Atreya, 2007; Hayes et al., 2008). Even after considering the possible removal of precipitated organics by a variety of liquid methane conduits (Burr et al., 2006), or the cryovolanically-driven burial and subsequent storage of precipitated organics (principally ethane) in a porous regolith (Mousis and Schmitt, 2008), it seems likely that much of Titan's surface still retains some unknown depth of accumulated atmospheric particles (Atreya, 2007). As such, the available evidence suggests that Titan's surface has a frozen bedrock layer covered by a variable depth of precipitated organics.

Table 3.1: Sediment Transport Terms

ρ (kg/m^3)	450	Liquid CH_4	*Burr et al. (2006)*
ρ_s (kg/m^3)	992	H_2O-ice	*Lorenz et al. (2003)*
g (m/s^2)	1.35	gravitational acceleration	e.g. *Collins (2005)*
D_{50} (m)	0.075	midpoint H_2O-ice grain size	e.g. *Tomasko et al. (2005)*

Important values used to define a variety of terms in the sediment transport formulas used in this chapter.

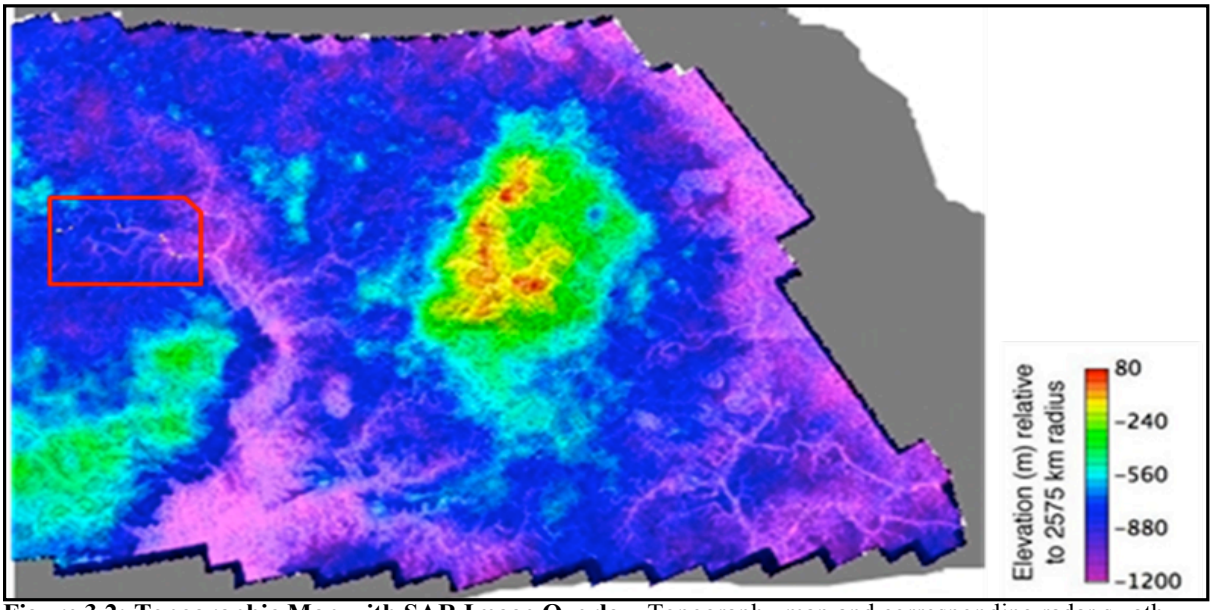

Figure 3.2: Topographic Map with SAR Image Overlay. Topography map and corresponding radar swath blended illustrating how the branch of Kraken Mare fits nicely into the low-lying areas (purple) while the surrounding terrain displays higher elevation values (dark blue to red). Basin A is contained with the red box. Adapted from: NASA/JPL/USGS (2008).

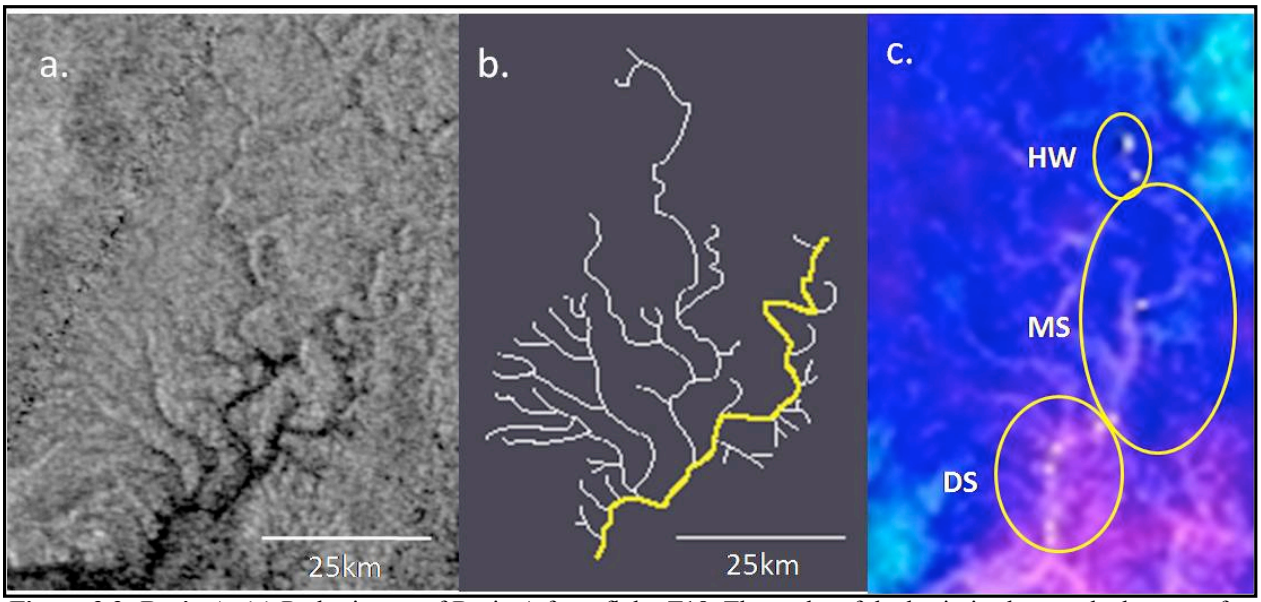

Figure 3.3: Basin A. (a) Radar image of Basin A from flyby T18. The outlet of the basin is close to the bottom of the image (on the left-hand side). **(b)** Channel network of Basin A. The yellow channel highlights the flow path from which the slope calculations were made. Further explanation of (b) is forthcoming in chapter 4. **(c)** blend of PIA 10353 and radar image of Basin A. HW (and adjacent yellow circle) represents the headwaters section, MS is the midstream (within adjacent yellow circle), and DS is the downstream section of Basin A (within adjacent yellow circle). Dots within each circle represent changes in elevation along the course of the channel.

For a given shear stress, Titan is able to transport larger sediment particles than fluvial systems on Earth due to Titan's substantially lower gravity (1.35 m/s^2) and the higher buoyancy of water-ice in liquid methane versus quartz grains in liquid water (Collins 2005). While less gravity on Titan leads to larger sediment sizes capable of entrainment for a given flow, the diminished gravity also retards sediment transport because Titan's lower gravity requires steeper slopes and/or greater flow depths in order to acquire the same shear velocity as a stream on Earth (Burr et al., 2006; Collins 2005). Once Titan's gravity and the potential composition of sediment sources are taken into account, the entrainment thresholds for a range of grain diameters at a given flow depth and slope are lower than the thresholds for sediment entrainment on Earth (Collins 2005).

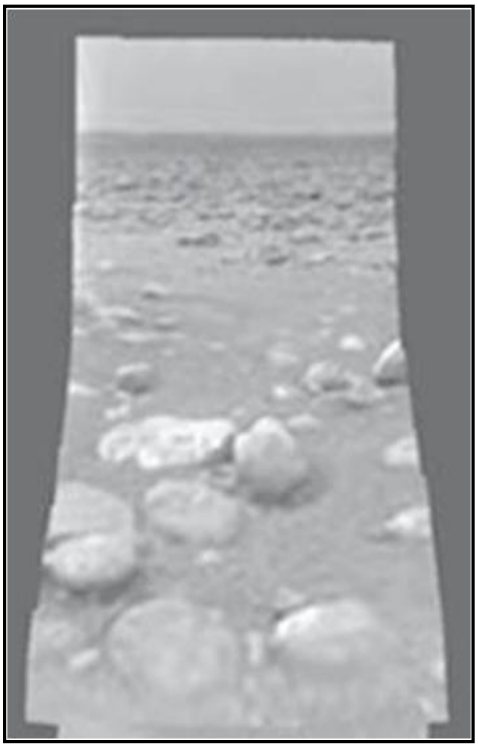

Figure 3.4: Potential Sediment Source at Huygens Landing Site. Image recorded by the Huygens probe after landing. A variety of well-rounded 'cobbles' are visible in the foreground. Note that many of the cobbles (assumed to be comprised of water-ice) are partially buried in what looks like sand (most likely organic particles). Source: Tomasko et al., (2005).

3.2.3: Bedload sediment sources

This study is principally concerned with the initiation of bedload transport for water-ice grains because channel morphology is mainly a function of bed load transport (Leopold, 1992). The only evidence available to constrain water-ice grain sizes was recorded in images taken by the Huygens probe after landing (figure 3.4). The landing site images provide examples of what look like 'cobbles' probably composed of water-ice and coated in organic particulates (Tomasko et al., 2005). The cobbles range in size from ~3 mm (the resolution limit of the imager) to 150 mm and appear to be well-rounded and partially buried (Tomasko et al., 2005). This study uses a similar range of grain sizes (1 mm - 150 mm) in subsequent calculations. The midpoint grain size of this study is an important value used in a variety of formulas that drive at interpreting the sediment entrainment potential of the three zones in Basin A (see equ. 3.1, 3.3, 3.6, etc).

3.2.4: Precipitation regime and north polar climate

Precipitated hydrocarbons (principally methane and ethane) likely replenish the liquid hydrocarbon lakes via summer convective storms (Griffith et al., 2006). Several researchers have created precipitation models for Titan, which predict the occurrence of intense methane storms stemming from convectional heating of moist parcels of air (Hueso and Sanchez-Lavega, 2006; Barth and Rafkin, 2007). It is important to note that no methane laden convective storms have thus far been imaged in the winter hemisphere (currently the north pole of Titan - Rannou et al., 2006), although there is a stable ethane cloud over the winter pole. However, once summer heating reaches the high northern latitudes around the pole (sometime in 2016), convective storms should form over the region, bringing tens of kg/m^2 of rain (e.g. Barth and Rafkin, 2007) during large precipitation events. As such, precipitation models designed for the south pole (fading summer hemisphere) should be applicable to the north pole as well.

The precipitation regime at the poles should be different from the global mean because there is a higher relative humidity at the poles stemming from the 2-3 K lower temperatures predicted to prevail at polar latitudes (Hayes et al., 2008). Furthermore, Titan has an obliquity of ~26.7^{o}, which leads to increased insolation over the summer hemisphere (i.e. the half of the moon tilted towards the Sun). The increase in convective storms is especially pronounced at the summer solstice (Brown, et al., 2002). Given these factors, it is expected that precipitation rates are higher at the poles than in the equatorial regions (where the Huygens landing site is located). Perron et al. (2006), using a model generated from small terrestrial drainage basins, suggest that the minimum amount of precipitation needed to transport sediment grains similar to the sizes imaged by the Huygens probe (10-100 mm grain diameter) is 0.5-15 mm hr $^{-1}$. While steeper slopes are required on Titan (versus Earth) to transport similar sediment loads (Burr et al., 2006), areas of higher topography (>500 m) might experience significantly more precipitation (Lorenz, 1993). Consequently, the areas of higher topography surrounding the polar lakes might capture substantial amount of rainfall (at least during the Titan summer), leading to flows deep enough to surpass any entrainment threshold imposed by the range of grain sizes seen at the Huygens landing site.

3.3: Methods

3.3.1: Assessment of slope at Basin A

PIA 10353 (figure 3.1) provides elevation values for a section of Titan's north polar Lake District. Basin A lies within this region, and its slope was assessed using the available topography data. First, I subset the radar image (top swath of figure 3.1) and placed it underneath the topography data (bottom swath of figure 3.1) creating a blended image (figure 3.2) that

shows the relative elevation of the areas surrounding a branch of Kraken Mare. Importantly, the blended image showed that the topography map fit quite well with the radar image of the same area; in other words, the lakes and seas fit into the low lying areas of the topography map, and the surrounding terrain corresponds with the areas of higher relative elevation in figures 3.1 and 3.2. The two images do not fit perfectly on top of each other, leading to slight differences along the edges of both swaths. However, the fit is better toward the middle of the images making it possible to assess the topography of the region over larger distances (>5 km).

The slope of Basin A is an important value that helps constrain a series of sediment transport calculations (see next sub-section). In order to find the slope, elevation variations over a long channel that drains from the headwaters to the outlet of Basin A was selected, and elevation changes were recorded along its flow path. Elevation variations in PIA10353 are displayed as simple color changes on a scale separated into sections. The total relative elevation displayed on the scale (1280 m) divided by the number of sections (25) equals the elevation change from pixel to pixel color shifts (i.e. 51.2 m increase/decrease in elevation per change in color). Therefore, where the color of the topography data changed distinctly, a point was made on the image. Over the course of the channel, 10 points (9 slopes) were recorded indicating drops in elevation from the headwaters of Basin A to its outlet. The elevation drops by ~461 m from the beginning of the headwaters zone, through the midstream zone, to the basin outlet in the downstream zone. The horizontal length of the selected channel (~72000 m) was found by counting the number of pixels (~880 m/pixel) within the confines of the channel from the start of the headwaters zones to the termination of the downstream zone at the basin outlet into Kraken Mare. Therefore, the selected pathway follows a channel-fitting ‘kinky’ route as the channel

travels from its starting point to its outlet. Once the slopes for each of the three zones were calculated, the mean slope for the entire channel segment was deduced.

After finding the basin-wide slope, a graph that displays the slope curve of the channel (figure 3.5) was constructed. By analyzing the slope curve of Basin A, it is apparent that this particular channel can be divided into three zones based on changes in slope: headwaters, midstream, and downstream (table 3.2). The headwaters zone is comprised of slope calculations 1 and 2, the midstream zone includes slope calculations 3 and 4, and the downstream zone includes slopes 5 through 9.

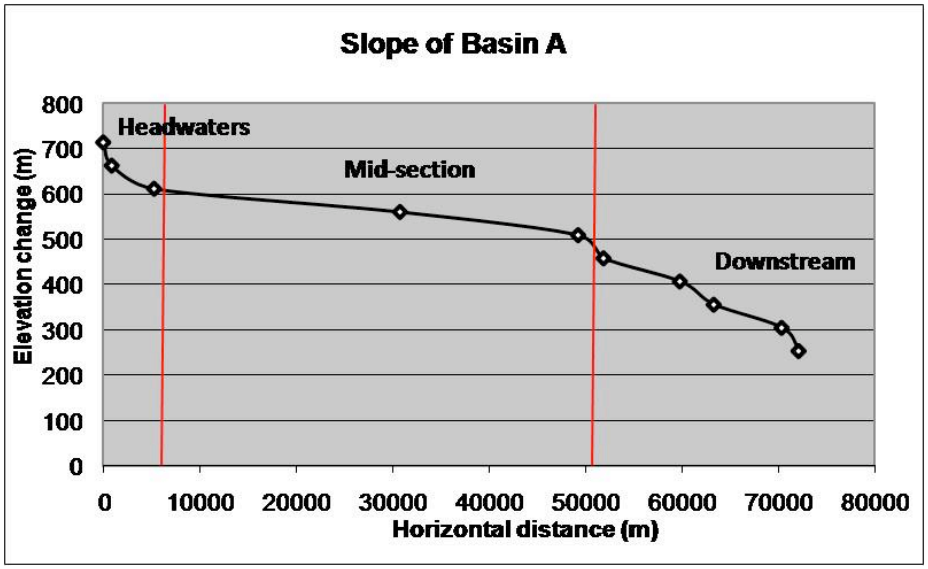

Figure 3.5: Graph of Basin A Slope. Slope of Basin A divided into the 3 zones: headwaters (points 1-3), midstream (points 4-5), and downstream (points 6-10). Red lines roughly indicate the boundaries between the three zones. Note the visible change in slope between each zone.

3.3.2: Sediment transport calculations

After Basin A was separated into three zones, each zone with its own slope value, I generated a variety of values aimed at understanding the sediment transport capacity within each zone using the following series of equations (see table 3.1 for important term values).

The Shields stress (τ^*) describes the capacity of a given flow to initiate sediment transport along the bed of a channel. Shields stress equals the boundary shear stress divided by the buoyancy of the sediment in the transporting fluid multiplied by the mean grain size of sediment within a given flow. This study modifies the normal definition of the D_{50} to represent the *midpoint* grain size instead of the *median* grain size. The image taken by the Huygens probe after it had landed (figure 3.4) shows a range of grain sizes from the imager resolution limit of 3 mm (adjusted to 1 mm in this study's calculations) up to 150 mm; however, the median grain size from this imaged sample of water-ice cobbles has not been constrained. As such, this study uses the midpoint value (D_{50} = 75 mm), which is halfway between 1 mm (D_{01}) and the top end of 150 mm (D_{100}) in place of the currently unknown median value for the imaged grains:

$\tau^* = \rho ghs/(\rho_s - \rho)gD_{50}$ [equation 3.1]

Where τ^* is the Shields stress, ρ is the density of liquid methane, $(\rho_s - \rho)$ is the difference between the density of water-ice sediment and liquid methane (i.e. buoyancy of the grains), g is the gravitational acceleration (in both the numerator and denominator), and the D_{50} is the midpoint grain size. The variable h (flow height) was initially held constant to one of four values (0.1 m, 0.5 m, 1.0 m, 1.5 m), and the variable s (slope) was defined by the slopes of each zone of Basin A. Four different values of τ^* were determined for each of the 3 zones – one for each of the flow heights (0.1 m, 0.5 m, 1.0 m, 1.5 m), creating a total of 12 τ^* values.

Next, the critical Shields stress (τ^*_c) for each of zonal slopes was calculated with a formula that uses slope to derive the critical Shield's stress in mountain streams on Earth. The equation (based on Mueller et al., 2005) was altered to account for the differences in sediment and fluid densities on Titan versus Earth. To do this, I divided the fluid density of water by the

buoyancy of quartz grains in liquid water [(1000 kg/m^3) / (1650 kg/m^3) = 0.6061], and then calculated the same ratio for the fluid density of liquid methane and sediment buoyancy of water-ice grains [(450 kg/m^3) / (542 kg/m^3) = 0.830]. Next, I divided the Titanian ratio (liquid methane and water-ice grains) by the Terrestrial ratio (liquid water and quartz grains) [(0.830/0.6061) = 1.369]. Once the ratio between Titan and Terrestrial sediment/fluid was calculated, the recalibrated τ^*_c equation is:

$\tau^*_c = [(2.18 \times s) + 0.021] \times 1.369)$ [equation 3.2]

where τ^*_c is the critical Shields stress and s is slope. Once the critical Shields stress values for each of the three zones were calculated, the ratio (τ^* / τ^*_c) was deduced for each zone. This ratio describes the amount of energy available to entrain sediment and the threshold energy required to initiate transport at a given location. Thus, (τ^* / τ^*_c) predicts whether enough energy is available at a given point to induce grain mobility. A (τ^* / τ^*_c) value below 1 indicates that there is very little (if any) sediment entrainment occurring, values of 1-2 indicate that size-selective mobility is possible, and values above 2 suggest that fully mobile conditions exist for all grain sizes (Clayton and Pitlick, 2007).

Once τ^*_c was defined, it was possible to solve for the critical flow depth (h_c), which defines the threshold at which sediment in a channel starts to move. Assuming all other terms stay the same, once the flow depth is increased above the h_c, then sediment will begin to mobilize, but if the flow depth drops below h_c, the sediment transport capacity goes back to zero. In order to find the critical flow depth, equation 3.1 is re-organized to solve for h, and τ^* is

replaced by the *critical* Shields stress value (τ^*_c) for the given location (defined using equation 3.2) in order to find the *critical* flow height:

$h_c = [\tau^*_c (\rho_s - \rho) D_{50}] / \rho s$ [equation 3.3]

By calculating the critical flow depths for each zone, it is possible to see how the depth requirement for the entrainment of water-ice sediment changes over the course of Basin A.

τ^* and τ^*_c values can then be utilized in a series of formulas that describe the bedload transport potential of a stream. The significance of bedload transport versus other forms of sediment transport is that the primary source of Titanian sediment considered in this study (water-ice) has fairly coarse grains (up to 150 mm) that would likely travel as bedload along the bottom of the channel during peak flows. Dimensionless bedload transport (defined in Meyer-Peter and Muller, 1948) measures the mobility of sediment along the bed of a stream:

$q^*_b = k(\tau^* - \tau^*_c)^{1.5}$ [equation 3.4]

Where q^*_b is the dimensionless bedload transport rate, k is a constant (most often 8), and ($\tau^* - \tau^*_c$) measures the amount of excess Shields stress available to entrain grains.

Now that the dimensionless bedload transport equation has been defined, it is possible to find the unit mass transport rate, which is a key component of the equation describing the denudation rate of a basin:

$qb = q^*_{b\,ds} \times [(s_g - 1) g D_{50}^3]^{0.5}$ [equation 3.5]

Where s_g represents the sediment specific gravity (ρ_s/ρ) defined as the ratio between the density of the sediment and the fluid (Clayton, 2005), qb is the unit mass transport rate, g is gravity, the D_{50} is the midpoint grain size, and $q^*_{b\,hw}$ is the dimensionless transport rate for the headwaters zone of Basin A.

Now that a unit mass transport rate has been calculated, it is possible to find the denudation rate of Basin A. The denudation rate measures the speed at which a given basin erodes down to its base level; therefore, a denudation rate can help constrain the age of the landscape by describing how quickly fluvial processes are able to resurface their surroundings. Basin A drops by ~461 m of elevation from the beginning of the headwaters zone to the terminus of the downstream zone at the basin's outlet, and so the denudation rate would constrain the minimum amount of time required for fluvial processes to erode away this elevated region of Basin A. In order to constrain the denudation rate of a basin, the unit mass transport rate was defined by multiplying the product of equation 3.5 by the width of the outlet of Basin A (~1400 m), then dividing by the area of Basin A (~1865 km^2):

Denudation rate = (0.023 m^3/s x 1400 m) / 1,865,000,000 m^2 [equation 3.6]

Thus, a denudation rate constraining the minimum amount of time for Basin A to erode down to base level is produced using equation 3.6 (assuming that external stimuli do not alter the rate of lowering).

3.4: Results

The calculated denudation rates (table 3.2) present the minimum amount of time required to erode the landscape of Basin A down to the base level of the outlet to Kraken Mare. The listed time spans are based on the slope of the downstream zone of Basin A (i.e. the zone where the outlet is located) using four constant flow depth values (0.1 m, 0.5 m, 1.0 m, 1.5 m). The critical flow depths required to entrain water-ice grains (ranging from 1 mm-150 mm) in the three different zones of Basin A are: headwaters (0.41 m), midstream (1.57 m), and downstream (0.51 m). The calculation of zonal slopes, τ^*, critical flow depths, τ^*_c, q^*_b, are summarized in table 3.3. The τ^*_c of each zone fluctuates depending on the slope of the zone (2nd and 3rd columns of table 3.3). Also, the q^*_b values do not increase in the downstream direction, which is different from the normal situation of basins on Earth. The reason for this is that there is very little excess Shields stress available in the midstream zone, which impedes the initiation of grain transport.

Table 3.2: Summary of Denudation Rates

h (m)	Time (Earth years)	Time (Titan Years)	Titan (summer only)
0.10	N/A	N/A	N/A
0.50	N/A	N/A	N/A
1.00	6569	223	891
1.50	2269	77	308

Summary of time requirements to erode down to base level in the downstream zone assuming constant flow at a variety of flow depths according to the denudation rates calculated using equation 3.6. The second column displays the time required to reach base level in Earth years (365 day years), the third column converts the values into Titan years (i.e. length of Saturn year, 10579 days), and the last column considers constant flow during the Titanian summer only (i.e one-fourth of the Titan Year), when seasonal heating leads to large convective storms and increased precipitation rates.

Table 3.3: Summary of Sediment Transport Analysis of Basin A

Region	Slope (s)	T^*_c	h (m)	T*	$(T^*-T^*_c)$	q^*_b	T^*/T^*_c	qb
Basin-wide	**0.006**	**0.047**	0.10	0.006	N/A	N/A	0.139	N/A
(mean)			0.50	0.032	N/A	N/A	0.693	N/A
			1.00	0.065	0.018	0.019	1.387	$5.076E^{-04}$
			1.50	0.097	0.050	0.090	2.080	$2.369E^{-03}$
h_c (m)			*0.70*					
Headwaters	**0.019**	**0.085**	0.10	0.020	N/A	N/A	0.240	N/A
(points 1-2)			0.50	0.102	0.017	0.018	1.199	$4.636E^{-04}$
			1.00	0.205	0.119	0.330	2.397	$8.645E^{-03}$
			1.50	0.307	0.222	0.836	3.596	$2.189E^{-02}$
h_c (m)			*0.41*					
Midstream	**0.002**	**0.035**	0.10	0.002	N/A	N/A	0.062	N/A
(points 3-4)			0.50	0.011	N/A	N/A	0.311	N/A
			1.00	0.022	N/A	N/A	0.621	N/A
			1.50	0.032	N/A	N/A	0.932	N/A
h_c (m)			*1.57*					
Downstream	**0.011**	**0.062**	0.10	0.012	N/A	N/A	0.193	N/A
(points 5-9)			0.50	0.059	N/A	N/A	0.963	N/A
			1.00	0.119	0.057	0.109	1.926	$2.853E^{-03}$
			1.50	0.178	0.116	0.317	2.889	$8.312E^{-03}$
h_c (m)			*0.51*					

Summary of pertinent terms and values for sediment transport through the three zones of Basin A. Note the change in slope (s), and the critical flow heights (h_c) required for each zone to initiate the bedload transport of 75 mm water-ice grains (the midpoint grain size).

3.5: Discussion

3.5.1: Topography data

The available topography map (PIA 10353, figure 3.1) is a small mosaic of overlapping flybys in the region (T25 and T28 being the primary flybys). The image represents a fantastic start to unraveling elevation variation in the region; however, it is not a perfect data source. The spatial structure of PIA 10353 is dependent upon the software that produced the image, and the local contents of the image. For example, patches of the image that are bland or featureless tend to have larger errors associated with them, and as such, areas lacking detail might be adulterated during the image processing stage (R. Kirk, USGS and Cassini Radar Team associate, personal

communication). Other types of artifacts work themselves into images produced by the same software as PIA 10353 as well. Furthermore, the borders of the polar seas are quite abrupt given the resolution of the image, and as a result elevation data close to the shorelines might be unreliable (R. Kirk, USGS and Cassini Radar Team associate, personal communication). While this study uses two elevation values close to the outlet of Basin A into Kraken Mare, these values are blended with other points further upstream into the downstream zone, which mitigates their error somewhat. Thus, the near-shore slope values might be less accurate than their upstream counterparts, but the trend in declining elevation values towards the outlet of Basin A (i.e. over the course of the downstream zone) is apparent. The inherent errors contained within PIA 10353 means that the slope values used in this study are likely inaccurate to some extent. Use of the original DTM that PIA 10353 is based on would help lower the amount of error in the slope calculations, but even the original DTM likely contains some amount of error on a pixel to pixel basis. A new and more precise topographical map of the polar seas is required to secure the most reliable slope values possible.

3.5.2: Slope of the downstream zone of Basin A

Normal basins experience a reduction in slope as their channels reach the outlet; however the calculated slope of Basin A (figure 3.5) suggests that the downstream zone has a steeper slope that the zone preceding it (the midstream zone). While the slope data presented in this study is based on a flawed topography map, the trend in decreasing slope towards the outlet of Basin A is provocative, and even if the calculated slopes are imprecise, the decreasing trend in the downstream slope is readily apparent. This increase in the downstream slope might indicate that the basin is in a state of rapid flux as it adjusts to a new base level. The driving mechanism leading to a new base level could stem from a fluctuating alkanifer beneath the polar seas. An

alkanifer (similar to the water table on Earth) may transport liquid hydrocarbons locally, from one mare to another, and perhaps from one region of Titan to another (i.e. pole to pole). Such subsurface transport of liquid hydrocarbons is only beginning to be examined, and future work concerning the channel networks draining into the polar maria must account for any discoveries concerning a global alkanifer.

3.5.3: Critical flow depths in Basin A

The midpoint grain diameter of water-ice sediment (D_{50} = 75mm), determined by the range of cobbles imaged at the Huygens landing site, requires a minimum depth of ~1.6 m to remain entrained along the entire course of Basin A (through all three zones). It is important to note that the Huygens landing site is located near the equator of Titan while Basin A is located near the north pole of the moon. However, the water-ice cobbles imaged by the Huygens probe are the only recorded examples of sediment on Titan; therefore, the imaged grains (figure 3.4) are the best available substitution for north polar water-ice grains.

The height of the critical flow depth required for sediment transport is inversely related to the slope and the amount of excess Shields stress available to entrain grains off the channel bed. Thus, as the slope increases from the midstream to the downstream zone of Basin A, the flow depth required to entrain the midpoint grain size decreases. Of course, the actual flow depth likely increases in the downstream direction due to the growing volume of liquid methane flowing from the headwaters across Basin A to the downstream outlet where flows are concentrated. Furthermore, the slope of the downstream zone looks like an ‘invigorated’ channel that formerly ended in a higher base level and now is incising to a lower elevation (probably due to a fluctuating methane table).

3.5.4: Calculation of τ^*_c

It is important to note that the τ^*_c values calculated in this study (table 3.3) were found using a formula that is dependent on the local slope (equation. 3.2). This formula [proposed by Mueller et al. (2005)] was generated from data gathered on the transport capacity of mountain streams. Given that the surface of Titan is more analogous to an arid landscape with gentle slopes on Earth, the Mueller formula for the deduction of the critical Shields stress might not be a perfect fit for the north polar region of Titan. However, the emerging picture of the terrain surrounding the large polar seas suggests that the region undergoes active cryotectonics as uplifted blocks of ice create radar bright plateaus covered by channels that are attempting to cut down to the base level of the region. As such, portions of the area might exhibit relatively steep slopes, which would help validate the use of the Mueller et al. equation (2005) in this study. The Mueller τ^*_c formula was modified slightly to the conditions prevalent on Titan (i.e. sediment and fluid density differences). See methods section for an explanation of how the equation was adapted to this study.

3.5.5: Bedload transport curves

The analysis of bed load transport conducted in this study borrows much from Burr et al., (2006), who examined the transport potential of sediment on Titan. My analysis shared various values with Burr et al. (2006) including identical density values for water-ice sediment (992 kg/m^3) and the fluid density (450 kg/m^3), and the same gravitational acceleration (1.35 m/s^2). The grain size ranges considered in Burr et al. (2006) are from 10-100 cm while this study used values ranging from 1 mm – 150 mm. A key graph (adapted from Burr et al., 2006, and shown in figure 3.6) provides slope-derived transport curves for a range of grain sizes and flow depths. As

slopes become steeper, the ability of a stream to entrain sediment increases, lowering the minimum flow depths required to entrain a grain of a given size.

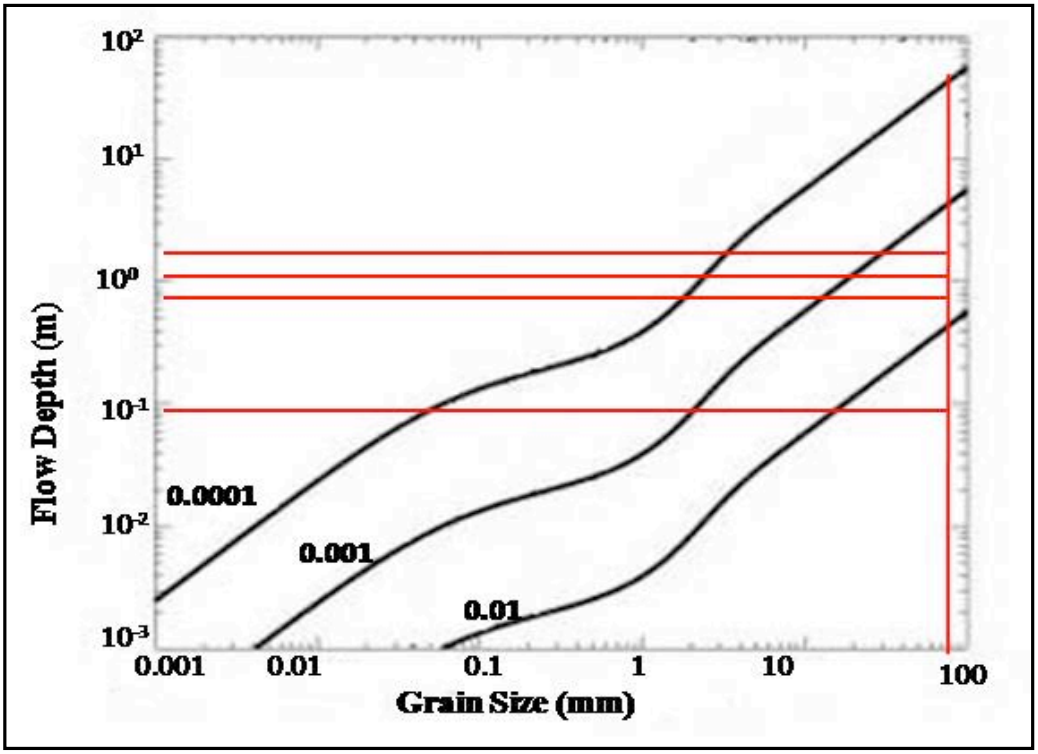

Figure 3.6: Graph of Basin A Slope. Compares three different slopes, and the flow depths each requires to entrain water-ice grains with a range of diameters. The horizontal red lines intersecting the slope curves mark the fixed flow heights analyzed in this study (0.1 m, 0.5 m, 1.0 m, and 1.5 m). The one vertical red line roughly indicates where the 75 mm grain size is in relation to the slope curves. Downstream and headwater zones' slopes fit to the right of the 0.01 slope (i.e. steeper), and the midstream slope fits between the 0.001 and the 0.01 slope curves. Adapted from Burr et al. (2006).

Figure 3.6 displays bedload entrainment initiation curves for three different slopes: 0.0001, 0.001, and 0.01. The graph illustrates that for a 75 mm diameter grain size, a slope of 0.01 would require a flow depth of ~0.25 m to become entrained. None of basin A's zones are able to entrain 75 mm sediment at such low critical flow depths. The headwaters zone (slope ~0.019) requires a minimum depth of 0.41 m, the midstream (slope ~0.002) needs 1.57 m of flow, and the downstream zone (slope ~0.011) requires 0.51 m of flow to entrain 75 mm

sediment. Thus, the bed load transport parameters utilized in this study suggests that higher flow heights are required to entrain water-ice grains of a given size compared to the analysis of Burr et al. (2006). While the differences between this study's results and Burr et al. (2006) are not immediately apparent, it is possible that the calculation of the critical Shields stress using equation 3.2 (adapted from Mueller et al., 2005) has led to more conservative results than those in Burr et al. (2006).

3.5.6: Denudation rates

The listed denudation rates in table 3.2 detail the rate at which the downstream zone erodes down towards base level. The calculated denudation rates are tantalizing pieces of information that can 'age' the surrounding landscape by producing the minimum amount of time necessary for Basin A to erode down to the mare level at its outlet. In other words, the denudation rate constrains the minimum amount of time required for fluvial processes to resurface their surroundings. Given the evidence for large convective storms during the summer (e.g. Brown et al., 2002) resurfacing via precipitation and channelized flow is likely an important process on the surface of Titan, and the denudation rate can help define the parameters of channelized liquid methane erosion. The included denudation rates in this study are linear; however, the actual denudation rate of Basin A is most likely going to adjust as the slope changes in response to the lowering landscape. Therefore, the erosion of Basin A down to the mare-level at the basin's outlet should lessen as the slope is reduced by the denudation process. Future work should incorporate the changing slope into the calculation of the denudation rate.

3.5.7: Sediment sources

The range of grain sizes used in this study (1 mm – 150 mm) leads to a D_{50} of 75 mm (representing the midpoint grain size). The range of grain sizes in this study was derived from

images displaying water-ice cobbles at the Huygens landing site. The Huygens landing site is closer to the equator than the north pole of Titan; therefore, whether the range of cobble sizes imaged by the Huygens probe is indicative of polar water-ice grains is currently impossible to answer given the current available imagery. Given the lower requirements to entrain sediment on Titan versus Earth (Collins, 2005), and the well-rounded appearance of the Huygens landing site cobbles, it seems likely that water-ice grains of 75mm and larger become entrained in liquid methane flows.

This study only considers the potential for water-ice sediment to become entrained in liquid methane flows, and does not investigate the potential sediment transport parameters of organic particles in part because of the large range in particle densities recorded in the literature (organic particulate densities of ~400 – 1500 kg/m^3). An undetermined depth of precipitated organics (e.g. Mousis and Schmitt, 2008) covers the surface of Titan, which likely provides a much finer sediment source than water-ice grains. Furthermore, the presence of fine grained organics over portions of the water-ice bedrock of Titan could increase the denudation rates presented in this study (i.e. decrease the amount of time required to cut down to base level) by providing a layer of easily removable material over the confines of Basin A.

Also, this study only considers the fluid density of liquid methane. In reality, runoff from precipitation on Titan probably contains other hydrocarbons and perhaps some nitriles, which of course would change the fluid density considered in this study. Thus, this chapter used the best available data to deduce the midpoint grain size of water-ice sediment transported as bedload in pure liquid methane flows. The role of precipitated organic particles and the impact of hydrocarbon impurities in the liquid methane flows are not considered here, but would likely

increase the potential for flows to entrain coarser water-ice grains. For a more detailed consideration of these factors, see Burr et al. (2006) and Collins (2005).

3.6: Conclusions

Given the available topography data, the range of grain sizes considered, and the expectation that analogous flows on Titan would entrain larger grains compared to Earth (Collins, 2005), it seems likely that a minimum depth of ~1.6 m would entrain 75 mm grains in all three zones of Basin A. The significant shifts in slope (0.019 to 0.002 to 0.011) between the zones of Basin A lead to a wide range of required flow depths for the entrainment of 75 mm water-ice grains. Given the large range of flow depths, it is possible that only large storm events generate enough precipitation to mobilize 75 mm grains in all parts of Basin A. While relatively shallow flows can entrain 75 mm grains in the headwaters (0.40 m) and downstream zones (0.51 m), the midstream of Basin A requires 1.57 m flow to entrain 75 mm grains. Thus, smaller precipitation events might only be able to entrain the midpoint grain size in isolated portions of Basin A. A fully mobile bed on Earth requires a τ^* values about two times as large as the τ^*_c (i.e. 0.06 / 0.03). Even the deepest flow depth used in this study (1.5 m) cannot generate a sufficient amount of excess Shields stress to initiate bed load transport of 75 mm water-ice. In contrast, the headwaters and downstream zones would exhibit fully mobile beds at ~1.0 m and 1.5 m flow depths. Thus, the results suggest that slope is a crucial factor in the determination of entrainment initiation, with steeper slopes transporting larger grains in shallower flows versus regions with more gentle slopes.

While this study presents some tantalizing data regarding bedload entrainment of water-ice grains on Titan, the topography data used in this study (from PIA 10353) includes some

amount error and is not accurate on a pixel-to-pixel basis, but should produce acceptable slope values for distances >5 km (R. Kirk, USGS and Cassini Radar Team associate, personal communication), which is shorter than the minimum length considered in this study (5280 m for the headwaters section). Subsequent digital terrain models will provide more accurate topography data where overlapping flybys allow for stereo analysis, and future sediment transport studies need to incorporate this emerging data.

The denudation rates calculated in this study suggest that Basin A will erode down to base level in ~2200 or more Earth years. The significance of calculating a denudation rate for Basin A is that it could become a useful tool for aging the polar surface, which to date has proven difficult to constrain using craters (see Lorenz 2007b for cratering rates on Titan). As such, accurate denudation rates for basins around the north polar seas could help constrain the speed at which fluvial processes operate in the region and resurface their surroundings.

CHAPTER 4.

CHANNEL NETWORKS ON EARTH AND TITAN: A COMPARISON OF MORPHOLOGIES, BIFURCATION RATIOS, AND STREAM ORDERING

4.1: Introduction

Once Cassini's Radar Data began imaging the surface of Titan, the presence of erosional features like channels supported the pre-existing evidence of methane precipitation onto the surface. Due to its large distance from the Sun, Titan only receives 1/100th of the solar energy that the Earth absorbs. Consequently, the mean surface temperature on Titan is only ~94K (Lebreton et al., 2005, Porco et al., 2005). At these low temperatures, methane is close to its triple point (~90K), which in conjunction with its abundance in the atmosphere, makes methane a prime candidate to fuel a 'methanological' cycle (Lunine and Atreya, 2008). Such a cycle would lead methane precipitation to cut erosional features like channels into the water-ice bedrock of Titan's crust. Given the evidence gathered by the radar instruments of Cassini (e.g. Lorenz et al., 2008), and the ideal surface conditions for the presence of liquid methane, it is likely that precipitated liquid hydrocarbons cut channels across the surface of Titan.

Some of the channels observed by Cassini's Titan Radar Mapper appear to form complicated networks like drainage basins cut by water on Earth. A Terrestrial drainage basin is characterized by a network of stream channels that drain water from areas of higher elevation down towards the low-lying outlet of a basin (Ritter et al., 2002). One way to quantify the relationships between channels within a given basin is to organize the channel segments into a hierarchy of stream orders that describes how smaller channels feed into larger channels (for example, 2 'n' channels join to form an 'n+1' channel). The ratios between different stream orders (n, n+1, n+2, n+3, etc) are used to constrain the properties of a given basin through the

calculation of a mean bifurcation ratio (Ritter et al., 2002). The bifurcation ratio describes the relationship between the channel segments in a stream order with the next highest stream order. The basin-wide bifurcation ratio can be used in conjunction with other factors to describe a wide range of mathematically-based properties displayed by a given channel network. Thus, stream ordering of drainage basins on Earth has led to the calculation of bifurcation ratios, which can be used to describe the relationship between one stream order and the next highest order.

Titan presents a prime opportunity to apply the principals of stream ordering to the surface of another world, where liquid methane, not water, carves the channel networks. As such, this study investigates three apparent drainage basins around Titan's north pole by constructing channel networks, conducting stream ordering, and calculating bifurcation ratios at all three locations. The morphology of the basins, coupled with bifurcation ratios, can help constrain the formation history of the basins while hinting at the cryotectonic forces that might have shaped portions of each basin discussed in this chapter (but specifically Basin B). Therefore, an investigation of the morphologies of these three apparent basins could shed some light on the lithology of the region, and the internal processes that shape the north polar landscape of Titan.

The three basins are also compared to an analogous Terrestrial basin in order to help constrain the morphological similarities shared by channel networks on Titan and Earth. Terrestrial basins with similar morphologies to basins on Titan might be able to shed light on the formation histories of the Titanian basins. For example, linear channels on Earth are usually indicative of channel networks shaped by local tectonic activity. Therefore, it is possible that Terrestrial basins with analogous morphologies to the Titan basins might hint at the formation processes which formed them.

4.2: Background

4.2.1: Radar properties of north polar fluvial features

The north polar, Titanian channel networks analyzed in this study cut paths through the plains and highlands that surround low-lying, radar dark areas called mares. The radar dark spots (interpreted as hydrocarbon seas/lakes) have extremely low backscatter values that fall below the instrument floor of -25dB (e.g. Brown et al., 2008). The combination of the SAR incidence angles (15-35^{o}) and the low backscatter off the radar dark patches is consistent with a very smooth surface (rock, ice, liquid, organics), or perhaps a non-reflecting surface such as soot or dirty snow overlying a uniform and electrically absorbing substrate (Stofan et al., 2007). Observations of the radar swaths containing the dark spots; however, show that the borders of the dark spots look like coastlines, and dark channels flowing from the surrounding highlands connect to them (this study). Given the expectation that a hydrocarbon cycle exists on Titan (e.g. Atreya et al., 2006), and the morphological similarities of the radar dark spots to lakes, it is likely that these radar anomalies are lakes filled with liquid hydrocarbons like methane and/or ethane and not large accumulations of 'dirty' snow or soot.

Complimenting the evidence of fluvial features imaged using SAR is the radiometry mode of the Titan Radar Mapper that can record brightness temperature values along with the SAR swaths. The spatial resolution of the radiometric-SAR mixed recording is more coarse (>6km) than SAR imaging alone; however, several of the dark patches can still be resolved (Paganelli et al., 2007). Thus, microwave backscatter and emissivity measurements suggest that the radar dark patches are smooth surfaces of a low dielectric material like liquid methane or ethane.

Figure 4.1: **Radar Swaths (early 2008). (a)** Left side of image displays the radar swaths recorded over Titan's northern hemisphere; **(b)** right side of image displays swaths over the southern hemisphere. The equator is the outer circle in both images and the poles are located at the image centers. The finest resolution recorded corresponds with the thinnest portions of the swaths, and the coarsest resolution is found at the wider portions of the swaths. Source: NASA, Steve Albers from NOAA/GSD.

4.2.2: Terrestrial basin imagery

Numerous Earth-bound basins with similar morphologies to the Titanian basins were considered for examination. The Oman Basin, an ephemeral network along the coast of central Oman, was eventually picked as an analog basin using Google Earth imagery. Another Terrestrial analog used in this study, referred to as the Nevada Basin, was found using Google Earth. Both basins are in arid environments with sparse vegetation, making them ideal for comparison with the barren surface of Titan. One drawback with Google Earth is that it uses a combination of different satellites to produce a mosaic of various spatial resolutions. However, a deciding factor in the selection of the Oman and Nevada basins was that the Google Earth imagery used in this study displays the same resolution over the extent of each basin. Discussion

of the basins' morphology, and their connection to the Titanian basins, is included in subsequent sections.

4.3: Morphology and Location of Basins

4.3.1: Titanian basins

The three liquid-methane carved basins considered in this study are located in a region of Titan dominated by liquid hydrocarbon reservoirs (Stofan et al., 2007). This region, found between 220°W and 350°W longitude and above 55°N latitude, displays a varied topography with low-lying mares surrounded by highlands. The image from which the Titanian drainage basins were identified is set in a polar stereographic projection (128 pixels/degree and 351.11 m/pixel) that covers an area from 56°N up to the north pole (R. Kirk, USGS and Cassini Radar Team Associate, personal communication). The image (figure 4.2) is a mosaic of various Cassini flybys including T16, T18, T19, T25, T28, T29, and T30 (R. Kirk, USGS and Cassini Radar Team Associate, personal communication). The three basins analyzed in this study were chosen based on their apparent morphologies, ranging from dendritic to contorted, which are common drainage basin types on Earth, and as such, the selected Titanian basins lend themselves well to comparisons with Terrestrial basins. Other Titanian networks with similar morphologies were considered, but were ultimately eliminated due to an inadequate numbers of discernable channels.

4.3.2: Basin A

This basin (located along the 270°W meridian in figure 2, close up in figure 10a) drains from the surrounding highlands into an apparent 'drowned valley' branch of a polar sea, which might have been flooded by a fluctuating methane table underneath the mare (Mitchell et al., 2009). Basin A (figure 4.3, figure. 4.10a) displays a dendritic morphology with stream segments

branching out in asymmetrical positions from one another. Basin A, measured from the furthest headwater to the outlet, is ~150 km long. Highlands define the southern and western perimeter of Basin A, and a gentle slope is expected to lead the channels into the estuary-like branch of a polar mare. Furthermore, analysis of the preliminary topography data suggests that the basin's slope increases just before it drains into the mare (see chapter 3). It is possible that this sudden and somewhat late drop in elevation is due to a fluctuating methanological table that acts as an important control on the lake levels in the region.

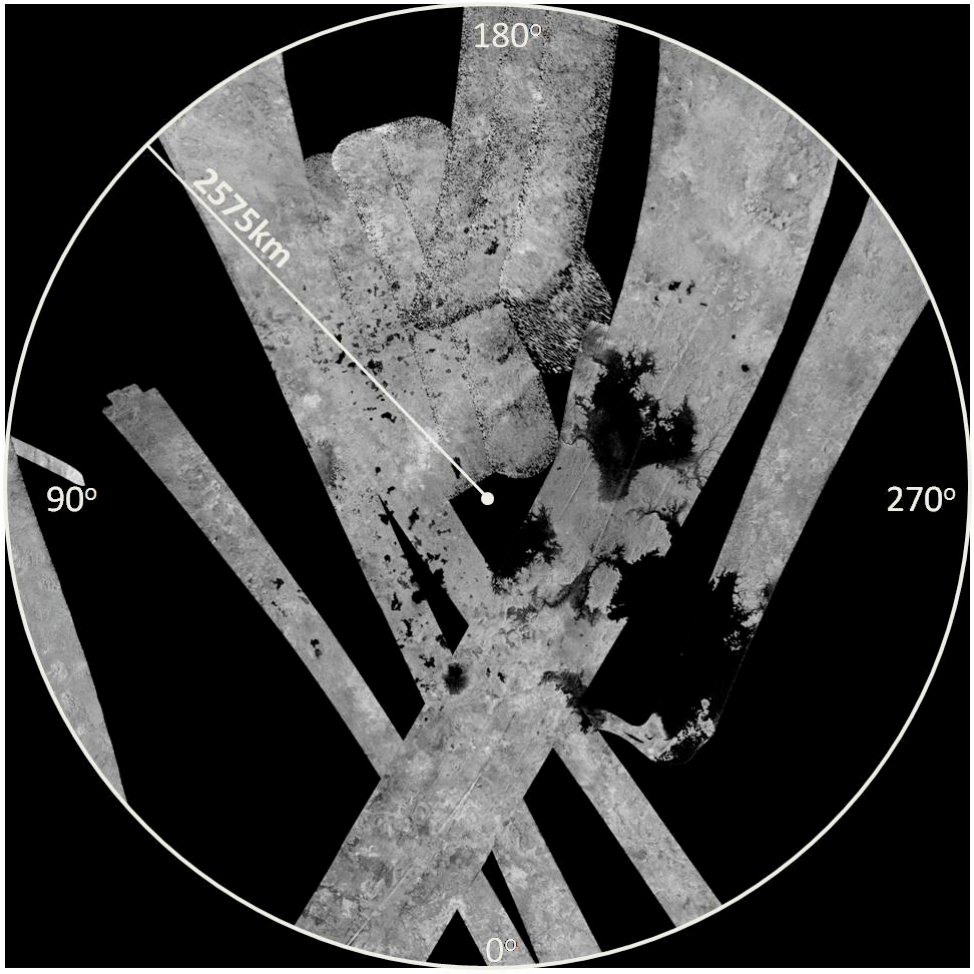

Figure 4.2: North Polar Region of Titan. Mosaic of the available polar radar swaths where the north pole is at the center of the figure (90°N latitude), and the outer white circle represents 56°N latitude. The radius of the circle is 2575 km, which is also the length of each line of longitude. Modified from MIBPH90N000_T039S00.

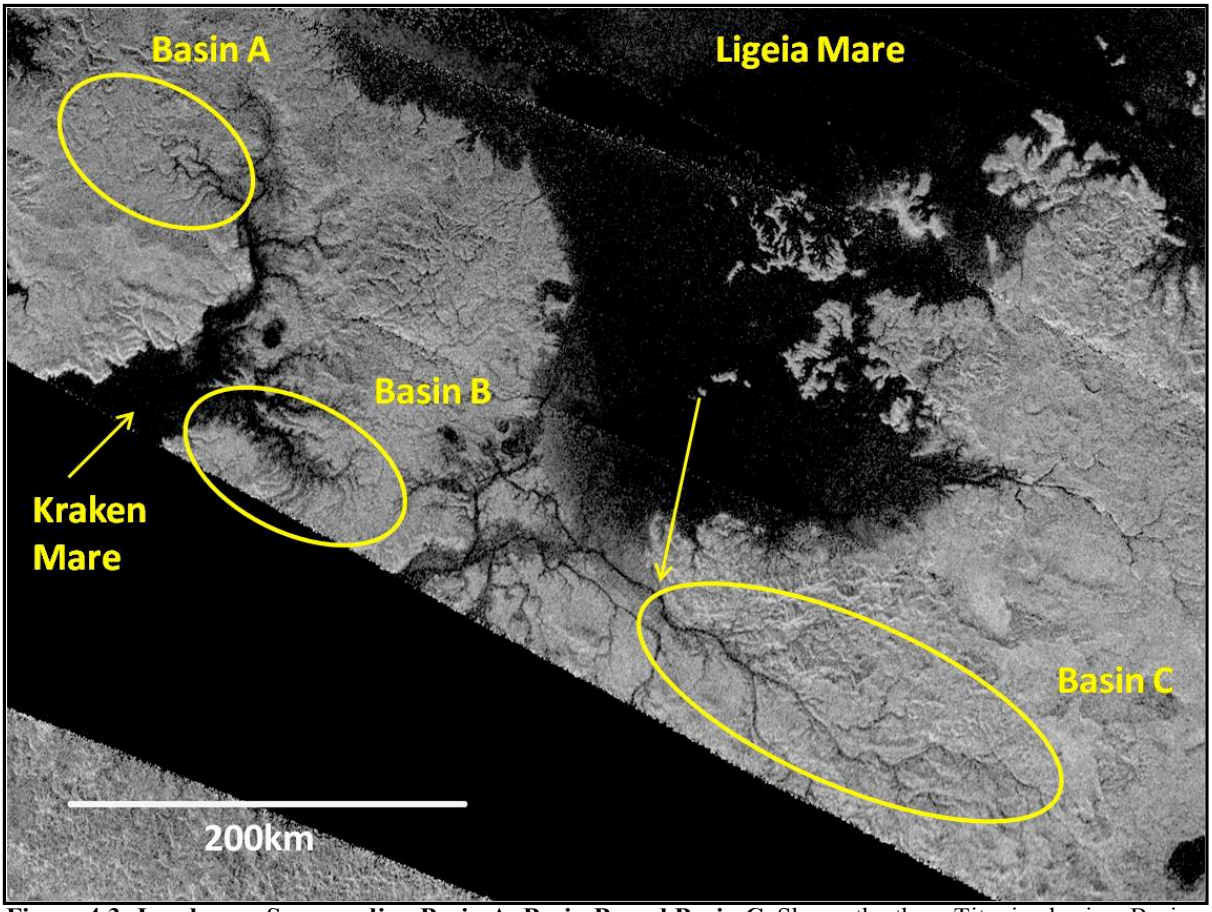

Figure 4.3: Landscape Surrounding Basin A, Basin B, and Basin C. Shows the three Titanian basins. Basins A and B empty into the 'estuary' that continues beyond the extent of the swath. Basin C flows from east to west along a fairly constant line of latitude before veering towards Ligeia Mare to its north (indicated by yellow arrow). Nothing to the west of the yellow arrow was considered to be part of Basin C due to the chaotic nature of the channels beyond the extent of the arrow.

4.3.3: Basin B

Basin B (~125 km in length) empties into the same polar 'estuary' as Basin A, but has a noticeably different morphology from Basin A. Basin B (figure 4.3, figure 4.11a) has a contorted/linear morphology with numerous branches of tributaries that drain into the polar mare without first draining into a larger order, central channel trunk. Topographical data generation for the basin is still an ongoing process for the Cassini Radar Team, but current data of the region (PIA 10353, discussed in chapter 3) confirms that the channels flow from highlands down into the mare branch. Basin B's morphology is strikingly similar to channel networks nestled in

between extensional ridges on Earth (in central Nevada and the East Africa Rift Valley, and elsewhere). Thus, perhaps Basin B was formed by cryotectonic processes similar to those that generate continental spreading zones on Earth.

4.3.4: Basin C

Basin C (figure 4.3, 4.12a) displays a constrained dendritic morphology with the channel branches gravitating towards a parallel orientation to the main trunk, versus a dendritic network like basin A where the branching channels are closer to perpendicular with the central trunk. Basin C appears to have constrained branches flowing into its central trunk perhaps because local topographical variations (i.e. uplifted highlands) appear to have prevented the channels from spreading out. The Basin's main downstream channel (after it veers towards the hydrocarbon sea to its north) is difficult to decipher. The downstream channel appears to continue in a straight line towards the west, but it also appears to veer towards the north to join the mare. Because of difficulties deciphering the direction of flow of the downstream portion of Basin C (indicated by a red arrow in figure 3), it is not considered in this study. As such, the size of the basin fluctuates from ~300 km to ~500 km in length depending on the location of the outlet.

4.3.5: Terrestrial basins

Given the dearth of vegetation and infrequent rainfall, arid basins on Earth share many analogous traits with Titanian channel networks (Lorenz et al., 2007a). The significance of Terrestrial analogs is that they present an opportunity to investigate the possible tectonic regimes of the north polar basins (by comparison with earthbound landscapes with known tectonic histories). Furthermore, it is possible to constrain the channel construction process I conducted in this study by simply increasing the resolution of the image. The available radar data of Titan, however, cannot be resolved further; as such, Terrestrial channel networks contain more detail

than Titanian channel networks because the enhanced resolution of earthbound basins in Google Earth allows for the creation of more detailed channel networks. Therefore, by using the same channel construction process to map both Titanian and Terrestrial basins, it is possible to deduce how many channels may actually be in the smaller, difficult to detect orders that likely house a substantial amount of channels that cannot be resolved in the SAR imagery of Titan.

A variety of arid landscapes are available to compare with Titan, including the desert hills of eastern Egypt, the Canyon Lands of Southern Utah, and other places with readily identifiable channel networks with similar, dendritic morphologies. The available topography data from Titan (see chapter 3) suggests that the channels might carve shallow canyons into the surrounding landscape. Such canyons could be aided by headward erosion (i.e. erosion of the channel that starts at the outlet and moves upstream) caused by intense summer storms (Hueso and Sanchez-Lavega, 2006). Many arid basins on Earth cut deep channels and canyons as they navigate through features like uplifted plateaus. Such canyon-cutting channel networks could serve as excellent analogies for the Titanian basins that carve the barren, water-ice dominated surface of Titan.

4.3.6: Oman Basin

This basin is found just east of Sharbthat, a small coastal village along the central region of Oman (figure 4.4). The outlet of the basin is located at 17°55’58”N and 56°16’41”E, and the furthest headwater is located at 17°58’46”N and 56° 22’25”E. The basin is ~14.40 km long. I have been unable to find the name of the basin, or any of the stream channels in the vicinity of Sharbthat; as such, the basin is simply referred to as the ‘Oman Basin’ throughout this study. The Oman Basin (figure 4.13) has cut canyons into a small uplifted plateau, which might mirror the channels of the Titanian basins as they navigate through water-ice terrain of varying elevation.

The basin has a dendritic morphology with what may be canyon-constrained channels stemming from the elevated plateau that the stream network has cut through and the subsequent canyons created by the cutting force of precipitation in the area. One reason why this particular basin was chosen over other possibilities was because of its strikingly similar appearance to the barren landscape and dendritic channel networks of Titan, in particular Basin A and Basin C. Basin B, however, does not fit into the dendritic mold, and is ill-suited for comparison with the Oman Basin. The Nevada Basin (discussed in the following subsection) is a closer analog to Basin B.

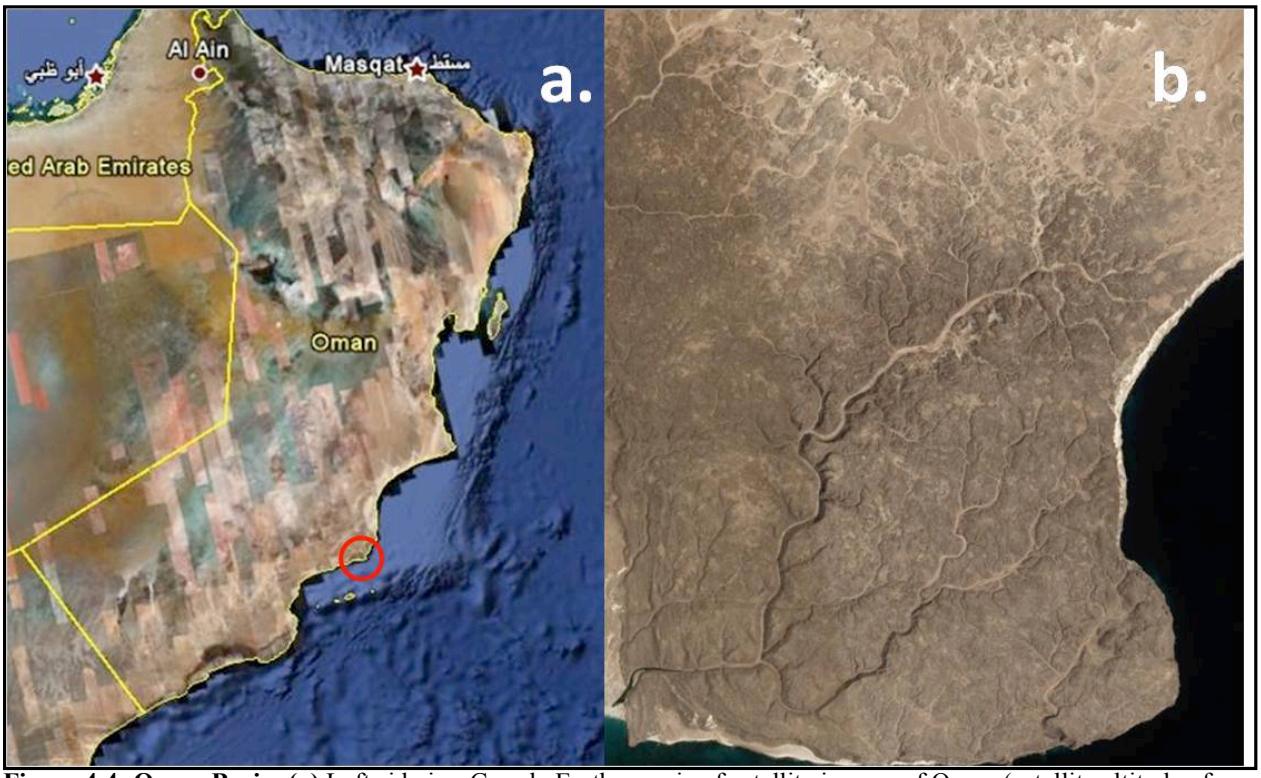

Figure 4.4: Oman Basin. (a) Left side is a Google Earth mosaic of satellite images of Oman (satellite altitude of ~1550 km). The Oman Basin is located within the red circle. **(b)** Right side of image shows the Oman Basin up close (satellite altitude of ~9 km). Its outlet is in the lower left-hand corner, and its headwaters are in the upper right hand region. Note the dark brown plateau that the basin cuts through before entering the Arabian Sea. Image recorded on April 16th, 2009.

The approximate length of the Oman Basin (~14.40 km) is much smaller than the Titanian basins, which range from ~150 km (Basin A) to over ~500 km (Basin C) in length. The

disparity in scale between the Titanian basins and the Oman Basin, however, should not impair the comparison of the basins' apparent morphologies. The morphology displayed by a drainage basin is assumed to be the same at every scale (Ritter et al., 2002), meaning that the individual sub-basins of each tributary share the same basic morphology as the entire river system. Thus, two dendritic basins of dissimilar sizes can possess similar bifurcation ratios because the relationship between stream orders holds constant throughout the network – from the headwaters of a small sub-basin, to the main trunk of a massive river.

4.3.7: Nevada Basin

The Nevada Basin (~51km long) is located within the alternating basin-range landscape of central Nevada (figure 4.5), which is an arid environment with sparse vegetation. The outlet of the basin is located at 37°50'59"N and 114°20'21"W (where it joins another channel network), and its furthest headwater is around 38°13'53"N and 44°32'40"W. I have been unable to find an official name for this basin; as such, I simply refer to it as the Nevada Basin in this study. The basin has a linear central channel with numerous smaller channels flowing into it at roughly perpendicular angles.

It is important to note that the morphology of the Nevada Basin's central trunk likely stems from the tectonic regime of the region. Extensional ridges adjacent to the basin (and throughout the region) are pushed up by tectonic forces underneath the surface. Moreover, the low-lying areas between the extensional ridges (i.e. where the Nevada Basin is located) undergo crustal thinning as the North American plate is stretched while it moves over the Pacific plate to the west. Crustal thinning leads to linear fractures and faults in the low-lying basins, which helps to explain the appearance of the Nevada Basin's central trunk. The Nevada Basin is similar to Basin B, which is dominated by a central 'drowned' trunk with many perpendicular channels

flowing into it. Given the comparable morphologies of Basin B and the Nevada Basin, it is possible that similar tectonic forces on Titan give Basin B its unusual appearance. Further discussion of Basin B's potential tectonic regime, and its similarity to the Nevada Basin, is included in later sections.

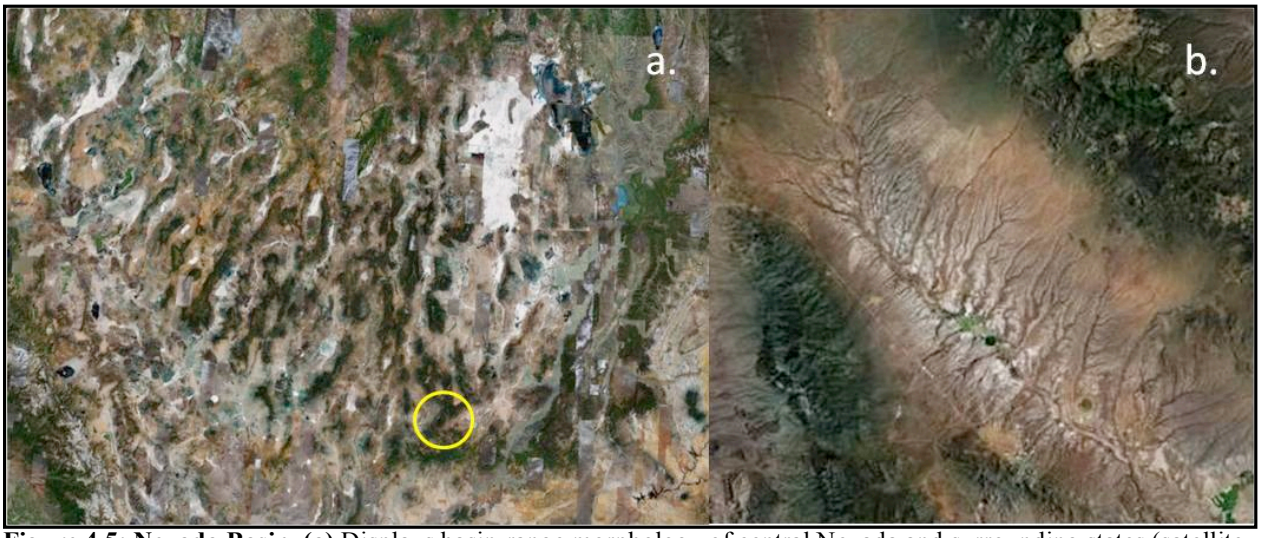

Figure 4.5: Nevada Basin. (a) Displays basin-range morphology of central Nevada and surrounding states (satellite altitude of ~1350 km). Nevada Basin is contained within the yellow circle. **(b)** Nevada Basin up close (satellite altitude of ~1700 m). Note the linear central trunk (tectonic fracture) with numerous perpendicular smaller channels draining into it.

4.4: Methods

4.4.1: Channel network verification process

After the sites were chosen, the Titan channel networks were traced on top of SAR mosaic (MIBPH90N000_T039S00). Constructing a stream network clutters the image and makes it progressively more difficult to identify additional channels, determine where channel segments join, and draw segments to represent accurate lengths (where possible). To combat these tracing issues, additional, 'clean' versions of the same image were cross-referenced with the image housing the channel construction process (figure 4.6 - 4.9). The clear, verification images were

often set to a smaller scale (~2 to 3 times as small) because the channels can be difficult to discern at the close up view required to carry out the stream network construction process. Also, older versions of the corresponding channel network were compared to channel networks still in process. Previous versions of the constructed channel networks were created with coarser resolution imagery (NASA image: PIA10353), or stretched versions of an analogous mosaic (BIBQI52N010_D126_T028S01). All of the Titanian channel networks analyzed in this study were built on image mosaic (MIBPH90N000_T039S00).

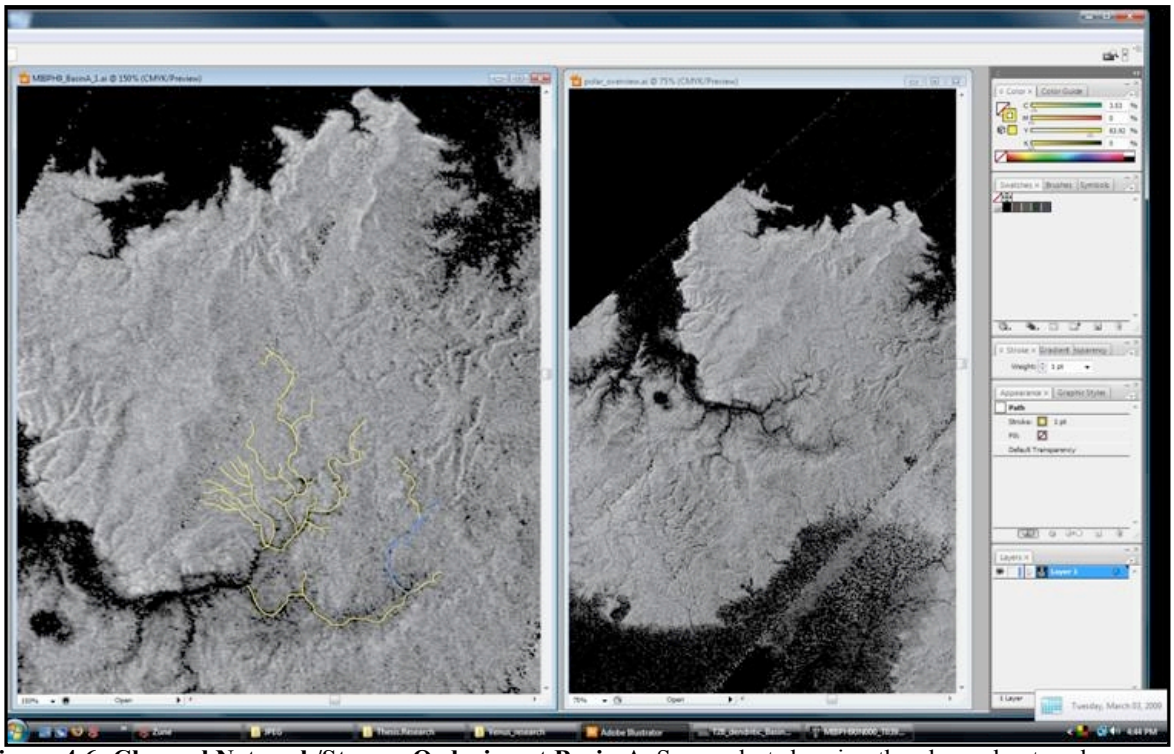

Figure 4.6: Channel Network/Stream Ordering at Basin A. Screenshot showing the channel network construction process at Basin A (left window), and verification of the network using a clean version of the image at a smaller scale (right window).

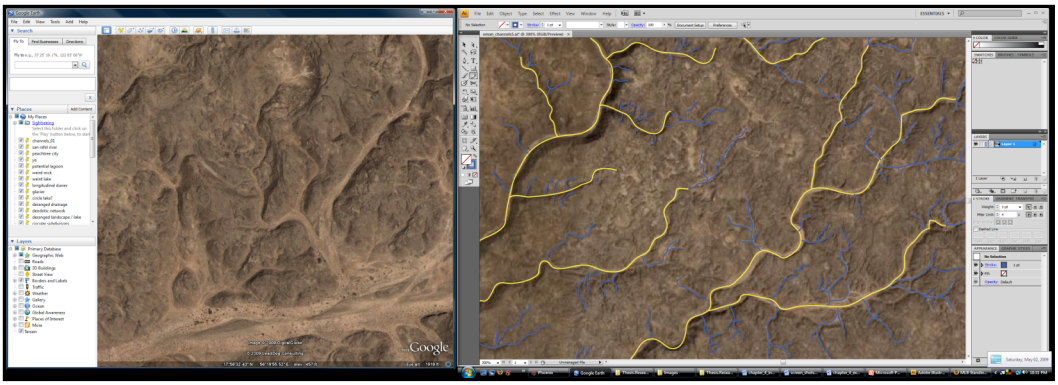

Figure 4.7: **Channel Network/Stream Ordering at Oman Basin.** Screen shot of the Oman Basin network construction (right window) with the same basin at a larger scale in Google Earth (left window). Note the enhanced number of mapped channels (compared to figures. 4.6, 4.8, and 4.9) resulting from the higher resolution provided by Google Earth (satellite altitude ~460 m).

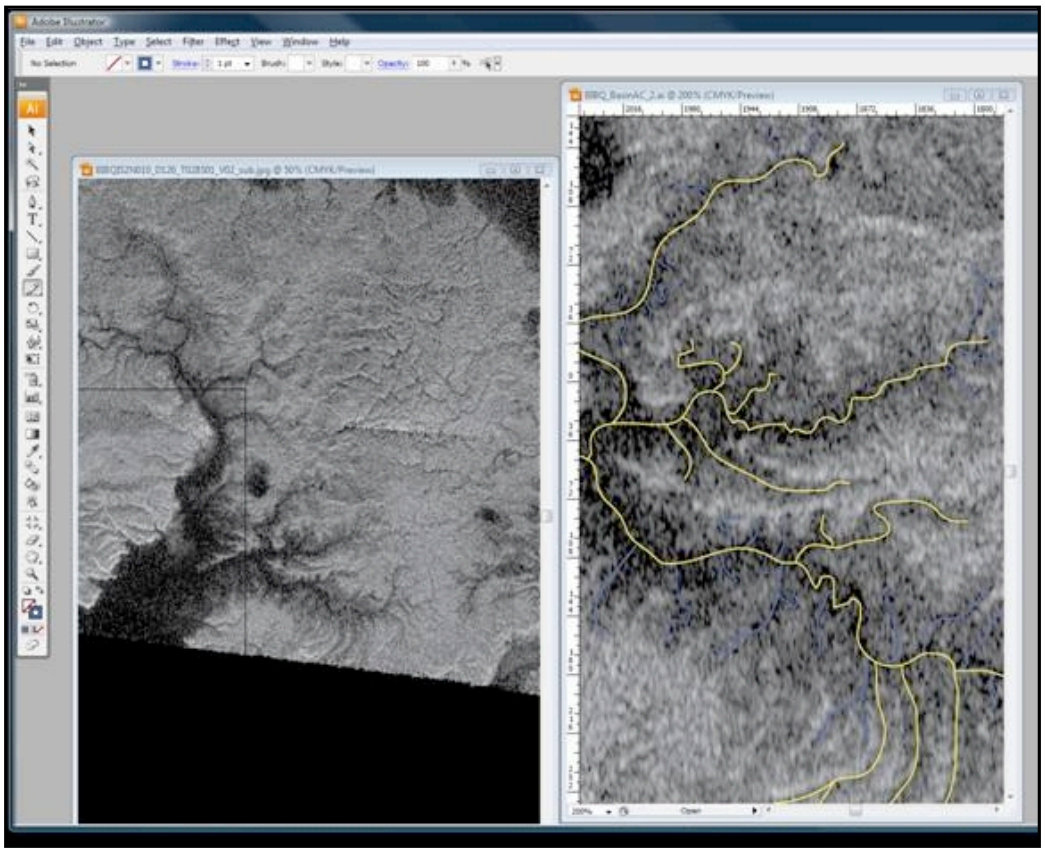

Figure 4.8: Channel Network/Stream Ordering at Basin B. Screenshot displaying a clean version of Basin B (left window) with channel network progression at Basin B (right window). Note the difference in scales between the two sides.

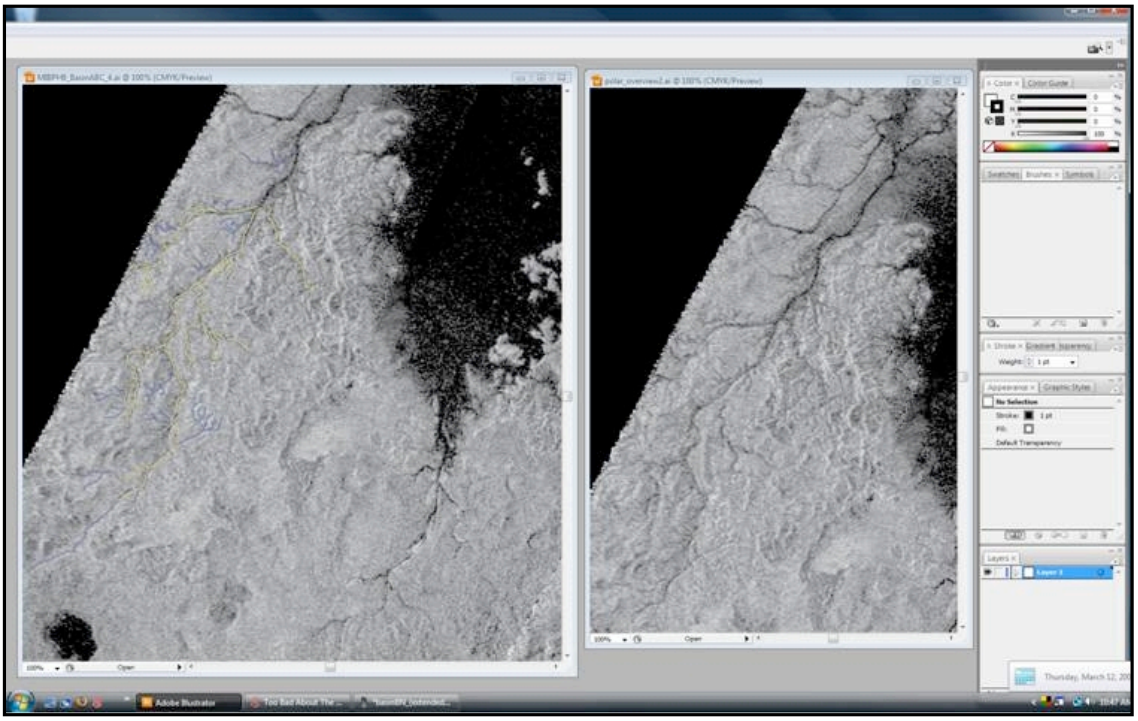

Figure 4.9: Channel Network/Stream Ordering at Basin C. Screenshot showing the channel network at Basin C (left window), with the clear version of the same image (right).

4.4.2: Channel network construction

The networks traced at each of the sites are separated into yellow and dark blue channels (figure 4.10-14b). This separation of channel segments distinguishes between channels that are visibly obvious in the imagery (yellow), and other channels that are more speculative (dark blue). The dark blue channels display evidence indicating that they are legitimate features in the imagery; however, they are flawed in one or more of the following ways: (1) dark blue channels are too faint to trace for their entire length, (2) the confluence of dark blue channels with the larger yellow channels is difficult to ascertain, (3) dark blue channels are too small to confirm direction of flow, (4) dark blue channels are intersected by other random lines in the imagery that might be noise or other legitimate channels that are difficult to fit into the channel networks.

The vast majority of the dark blue channels are smaller (and of a lower order) than the yellow channels. This disparity intuitively makes sense – the more visible channels are larger and easier to discern. Most of the [n+2] order streams are yellow, and all of the [n+3] and [n+4] channels are yellow channels; in contrast, many of the [n] and [n+1] stream segments are dark blue.

4.4.3: Stream ordering

I applied a stream ordering technique developed by Strahler (1952) to constructed channel networks in the north polar region of Titan dominated by polar seas, and to a Terrestrial analog basin. Strahler's stream ordering method, adapted from Horton (1945), labels all headwaters within a given drainage basin as 'first-order' stream segments (Ritter et al., 2002). Where two first-order segments meet, a second-order stream is labeled, and where two second-order stream segments meet, a third-order stream is recognized. This process of increasing a stream order whenever two stream segments of the same order meet continues until a stream network reaches its maximum ordering (i.e. the stream network exits the basin and flows into a large body of water, dries up, goes underground, etc).

In this study, the stream ordering ranks have been replaced with the variable 'n.' Therefore, first order streams are 'n order' channels, 2nd order are 'n+1' channels, 3rd order are 'n+2,' and so on. The replacement of ordinal ranks with the 'n' variable is an easy way to account for an undetected stream orders (i.e. n-1) due to the limited resolution of the imagery. Therefore, to avoid confusion between first order streams and 'true' first order steams (i.e. the order too small to resolve in the imagery), this study scraps the ordinal ranking of stream orders in favor of variations of 'n.'

The constructed channel network segments orders (both yellow and dark blue channels) were dissected and re-colored to correspond to their particular stream order (figure 4.10 – 4.14c).

The orders are colorized as follows: [n] - light blue, [n+1] – green, [n+2] - red, [n+3] – purple, [n+4] - orange, and [n+5] - yellow.

4.4.4: Bifurcation calculation

Once the ordering process was completed at each basin, the relationships between different orders within each channel network were assessed. The key piece of data produced by the stream ordering technique is the bifurcation ratio (R_b), which is the ratio between the channel segments in any given order to the number of channel segments in the next highest order, rounded to 1 decimal (Ritter et al., 2002; Ward and Trimble, 2004). For example, Basin A contains 39 [n] order segments and 13 [n+1] order segments (table 2), which leads to a bifurcation ratio between the two orders of 3.0 (39/13). Once calculation of each order's R_b is completed, the mean bifurcation ratio is found by dividing the summation of a basin's bifurcation ratios (10.3 for Basin A) by the number of total ratios (Basin A has 4). Thus, Basin A (10.3/4) has a mean bifurcation ratio of 2.6 (table 4.2).

The significance of the basin-wide bifurcation ratio is that it can be used to identify stream segments that escape visible detection. By multiplying the mean R_b of Basin A (2.6) by the number of channel segments in Basin A's lowest order (39), the number of channels in a hypothetical, smaller order can be calculated (39 x 2.6 = 101). Thus, the mean bifurcation ratio constrains the number of channels that might exist in a smaller, undetected order (Ritter et al., 2002). Given the resolution of the available radar imagery (~350 m/pixel – 1.5 km/pixel) it is highly likely that smaller, undetected orders of stream segments exist within each of the three Titanian basins. As such, the calculated stream ordering values are extended to include a hypothetical order that is too small to discern in the imagery. The process is extended to the Oman and Nevada basins as well.

4.5: Results

The number of stream segments found in each order are listed in table 4.1, and the ratios between the orders are displayed in table 4.2 with basin-wide, mean bifurcation ratios in red font at the bottom of table 4.2. Both Basin C and the Oman Basin fall within the average range of bifurcation ratios for basin on Earth with identical bifurcation values of 3.4, Basin A is below the average range at 2.6, and Basin B and the Nevada Basin are both above the average range at 8.1 and 5.5 respectively. Table 4.2 indicates that only the Oman Basin has stream orders of 'n+5' magnitude, Basin A and C have up to 'n+4,' the Nevada Basin has a maximum order of 'n+3,' and Basin B only has up to 'n+2' order channels. Therefore, the dendritic networks (Basin A, Basin C, and the Oman Basin) display higher order complexity compared to the linear/contorted networks of Basin B and the Nevada Basin. The increased complexity of the dendritic basins stems from the higher number of channels within the peripheral branches of the dendritic networks that combine before joining the central trunk of the networks. In contrast, the Nevada Basin and Basin B possess numerous [n] and [n+1] order channel segments that drain directly into a central trunk without first combining into [n+2] or [n+3] branches.

Table 4.1: Summary of Channel Segment Totals for each Basin

Stream Orders	Basin A	Basin B	Basin C	Oman Basin	Nevada Basin
***n-1**	*101*	*397*	*343*	*1146*	412
n	39	49	101	337	75
n+1	13	12	37	89	22
n+2	4	1	10	25	2
n+3	2	N/A	2	5	1
n+4	1	N/A	1	2	N/A
n+5	N/A	N/A	N/A	1	N/A

Shows the number of stream segments (both yellow and dark blue segments) found in each order for the three Titanian basins and the two Terrestrial analogs.

Table 4.2: Summary of Bifurcation Ratios of each Basin

Order Ratios	Basin A	Basin B	Basin C	Oman Basin	Nevada Basin
n/(n+1)	3.0	4.1	2.7	3.8	3.4
(n+1)/(n+2)	3.3	12.0	3.7	3.6	11
(n+2)/(n+3)	2.0	N/A	5.0	5.0	2
(n+3)/(n+4)	2.0	N/A	2.0	2.5	N/A
(n+4)/(n+5)	N/A	N/A	N/A	2.0	N/A
(total):	10.3	16.1	13.4	16.9	16.4
(mean R_b):	**2.6**	**8.1**	**3.4**	**3.4**	**5.5**

Displays the bifurcation ratios calculated between each order of the Titanian and Terrestrial basins. Mean bifurcation ratios for each basin (red font) are also included.

Figures 4.10 – 4.14 are each comprised of three different images. The top image of figures 4.10 - 4.14a displays either a radar crop (for the Titan basins) or the Google Earth image (for the Terrestrial basin) over which the channel networks were traced. The middle portion of figures 4.10 – 4.14 (b) shows the yellow and blue channels that comprise the constructed channel networks for each basin. The bottom image of each figure (c) is the same channel network shown in figure 4.10 - 4.14b, but re-colored to represent the stream ordering breakdown of each basin. An important observation is the enhanced channel density of the Oman and Nevada basins in figures 4.13 and 4.14 compared to the Titan basins in figures 4.10 – 4.12. The increased drainage density of the Terrestrial basins stems from the superior resolution of Google Earth imagery compared to the SAR images recorded by Cassini's Titan Radar Mapper. However, even the Google Earth imagery is unable to display the full complexity of the Nevada and Oman basins, which became apparent once I increased the resolution of the satellite imagery (i.e. zoomed in to extremely low altitudes of ~100 m). A more detailed discussion of how the Terrestrial basins compare to the Titanian basins is included in the discussion section.

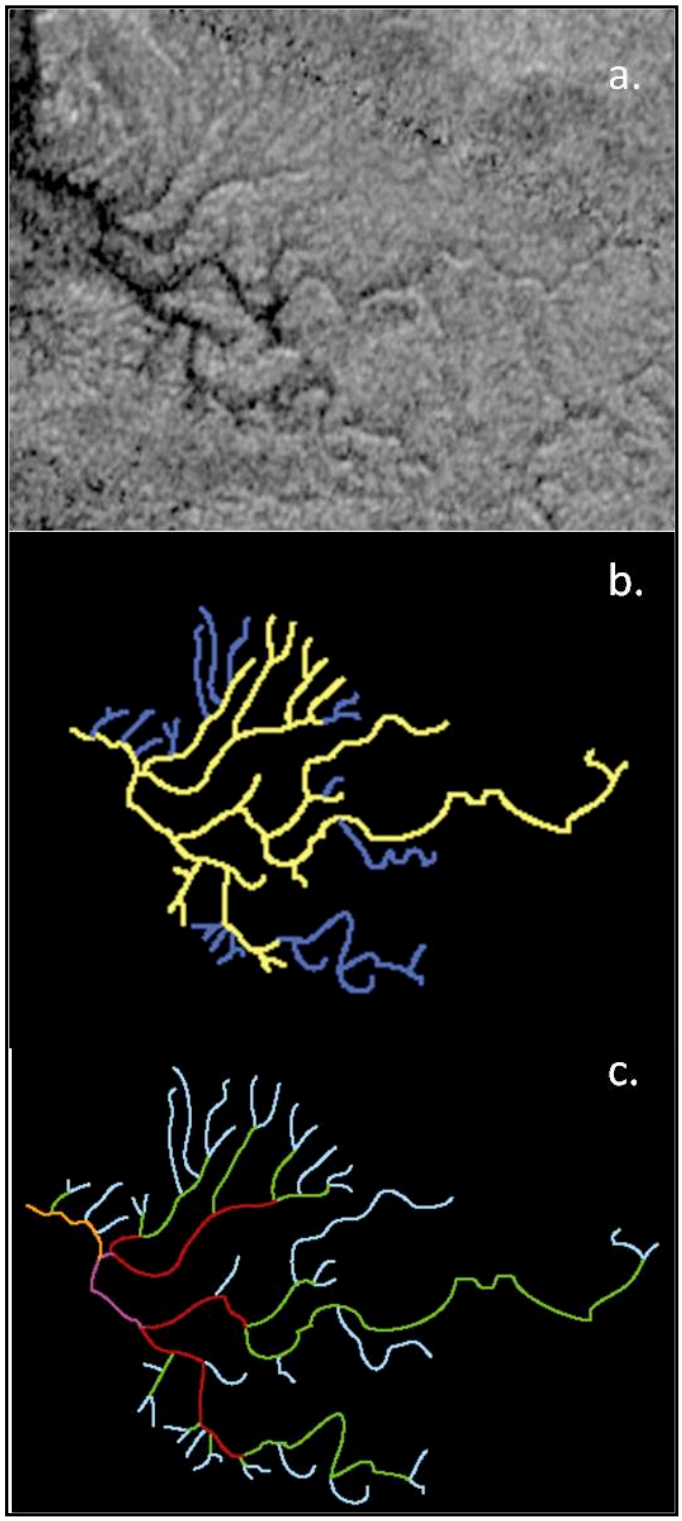

Figure 4.10: Basin A (triple image). (a) Cropped radar image of Basin A; **(b)** displays the constructed channel network at Basin A; **(c)** shows the stream ordering breakdown of Basin A. The furthest headwater is in the middle of the right-hand side, and the outlet is in the middle of the left-hand side of the image.

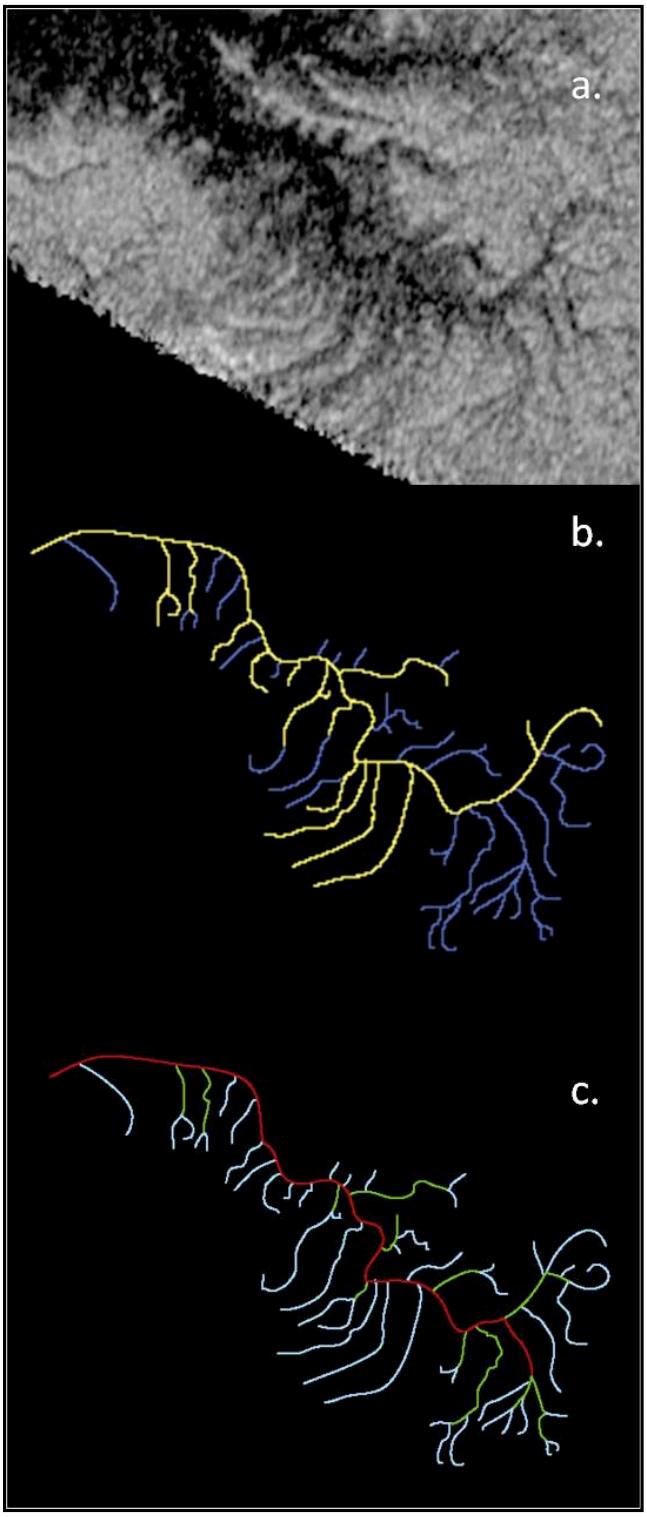

Figure 4.11: Basin B (triple image). (a) Cropped radar image of Basin B; **(b)** displays the constructed channel network at Basin B; **(c)** shows the stream ordering breakdown of Basin B. The furthest headwaters are in the upper and lower right-hand corners. The outlet is in the upper left-hand corner.

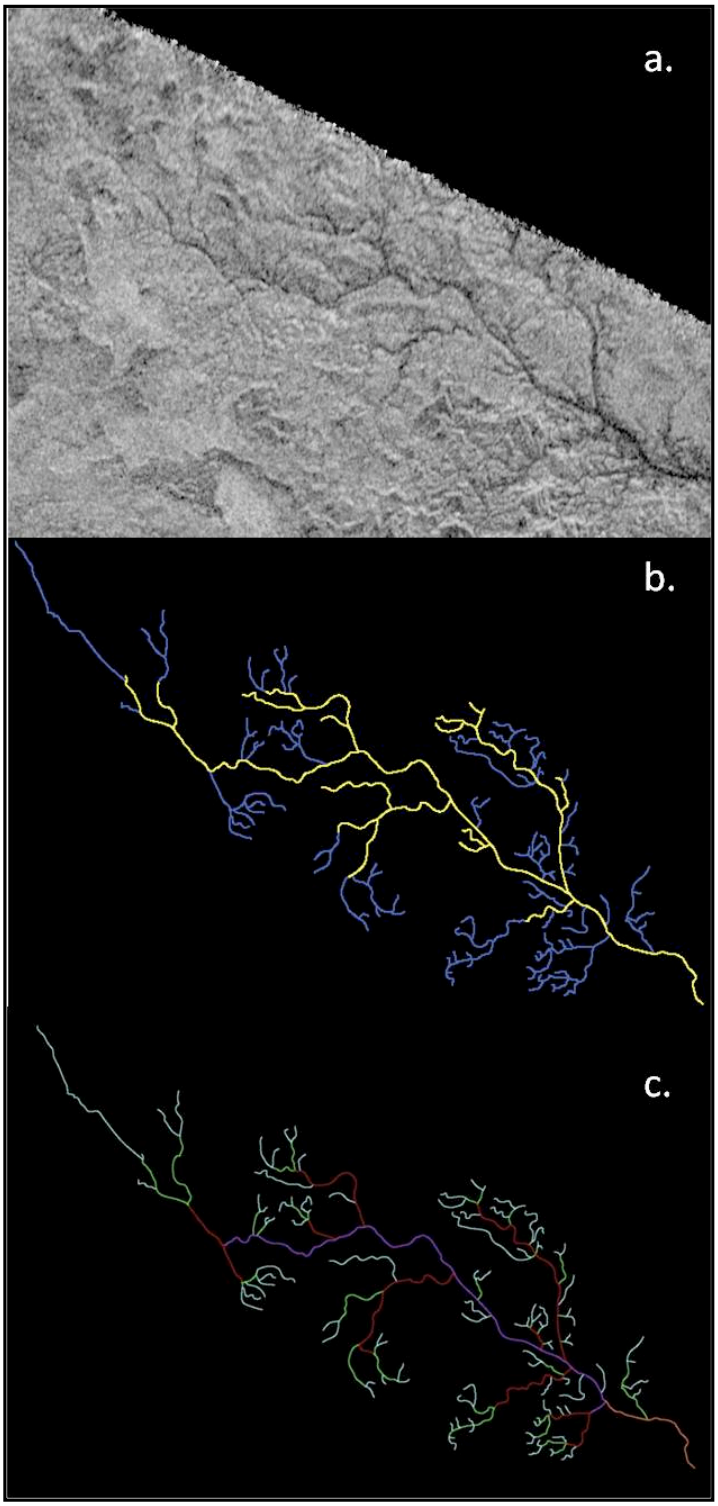

Figure 4.12: Basin C (triple image). (a) Cropped radar image of Basin C; **(b)** displays the constructed channel network at Basin C; **(c)** shows the stream ordering breakdown of Basin C. The furthest headwaters are in the upper left-hand corner. The outlet is in the lower right-hand corner.

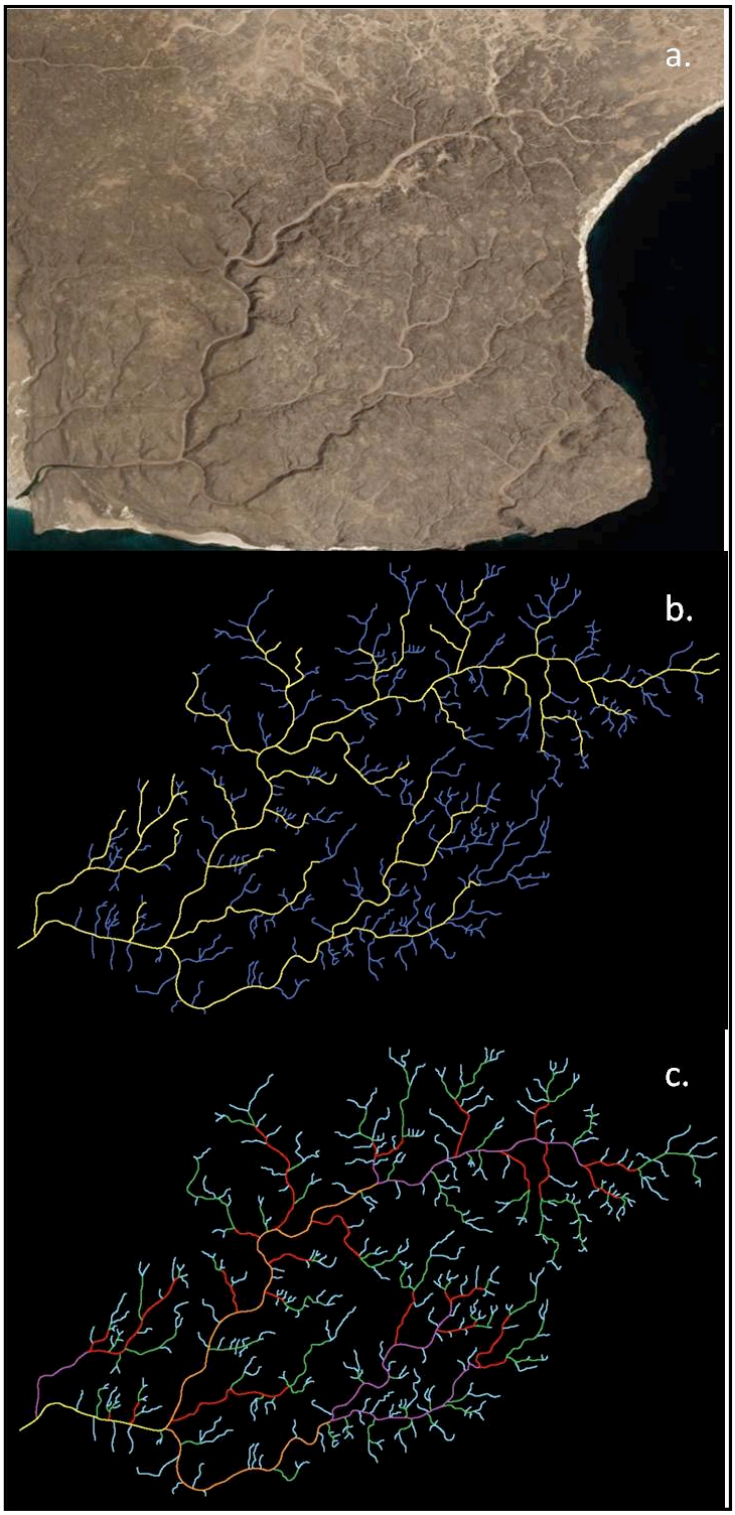

Figure 4.13: Oman Basin (triple image). (a) Cropped radar image of Oman Basin; **(b)** displays the constructed channel network at Oman Basin; **(c)** shows the stream ordering breakdown of Oman Basin. The furthest headwaters are in the upper right-hand corner. The outlet is in the lower left-hand corner.

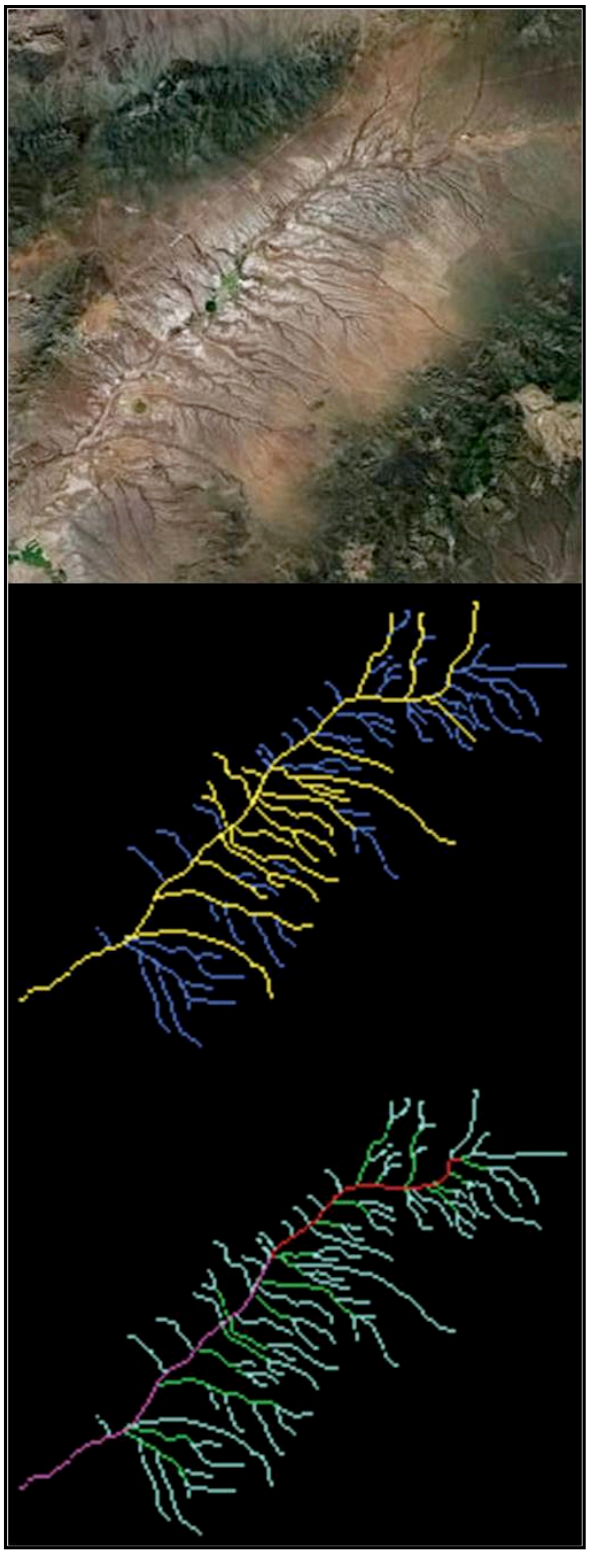

Figure 4.14: Nevada Basin (triple image). (a) Cropped radar image of Nevada Basin; **(b)** displays the constructed channel network at Nevada Basin; **(c)** shows the stream ordering breakdown of Nevada Basin. The furthest headwaters are in the upper right-hand corner. The outlet is in the lower left-hand corner.

4.6: Discussion

4.6.1: Channel networks

For all of the basins both yellow and dark blue channels were used to construct channel networks. The yellow, more visibly obvious, channels form the central trunks of each basin while the dark blue, more speculative, channels feed into their yellow counterparts. In several locations, more channels could have been included within the constructed channel networks; however, their exclusion was minor for two key reasons: (1) adequate network complexity already existed without their inclusion; (2) the excluded (potential) channels are more difficult to resolve than the dark blue channels. Thus, the excluded channels are even harder to see than the speculative dark blue channels, and their exclusion does not change the bifurcating relationships displayed at most of the sites.

Basin B, however, is significantly altered by the exclusion of a cluster of channel segments. Whether these channel segments (figure 4.15) are actually part of the basin, or simply noise or other features, is an unresolved matter. If Basin B's excluded channels are allowed to join up with the current network, then the bifurcation ratio for the basin changes significantly (from 8.1 to 4.5). However, beyond the resolution difficulties, the displayed morphology of the additional channels is best described as chaotic and counter to the prevailing contorted morphology of the basin as a whole. Therefore, the excluded channels do not look like they belong in Basin B and they are harder to discern than some of the dark blue channels.

The dark blue, more speculative, channels within each basin were as prevalent in the radar imagery of Titan as in the higher resolution, visible wavelength imagery of the Oman and Nevada basins. A conglomerate of reasons could combine to explain the ubiquitous nature of the dark blue channels including scaling, terrain differences, resolution disparities, etc. Perhaps most

importantly, even though the imagery of the Terrestrial basins possesses superior resolution to the radar data of the Titanian Basins, smaller channels are present at all scales. Therefore, even when the Oman and Nevada basins resolutions are maximized in Google Earth, difficult to resolve channels that are still persistent throughout the image. (i.e. blurry, distorted, etc).

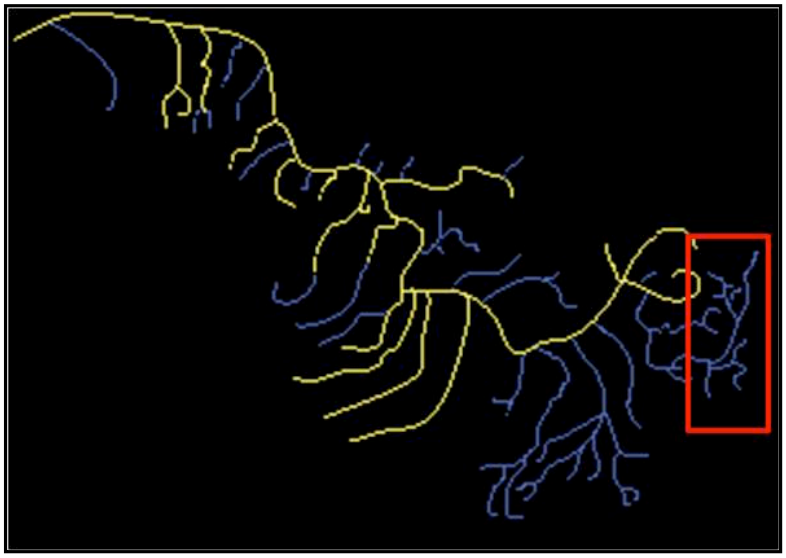

Figure 4.15: Basin B Omitted Channel Segments. Shows Basin B with the inclusion of additional dark blue channels (enclosed by red square). Note the chaotic nature of the excluded channels.

4.6.2: Stream ordering

The ordered channel networks (figure 10-14c) of the Basins include: [n], [n+1], [n+2], [n+3], and [n+4] orders (except for Basin B which stops at [n+2]). The Oman Basin has an additional order [n+5] most likely stemming from the enhanced resolution of the Google Earth imagery versus the available radar imagery of Titan.

The hypothetical order included in this study [n-1] indicates how many channel segments might exist in a smaller, unseen order. Each Basin produced fairly different [n-1] values because of the range in the basin-wide bifurcation ratios (and the range in the number of segments within each Basin's [n] order). For example, Basin B produced an analogous number of [n-1] channel

segments (397) compared to Basin C (343) even though Basin B possesses only 49 [n] channels and Basin C has 101. The large disparity in R_b values between Basin B and C (R_b = 8.1 and 3.4 respectively) explains why these basins can exhibit similar [n-1] values despite their significantly different [n] values.

4.6.3: Bifurcation ratios

The mean bifurcation ratio calculated for Basin C and the Oman Basin (both have R_b = 3.4) falls within the normal range encountered for drainage basins on Earth with high drainage densities (3.0 – 5.0) (Strahler, 1952). Basin A is slightly below the normal range (R_b = 2.6), the Nevada Basin (R_b = 5.5) is slightly above the normal range, and Basin B (R_b = 8.1) is noticeably higher than the normal range of bifurcation values on Earth. It is important to remember that Basin B is a peculiar case because of the drowned tributaries that are roughly perpendicular to a central linear trunk. Without a central trunk to drain the branches of Basin B, the bifurcation relationship shared by the different channels within Basin B involves fewer orders than the other Titan basins, as only 3 stream orders exist within Basin B. In a similar fashion, the Nevada Basin has many low-order tributaries flowing into a central trunk. The Nevada Basin is shaped by the tectonic regime of its surrounding landscape (i.e. central fissure that numerous peripheral channels drain into), and perhaps Basin B is also shaped by tectonic forces stemming from mantle plumes uplifting blocks of ice - similar to tectonic uplift via extensional ridges on Earth (Radebaugh et al., 2007). Therefore, only the bifurcating rates of liquid-methane cut channels observed at Basin A and C are similar to the rates exhibited on Earth for water-cut stream networks in arid environments like the Oman Basin while Basin B, and its perpendicular tributaries, produce an R_b well outside the average range and is more comparable to the Nevada Basin.

The significance of calculating bifurcation ratios for basins on Titan is that it allows for immediate comparison with similar morphological patterns displayed by basins on Earth. Consequently, the formation histories and lithology of Terrestrial basins can quickly be applied to Titanian basins with similar morphologies. While the processes that form basins on Titan are likely quite different from the processes that form Terrestrial basins, the connections between bifurcation ratio, basin morphology, and formation history are noteworthy and subsequent analysis of channel networks on Titan would benefit from the production of bifurcation ratios and comparison to Terrestrial basins with similar R_b values.

4.6.4: Titanian basins versus Terrestrial analogs

Given the high drainage density of the basins, the lack of vegetation on Titan, and the seasonally variable precipitation rates (e.g. Rannou et al., 2006), the region mirrors arid environments on Earth like the Oman and Nevada basins. While it is unclear whether the liquid-methane carved channels analyzed in this study are enclosed by canyons, the available topographic data (NASA image PIA10353) suggests that there is a steady increase in slope close to the perimeter of the polar estuary. This increasing slope is not conclusive evidence of a canyon-like landscape, but at the very least, it suggests that the surrounding basins might be experiencing some sort of heightened down-cutting.

The Oman Basin compares most favorably to Basin C, because they share identical bifurcation ratios and similar dendritic morphologies. Furthermore, the Oman Basin cuts through a small uplifted plateau, and Basin C appears to navigate through a topographically varied section of the Titanian surface. While the evidence is sparse and dependent on the developing topographical data, Basin C could be cutting through an uplifted section of water-ice bedrock

similar to the Oman Basin carving pathways through uplifted silicates. Basin A is similar to the Oman Basin as well, but its morphology is not quite the perfect match of Basin C.

Basin B, as discussed in the previous section, is more similar to the Nevada Basin versus the Oman Basin. Basin B and the Nevada Basin both have numerous perpendicular tributaries flowing into a central linear trunk. Basin B's central trunk, however, is a drowned branch of Kraken Mare while the Nevada Basin is ephemeral and is not flooded. The morphology of the Nevada Basin is strongly controlled by the crustal thinning beneath the low-lying valley that it resides in. In a similar fashion, Basin B could be surrounded by rising crustal material that is forcing the basin into a confined area. Furthermore, linear channels are typical features of basins shaped by tectonic forces on Earth (i.e. fractures and fissures); as such, the linear nature of Basin B's central trunk (and its perpendicular tributaries) could suggest that cryotectonics are changing the landscape of the region, leading to the uplifting of water-ice blocks and the thinning of crustal material in areas adjacent to the uplift.

4.6.5: Radar complications

There are inherent difficulties with the interpretation of radar imagery from Titan. Given the mean surface temperature of 94 K, and the expected chemical regime (i.e. assumed composition of the surface), the scattering properties exhibited are likely to be different than for Earth and Venus, which are the only other surfaces imaged with space borne radar (Campbell, 2002). As such, comparison of Terrestrial drainage basins, observed by SAR systems, with the radar imaged Titanian basins will strengthen the image interpretation process and the related channel network construction on Titan. Future work that compares basins on Earth imaged using synthetic aperture radar with basins on Titan imaged by Cassini will aid in the interpretation of the Titanian channel networks.

4.7: Conclusions

The bifurcation ratio of Basin C falls within the average range of values displayed by Terrestrial arid basins (like the Oman Basin) with a high drainage density (3.0 -5.0). The bifurcation ratio of Basin A (2.6) is slightly lower than the average R_b on Earth, and Basin B's R_b (8.1) is significantly higher. Basin C compares the most favorably with the Oman Basin while Basin B is similar to the Nevada Basin. An expansion of the number of Titanian basins and Terrestrial basins is needed to strengthen the comparison between channel networks on Earth versus Titan. Other arid landscapes on Earth could further scientific understanding of how liquid methane creates organized channel networks on Titan. Also, a comparison between basins in different locations across Titan would be a useful endeavor. Overall, methane-cut basins on Titan and water-cut basins on Earth are remarkably similar given the differences in gravity, surface composition, and the erosional agent involved.

Topographical data for all of Titan is a work in progress where overlapping swaths allow for stereographic analysis. Given the uncertainty in the available elevation data, it is difficult to know exactly where some of the more speculative, dark blue stream segments within the Titanian basins flow, and where they join the higher order main trunks of the basins. Future work that uses the developing topographical data should be incorporated into subsequent channel network analysis. Also, the role of cryotectonics and cryovolcanism across Titan, but specifically around the north pole, could help explain why large seas of hydrocarbons exist in the region, but nowhere else on Titan. The simplest explanation could be that topographical variations in the region dominated by the large maria allows for liquids to accumulate on the surface. However, such a statement begs the question – why does this portion of Titan have topographical variation? This is where cryotectonics might come into play as giant blocks of water-ice bedrock

could be hypothetically pushed up through the lithosphere, driven by convective mantle processes below (Radebaugh et al., 2007). Therefore, future work that seeks to explain the morphology of Titanian basins must include the emerging topographical data and account for the underlying drivers of geomorphic activity across Titan.

CHAPTER 5.

CONCLUSIONS AND DISCUSSION REGARDING THE IMPLICATIONS OF THIS STUDY

5.1: Investigation of Titan's Surface

The Cassini orbiter has spent the past 5 years exploring the depths of the Saturnian system, sending breath-taking imagery of the puffy gas giant and its many satellites back to Earth. Obtaining imagery of Saturn's largest moon, Titan, which is also the second largest moon in the Solar System, was a key mission objective even before the launch of Cassini in 1997; consequently, project designers equipped Cassini with viewing technology capable of piercing the dense methane fog surrounding Titan (Lorenz and Mitton, 2008). One of the primary viewing instruments onboard Cassini is the Titan Radar Mapper, which produces the finest resolution images available of the moon's surface. The images produced by the SAR mode of Cassini's radar have revealed a surface sculpted by geomorphic processes, including fluvial erosion and channelized flow (Perron et al., 2006), dune field production and migration (Mitchell, 2008), and cryovolcanic eruptions with 'magmatic' liquid-water flows (Nelson et al., 2009). These agents of change continually resurface Titan, burying old features under layers of debris while exposing bedrock in other places. To study the evolving surface of Titan, this document focused on selected channel networks around the large hydrocarbon seas of Titan's north pole.

5.2: Bedload Transport in Basin A

Sediment transport of water-ice grains in liquid methane on Titan is similar to water transporting quartz grains on Earth; however, each world requires starkly different values for a variety of terms defining the entrainment of sediment (Burr et al., 2006). Titan, with its lower

gravity, requires steeper slopes for sediment (of an analogous grain diameter) to be entrained compared with grains on Earth (Collins, 2005). However, the lower gravity of Titan also enhances sediment removal because water-ice and precipitated organics are more buoyant in liquid methane than silicates are in water. Overall, sediments in Titanian channels are expected to become entrained in flow depths about half as deep as a particular grain size requires on Earth (Burr, 2006). As such, seasonal precipitation, stemming from large convective storms (e.g. Barth and Rafkin, 2007), should lead to mobilizing flows, channel incision, and large volumes of sediment moving downstream.

Without the benefit of *in situ* measurements, topographic maps like PIA 10353 are the best available data sources for interpreting the slope of a given region on Titan. Along with a variety of terms defined elsewhere (see table 1.1), it is possible to estimate the bedload entrainment potential of channel networks contained within the DTM that generated PIA 10353. The results show that sediment grains with 75 mm diameters could be entrained in flows of about 1.6 m deep along the selected channel of Basin A. However, the steeper portions of Basin A could entrain 75 mm water-ice grains in flows as shallow as ~1 m. Thus, the slope of the region is a crucial parameter for estimating the potential of sediment transport in Basin A. Subsequent topographical data concerning the region will help constrain the processes at work and resulting features recorded in the SAR generated swaths covering the north polar landscape.

In Basin A, the downstream increase in slope close to the polar mare branch is an intriguing feature in the data. Normal streams on Earth experience a decrease in slope towards their outlet, but headward erosion (i.e. erosion of the channel away from the outlet back upstream) is a common feature in many terrestrial landscapes where a fluctuating water level leads to the continual adjustment of a stream to new conditions. Whether the near-outlet drop in

elevation is a real feature or an artifact buried within PIA 10353 is unclear; however, some researchers (Hayes et al., 2008) believe that the polar lakes are connected through a porous regolith, which would enable the lakes to 'share' liquid hydrocarbons. The subsurface flow of liquid amongst the polar lakes would in effect lead to fluctuating lake levels as fluids transfer from one lake to another. The fluctuating lake levels could help explain the sudden topographical dip close to the outlet of Basin A. As the outlet of Basin A adjusts to the fluctuating lake level, it is forced to erode further down when the mare it drains into is 'low,' and becomes flooded when the mare is 'full.' Thus, the downstream section of Basin A might be in a perpetual state of adjustment to fluctuating conditions, similar to eustatic sea level changes that affect coastal areas of Earth.

The denudation rates calculated in chapter 3 suggest that different parts of Basin A are eroding down to base level at different rates. Furthermore, the amount of time required to erode to base level places an important constraint on the minimum age of the terrain. The denudation rate of the downstream zone suggests that ~2200 Earth years of constant flow (1.5 m) are required to erode the landscape down to the lake level at the outlet of Basin A. Given that Basin A is still adjusting towards base level, the basin cannot be older than ~2200 years or else the downstream zone would no longer exist. It is important to note that the denudation rates assume constant flow of a given depth. Therefore, it might only take ~2200 Earth years to erode the landscape of Basin A_{ds} down to base in theory, but in reality, no combination of precipitation events is going to produce a constant 1.5m of flow over a long enough time period to erode the landscape of Basin A down to base level. As such, the denudation rates calculated in this study serve as useful constraints on the minimum age of the landscape (as measured backward from now) and the minimum amount of time for Basin A to erode to its base level.

5.3: Channel Networks and Stream Ordering

Channel networks on Titan have strikingly similar morphologies to Terrestrial drainage basins. This document investigated the morphology of three Titan basins by constructing channel networks, conducting stream ordering, and calculating bifurcation ratios at several selected sites around Titan's north pole. The networks compare favorably with earthbound basins in arid landscapes due to their low precipitation amounts and the lack of vegetation on Titan. An analog basin simply referred to as the 'Oman Basin' is strongly correlated to Basin C, somewhat similar to Basin A, and entirely dissimilar from Basin B and its drowned tributaries. Future work needs to expand the sample size and include more basins from both worlds with a larger variety of basin morphologies.

The stream morphology displayed at Basin A and C is dendritic; Basin B, however, is not dendritic and possesses a noticeably 'contorted' morphology. Basin B has no main trunk into which the tributaries flow because the basin is located in the midst of a series of drowned valleys. The tributaries of Basin B flow into a somewhat linear branch of Kraken Mare where normally a central trunk would drain the headwaters. Consequently, Basin B has a significantly higher bifurcation ratio than Basin A or C as it never manifests higher than an [n+2] channel (versus [n+4] at Basin A and C). The formative processes that shaped Basin B are difficult to assess remotely. The basin-range nature of the Nevada Basin, however, could shed light on why Basin B is characterized by long perpendicular channels that flow into the mare branch instead of a central drainage basin trunk. The low-lying valley where the Nevada Basin is located undergoes crustal thinning that creates long linear channels with numerous perpendicular tributaries feeding into the central straight channel. Such a morphology is very similar to Basin B, and perhaps similar tectonic forces shape this peculiar Titanian basin.

The Titanian basins analyzed in this study display morphologies similar to drainage basins on Earth in arid environments where infrequent and intense storms can dramatically sculpt the desert terrain. Basins A and C are fairly similar and dendritic while Basin B is a standout for its unusual appearance and drowned tributaries. The morphology of these basins can help explain the genetic history of each site as the liquid methane-cut channels continually adjust to their changing surroundings – just like water-cut channels in dynamic environments on Earth. Therefore, by analyzing what channel networks on Titan look like, it is possible to constrain how each network formed based on comparisons with Terrestrial basins that have similar morphologies.

5.4: Implications of Fluvial Processes on Titan

Titan's prevailing fluvial processes lead to the formation of channel networks that look strikingly similar to those on Earth. While these Titanian fluvial processes likely have specific nuances that impact the formation of channels on local scales, it is clear that on a regional scale, fluvial features (i.e. channels and lakes with rough coastlines) are very similar in appearance to the same features on Earth. However, how can fluvial features formed by such disparate substances end up looking so similar? This question is more philosophical than quantitative, but the intellectual importance of why different fluids carve dissimilar landscapes in such analogous fashions is tantalizingly clear: worlds analogous to Earth do not have to be made out of the same materials to create similar landscapes. Liquids on Earth and Titan flow in analogous patterns simply because the energy to move flows down slope, cutting down towards a base level while transported, is a fundamental process that shapes not only our planet, but others in our Solar

System and presumably beyond. Thus, analogous worlds to Earth do not have to be made of the same materials in order to mimic the same fundamental surface processes.

5.5: Cryotectonic Forces and Basin C

The highlands and ridges surrounding the north polar seas present an intriguing mystery that might help explain why liquid hydrocarbon reservoirs are able to pool in the region, while on other parts of Titan with muted topography, liquid methane precipitation simply runs off and evaporates, unable to collect at the surface. The existence of the elevated regions around the polar seas raises two important questions: (1) Is tectonic uplift the formative process of the elevated highlands around the polar lakes? (2) Are cryotectonics an ongoing process or are the elevated regions relic features of activity in the geologic past? Tectonic uplift on Titan could be facilitated by shifting ice blocks in the lithosphere – pushed up by convective plumes in the moon's mantle (Radebaugh et al., 2006). These blocks could act in a similar fashion to uplifted blocks on Earth that are pushed up by compressional forces acting upon on portions of the crust (Turcotte and Schubert., 2002).

Of interest here are the western 'downstream' reaches of Basin C. Basin C displays a dendritic morphology for most of its length until it veers towards the nearby Ligeia Mare to its north. At this point, the trunk of the basin appears to flow into the mare, but it also continues onwards towards another juncture (figure 5.1), and it seems to branch southward as well to join another basin beyond the extent of figure 5.1. Several explanations for the mess of channels comprising the downstream section of Basin C are feasible given the available evidence concerning surface processes on Titan: (1) misinterpretation of the imagery, (2) fluctuating methanological table, (3) cryovolcanic uplift.

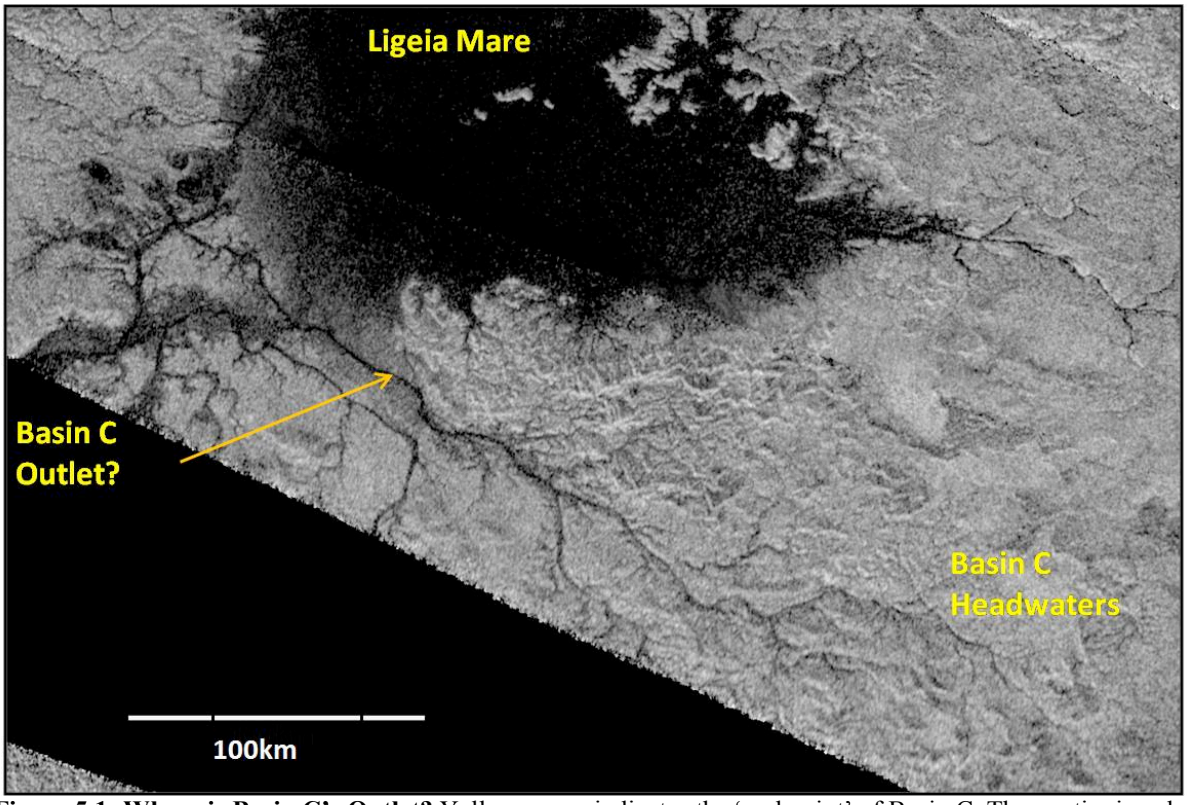

Figure 5.1: Where is Basin C's Outlet? Yellow arrow indicates the 'end point' of Basin C. The continuing channel west of the arrow is not considered in this study. Ligeia Mare is to the north of Basin C, in the top left-hand corner of figure 5.1. Source:Cassini Radar Team.

(1) Given the nature of radar instruments penetrating the thick atmosphere, and recording images from the altitude of the Titan flybys depicting Basin C, it is possible that the interpretation of the downstream end of Basin C presented in this document is incorrect; as such, perhaps the downstream channel visible in figure 5.1 (west of the yellow arrow) are relict segments that no longer possess flow and are covered by a shallow depth of liquid hydrocarbons stemming from the nearby maria to the basin's north. Paillou and colleagues (2008) suggest that Cassini's SAR mode should be able to penetrate several meters of liquid methane. Thus, Cassini's radar equipment might be imaging a submerged channel that has been drowned by Ligeia Mare.

(2) A fluctuating methane table in the subsurface might control the region's laci/maria levels (Mitchell et al., 2009). As such, Ligeia Mare's level is rising, and consequently Basin B has been re-routed into it. Using this theory, the channels past the mare are no longer carrying flow, and the backscatter from the channel is due to material lining the channel (see Barnes et al., (2007) for a discussion on radar properties of empty channels). This scenario could help explain the multiple channels that fork away from the trunk of Basin C at the downstream end; however, this theory does not explain why the channels further west of the Basin C trunk seem to flow north, south, and in other directions. Even if these 'former' channels no longer carry flow, why are they so disorderly, seemingly carrying flow both up and down slopes?

(3) The downstream morphology of Basin C might be due to cryotectonic uplift. If a highland area is actively 'growing' in the downstream portion of Basin C (i.e. a crustal block of water-ice bedrock is being pushed upward, then the multiple avenues of flow become more plausible. In this scenario, some of the downstream network is comprised of relict channels that previously transported liquid hydrocarbons (but no longer do so), and some of the network is comprised of newly formed channels responding to the change in elevation. An obvious follow up question to this scenario is which of the visible channels are relict features, and which are the newly created channels? In other words is Basin C currently flowing north into the mare or is this the former direction of flow, and currently, Basin C is flowing south, merging with another basin? This question is currently impossible to answer based on the available imagery. However, the more light that is shed on the formative processes that shaped Basin C, the more the direction of downstream flow could come into focus.

5.6: Role of Topography

An intriguing aspect of Titan's surface is the spatial distribution of hydrocarbon lakes. While large polar maria exists between 220°W and 350°W, other portions of Titan above 55°N have few, if any, surface hydrocarbon reservoirs, and where lakes do exist, they are much smaller than the great maria and display dissimilar morphologies from them. Furthermore, no lakes have been imaged between the equator and 55°N (Stofan et al., 2007), and very few have been identified at high latitudes around the south pole – even though the south pole had just recently experienced Titanian summer, and the associated liquid methane convective storms (e.g. Schaller et al., 2006) that can cover up to 10% of the surface (Griffith et al., 2000). Why is so much liquid methane and ethane stored in the relatively dry darkness of the north pole and why is it clustered between certain meridians? One compelling theory to explain the spatial and seasonal disparities in surficial liquid hydrocarbon locations is that the maria in the 'Lake District' are surrounded by highland topography (R. Kirk, USGS and Cassini Radar Team associate, personal communication) that makes the pooling of hydrocarbons more efficient while in other parts of Titan, precipitated liquid hydrocarbons simply dissipate into the subsurface after 'flashflood' events – unable to concentrate into lakes and seas.

5.7: 'Ground-Methane' Seepage

Given the appearance of some of the channels in the 'Lake District,' coupled with the potential for localized uplift, it is possible that some of the imaged channels and stream networks were created by subsurface seepage in conjunction with precipitation-driven formation (R. Kirk, USGS and Cassini Radar Team associate, personal communication). If the region does possess a fluctuating methane table (Mitchell et al., 2009), then it is possible that at any given time large

reservoirs of liquid methane lie close to the surface. If such sources of liquid hydrocarbons were uplifted in conjunction with water-ice bedrock via mantle plumes from beneath, then it is plausible that the liquid could 'seep out' of the bulging crust - like water draining from a saturated sponge. Evidence for 'ground-methane' seepage exists in other parts of Titan (e.g. Tomasko et al., 2005); as such, subsurface flows might also carve the landscape of the polar basins observed in this document.

5.8: Complications with radar data interpretation

Given the mean surface temperature of 94K, and the expected chemical regime (i.e. assumed composition of the surface), the scattering properties exhibited are likely to be different than for Earth and Venus, which are the only other surfaces imaged with space borne radar (Campbell, 2002). As such, data interpretation of the Titanian surface is still a bit of a developing process. Thus, comparison of Terrestrial drainage basins, observed by SAR systems, with the radar imaged Titanian basins would strengthen the image interpretation process, but radar imagery of Earth compared to Titan should have many subtle differences given the disparate materials composing the surface of each world.

5.9: Future work

Subsequent analysis of channel networks around Titan's north polar seas should incorporate additional examples of drainage basins not included in this document. Also, more analogous Terrestrial basins are needed to compare to the Titanian basins beyond the Oman and Nevada basins included here. Terrestrial analogs added to this study should ideally be found using radar imagery of Earth. While the surface properties of Earth should produce a different

radar signature than the surface of Titan, comparison on radar data from both worlds would strengthen the analysis of the Titanian basins.

Future work concerning sediment transport will use data from the developing topography map of the polar seas. This new topography map will be much larger than the existing one (PIA 10353); furthermore, it will use the new coordinate system, which was developed after the original topography map was released. Given the advantages of the new map, subsequent sediment transport analysis will extend the work covered in chapter 3 of this document in order to further constrain the denudation rate and the bedload transport potential of water-ice grains.

References

Atreya, S. 2007. Titan's Organic Factory. *Planetary Science*. 316: 843-45.

Atreya, S., E. Adams, H. Niemann, J. Demick-Montelara, T. Owen, M. Fulchignoni, F. Ferri, and E. Wilson. 2006. Titan's methane cycle. *Planetary and Space Science* 54: 1177-87.

Barnes, J., R. Brown, L. Soderblom, B. Buratti, C. Sotin, S. Rodriguez, S. Le Mouelic, K. Baines, R. Clark, P. Nicholson. 2006. Global-scale surface spectral variations on Titan seen from Cassini/VIMS. *Icarus* 186: 242-58.

Barnes, J., J. Radebaugh, R. Brown, S. Wall, L. Soderblom, J. Lunine, D. Burr, C. Sotin, S. Le Mouelic, S. Rodriguez, B. Buratti, R. Clark, K. Baines, R. Jaumann, P. Nicholson, R. Kirk, R. Lopes, R. Lorenz, K. Mitchell, and C. Wood. 2007. Near-infrared spectral mapping of Titan's mountains and channels. *Journal of Geophysical Research – Planets* 112: E11006, doi:10.1029/2007JE002932.

Barth, E., and S. Rafkin. 2007. TRAMS: A new dynamic cloud model for Titan's methane clouds. *Geophysical Research Letters.* 34: L03203, doi:10.1029/2006GL028652.

Brown, M., A. Bouchez, and C. Griffith. 2002. Direct detection of variable tropospheric clouds near Titan's south pole. *Letter to Nature* doi:10.1038/nature01302.

Brown, R., L. Soderblom, J. Soderblom, R. Clark, R. Jaumann, J. Barnes, C. Sotin, B. Buratti, K. Baines, and P. Nicholson. 2008. The identification of liquid ethane in Titan's Ontario Lacus. *Nature Letters* 454: 607-10.

Burr, D., J. Emery, R. Lorenz, G. Collins, and P. Carling. 2006. Sediment transport by liquid surficial flow: Application to Titan. *Icarus*. 181: 235-42.

Campbell, B. 2002. Radar Remote Sensing of Planetary Surfaces. Cambridge: Cambridge UP.

Clayton, J., and J. Pitlick. 2007. Spatial and temporal variations in bed load transport intensity in a gravel bed river bend. Water Resources Research 43: W02426, doi:10.1029/2006WR005253

Clayton, J. 2005. Sediment Transport and Channel Form in Gravel-Bed River Meanders. PhD diss., Colorado University.

Collins, G. 2005. Relative rates of fluvial bedrock incision on Titan and Earth. *Geophysical Research Letters* 32: L22202, doi:10.1029/2005GL024551.

De Pater, I., and J. Lissauer. 2001. *Planetary Sciences.* New York: Cambridge University Press.

Elachi, C., S. Wall, M. Allison, Y. Anderson, R. Boehmer, P. Callahan, P. Encrenaz, E. Flamini, G. Franceschetti, Y. Gim, G. Hamilton, S. Hensley, M. Janssen, W. Johnson, K. Kelleher, R. Kirk, R. Lopes, R. Lorenz, J. Lunine, D. Muhleman, S. Ostro, F. Paganelli, G. Picardi, F. Posa, L. Roth. R. Seu. S. Shaffer, L. Soderblom, B. Stiles, E. Stofan, S. Vetrella, R. West, C. Wood, L. Wye, H. Zebker. 2005. Cassini Radar Views the Surface of Titan. *Science* 308: 970-74.

Griffith, C., J. Hall, and T. Geballe. 2000. Detection of daily clouds on Titan. *Science* 290: 509-13.

Griffith, C., T. Owen, T. Gaballe, J. Rayner, and P. Rannou. 2003. Evidence for the exposure of water ice on Titan's surface. *Science* 300: 628-30.

Griffith, C., P. Penteado, P. Rannou, R. Brown, V. Boudon, K. Baines, R. Clark, P. Drossart, B. Buratti, P. Nicholson, C. McKay, A. Coustenis, A. Negrao, and R. Jaumann. 2006. Evidence for a Polar Ethane Cloud on Titan. *Science* 313: 1620-22.

Hayes, A., O. Aharonson, P. Callahan, C. Elachi, Y. Gim, R. Kirk, K. Lewis, R. Lopes, R. Lorenz, J. Lunine, K. Mitchell, G. Mitri, E. Stofan, and S. Wall. 2008. Hydrocarbon lakes on Titan: Distribution and interaction with a porous regolith. *Geophysical Research Letters*. 35: L09204, doi:10.1029/2008GL033409.

Horton, R. 1945. Erosional Development of Streams and their drainage basins. Hydrophysical approach to quantitative morphology. *Geologic Society America Bull*. 56: 275-370.

Hueso, R., and A. Sanchez-Lavega. 2006. Methane storms on Saturn's moon Titan. *Nature*. 442: 428-31.

Jaumann, R., R. Brown, K. Stephan, J. Barnes, L. Soderblom, C. Sotin, S. Le Mouelic, R. Clark, J. Soderblom, B. Buratti, R. Wagner, T. McCord, S. Rodriguez, K. Baines, D. Cruikshank, P. Nicolson, C. Griffith, M. Langhans, R. Lorenz. 2009. Fluvial erosion and post-erosional processes on Titan. *Icarus* 197: 526-38.

Lebreton J-P., and D.L. Matson. 2002. The Huygens probe: science, payload and mission overview. *Space Science Review* 104: 59-100.

Lebreton, J., O. Witasse, C. Sollazzo, T. Blancquaert, P. Couzin, A. Schipper, J. Jones, D. Matson, L. Gurvits, D. Atkinson, B. Kazeminejad, and M. Perez-Ayucar. 2005. An overview of the descent and landing of the Huygens probe on Titan. *Nature* 438: 758-64.

Leopold, L., 1992. Sediment Size that Determines Channel Morphology. *In Dynamics of Gravel-bed Rivers*, ed. P. Billi, 297-311. New York: John Wiley & Sons, Inc.

Lillesand, T., and R. Kiefer. 2008. *Remote Sensing and Image Interpretation 6th edition.* New York: John Wiley & Sons, Inc.

Lorenz, R. 1993. The life death and afterlife of a raindrop on Titan. *Planetary and Space Science* 41: 647-55.

Lorenz, R., and J. Lunine. 1996. Erosion on Titan: Past and present. *Icarus* 122: 79-91.

Lorenz, R., and J. Lunine. 1997. Titan's surface reviewed: the nature of bright and dark terrain. *Planetary and Space Science* 45: 981-92.

Lorenz, R., and J. Lunine. 2005. Titan's surface before Cassini. *Planetary and Space Science* 53: 557-76.

Lorenz, R. 2006. The Exploration of Titan. *John Hopkins APL Technical Digest*, 27. 133-143.

Lorenz, R., K. Mitchell, R. Kirk, A. Hayes, O. Aharonson, H. Zebker, P. Paillou, J. Radebaugh, J. Lunine, M. Janssen, S. Wall, R. Lopes, B. Stiles, S. Ostro, G. Mitri, E. Stofan. 2007a. Titan's Inventory of Organic Surface Materials. *Geophysical Research Letters*. 35, L02206, doi:10.1029/2007GL032118.

Lorenz, R., C. Wood, J. Lunine, S. Wall, R. Lopes, K. Mitchell, F. Paganelli, Y.Anderson, L. Wye, C. Tsai, H. Zebker, and E. Stofan. 2007b. Titan's young surface: Initial crater survey by Cassini RADAR and model comparison. *Geophysical Research Letters* 34: L07204, doi:10.1029/2006GL028971.

Lorenz, R., R. Lopes, F. Paganelli, J. Lunine, R. Kirk, K. Mitchell, L. Soderblom, E. Stofan, G. Ori, M. Myers, H. Miyamoto, J. Radebaugh, B. Stiles, S. Wall, C. Wood, and the Cassini Radar Team. 2008. Fluvial channel on Titan: Initial Cassini RADAR observations. *Planetary Space Science.* 1016: 1-13.

Lorenz, R., and J. Mitton. 2008. *Titan Unveiled*. Princeton: Princeton University Press.

Lunine, J., D. Stevenson, and Y. Yung. 1983. Ethane Ocean on Titan. *Science.* 222: 1229-30.

Lunine, J., and S. Atreya. 2008. The methane cycle on Titan. *Nature Geoscience*. 1: 159-64.

Lunine, J., C. Elachi, S. Wall, M. Janssen, M. Allison, Y. Anderson, R. Boehmer, P. Callahan, P. Encrenaz, E. Flamini, G. Franceschetti, Y. Gim, G. Hamilton, S. Hensley, W. Johnson, K. Kelleher, R. Kirk, R. Lopes, R. Lorenz, D. Muhleman, R. Orosei, S. Ostro, F. Paganelli, P. Paillou, G. Picardi, F. Posa, J. Radebaugh, L. Roth, R. Seu, S. Shaffer, L. Soderblom, B. Stiles, E. Stofan, S. Vetrella, R. West, C. Wood, L. Wye, H. Zebker, G. Alberti, E. Karkoschka, B. Rizk, E. McFarlane, C. See, and B. Kazeminejad. 2008. Titan's diverse landscapes as evidenced by Cassini RADAR's third and fourth looks at Titan. *Icarus* 195: 415-33.

Matson, D., L. Spilker, and J-P. Lebreton. 2002. The Cassini-Huygens mission to the Saturnian System. *Space Science Review* 104: 1-58.

Meyer-Peter, E., and R. Muller. 1948. Formulas for Bedload Transport. Paper presented at the International Association of Hydraulic Structures Research, Report on 2nd meeting, Stockholm, Sweden.

Meier, R., B. Smith, T. Owen, and R. Terrile. 2000. The surface of Titan from NICMOS observations with the Hubble Space Telescope. *Icarus* 145: 462-473.

Mitchell, K. 2008. The drying of Titan's dunes: Titan's methane hydrology and its impact on atmospheric circulation. *Journal of Geophysical Research* 113: E08015, doi.1029/2007JE003017.

Mitchell, K., B. Stiles, H. Zebker, R. Kirk, J. Lunine, A. Hayes, C. Wood, R. Lorenz, E. Stofan, R. Lopes, S. Vance and the Cassini Radar Team. 2009. A Global Sub-surface Alkanifer System on Titan? Paper presented at the Lunar and Planetary Science Conference, March 23-27, in Woodlands, Texas.

Mousis, O., and B. Schmitt. 2008. Sequestration of Ethane in the Cryovolcanic Subsurface of Titan. *The Astrophysical Journal.* 677: L67-L70.

Mueller, E., and J. Pitlick. 2005. Morphologically based model of bed load transport capacity in a headwater stream. *Journal of Geophysical Research* 110: F02016, doi:1029/2003JF000117.

Nelson, R., L. kamp, R. Lopes, D. Matson, R. Kirk, B. Hapke, S. Wall, M. Boryta, F. Leader, W. Smythe, K. Mitchell, K. Baines, R. Jaumann, C. Sotin, R. Clark, D. Cruikshank, P. Drossart, J. Lunine, M. Combes, G. Bellucci, J. Bibring, F. Capaccioni, P. Cerroni, A. Coradini, V. Formisano, G. Filacchione, Y. Langevin, T. McCord, V. Mennella, P. Nicholson, B. Sicardy, P. Irwin, and J. Pearl. 2009. Photometric changes on Saturn's Titan: Evidence for active cryovolcanism. *Geophysical Research Letters* 36: L04202, doi:10.1029/2008GL036206.

Niemann, H., S. Atreya, S. Bauer, G. Carignan, J. Demick, R. Frost, D. Gautier, J. Haberman, D. Harpold, D. Hunten, G. Israel, J. Lunine, W. Kasprzak, T. Owen, M. Paulkovich, F. Raulin, E. Raaen, and S. Way. 2005. The abundances of constituents of Titan's atmosphere from the GCMS instrument on the Huygens probe. *Nature* 438: 779-84.

Paganelli, F., M. Janssen, R. Lopes, E. Stofan, S. Wall, R. Lorenz, J. Lunine, R. Kirk, L. Roth, C. Elachi, the Cassini Radar Team. 2007. Titan's surface from the Cassini RADAR radiometry data during SAR mode. *Planetary and Space Science* 56: 100-08.

Paillou, P., K. Mitchell, S. Wall, G. Ruffie, C. Wood, R. Lorenz, E. Stofan, J. Lunine, R. Lopes, and P. Encrenaz. 2008. Microwave dielectric constant of liquid hydrocarbons: Application to the depth estimation of Titan's lakes. *Geophysical Research Letters*. 35: L05202, doi:10.1029/2007GL032515.

Perron, J., M. Lamb, C. Koven, I. Fung, E. Yager, and M. Adamkovics. 2006. Valley formation and methane precipitation rates on Titan. *Journal of Geophysical Research – Planets* 111: E11001, doi:10.1029/2205JE002602.

Porco, C., E. Baker, J. Barbara, K. Beurle, A. Brahic, J. Burns, S. Charnoz, N. Cooper, D. Dawson, A. Del Genio, T. Denk, L. Dones, U. Dyudina, M. Evans, S. Fussner, B. Giese, K. Grazier, P. Helfenstein, A. Ingersoll, R. Jacobson, T. Johnson, A. McEwen, C. Murray. G. Neukum, W. Owen, J. Perry, T. Roatsch, J. Spitale, S. Squyres, P. Thomas, M. Tiscareno, E. Turtle, A. Vasavada, J. Veverka, R. Wagner, and R. West. 2005. Imaging of Titan from the Cassini spacecraft. *Nature*. 434: 159-68.

Radebaugh, J., R. Lorenz, R. Kirk, J. Lunine, E. Stofan, R.M. Lopes, and S.D. Wall. 2007. Mountains on Titan observed by Cassini Radar. *Icarus* 192: 77-91.

Rannou, P., F. Montmessin, F. Hourdin, and S. Lebonnois. 2006. The Latitudinal Distribution of Clouds on Titan. *Science*. 311: 201-05.

Ritter, D., R. Kochel, and J. Miller. 2002. Process Geomorphology. Long Grove: Waveland Press Inc.

Schaller, E., M. Brown, H. Roe, and A. Bouchez. 2006. A large cloud outburst at Titan's south pole. *Icarus*, 182: 224-9.

Sklar, L., and W. Dietrich. 2004. A mechanistic model for river incision into bedrock by saltating bed load. Water Resources Research 40: W06301, doi:10.1029/2003WR002496.

Smith, P., M. Lemmon, R. Lorenz, L. Sromovsky, J. Caldwell, and M. Allison. 1996. Titan's surface, revealed by HST imaging. *Icarus* 119: 336-49.

Sotin, C., R. Jaumann, B. Buratti, R. Brown, R. Clark, L.A. Soderblom, K. Baines, G. Bellucci, J-P. Bibring, F. Capaccioni, P. Cerroni, M. Combes, A. Coradini, D. Cruikshank, P. Drossart, V. Formisano, Y. Langevin, D.L. Matson, T. McCord, R. Nelson, P. Nicholson, B. Sicardy, S. LeMouelic, S. Rodriguez, K. Stephan, and C. Scholz. 2005. Release of volatiles from a possible cryovolcano from near-infrared imaging of Titan. *Nature* 435: 786-789.

Stofan, E., C. Elachi, J. Lunine, R. Lorenz, B. Stiles, K. Mitchell, S. Ostro, L. Soderblom, C. Wood, H. Zebker, S. Wall, M. Janssen, R. Kirk, R. Lopes, F. Paganelli, J. Radebaugh, L.Wye, Y. Anderson, M. Allison, R. Boehmer, P. Callahan, P. Encrenaz, E. Flamini, G. Francescetti, Y. Gim, G. Hamilton, S. Hensley, W. Johnson, K. Kelleher, D. Muhleman, P. Paillou, G. Picardi, F. Posa, L. Roth, R. Seu, S. Shaffer, S. Vetrella, and R. West. 2007. The Lakes of Titan. *Nature* 445: 61-64.

Strahler, A. 1952. Dynamic Basis of Geomorphology. *Geologic Society America Bull* 63: 923-38.

Thompson, W. 1984. A physical and chemical study of Titan: atmosphere, clouds, and hazes. PhD Diss., Cornell University.

Tobie, G., O. Grasset. J. Lunine, A. Mocquet, and C. Sotin. 2005. Titan's internal structure inferred from a coupled thermal-orbital model. Icarus 175: 495-502.

Tomasko, M., B. Archinal, T. Becker, B. Bezard, M. Bushroe, M. Combes, D. Cook, A. Coustenis, C. de Bergh, L. Dafoe, L. Doose, S. Doute, A. Eibl, S. Engel, F. Gliem, B. Grieger, K. Holso, E. Howington-Kraus, E. Karkoschka, H. Keller, R. Kirk, R. Kramm, M. Kuppers, P. Lanagan, E. Lellouch, M. Lemmon, J. Lunine, E. McFarlane, J. Moores, G. Prout, B. Rizk, M. Rosiek, P. Rueffer, S. Schroder, B. Schmitt, C. See, P. Smith, L. Soderblom, N. Thomas, and R. West. 2005. Rain, winds and haze during the Huygens probe's descent to Titan's surface. *Nature* 438: 765-78.

Tran, B., J. Ferris, and J. Chera. 2003. The photochemical formation of a Titan haze analog. Structural analysis by X-ray photoelectron and infrared spectroscopy. *Icarus* 162: 114-24.

Turcotte, D., and G. Schubert. 2002. Geodynamics, 2nd ed. New York: Cambridge UP.

Ward, A., and S. Trimble. 2004. Environmental Hydrology. New York: CRC Press LLC.

Whipple, K., G. Hancock, and R. Anderson. 2000. River incision into bedrock: Mechanics and relative efficacy of plucking, abrasion, and cavitation. *Geological Society of America Bulletin* 112: 490-503.

Yung, Y., and M. Allen. 1984. Photochemistry of the Atmosphere of Titan: Comparison between model and observations. *The Astrophysical Journal Supplement Series* 55: 465-506.